

COMPUTATIONAL INVESTIGATION OF SMALL  
MOLECULE CATALYSIS BY COBALT, RHODIUM,  
AND IRIIDIUM MOLECULAR CATALYSTS

Thesis by  
Samantha Jo Iva Johnson

In Partial Fulfillment of the Requirements for  
the degree of  
Doctor of Philosophy

The Caltech logo is displayed in a bold, orange, sans-serif font. The word "Caltech" is centered within a light gray rectangular background.

CALIFORNIA INSTITUTE OF TECHNOLOGY  
Pasadena, California

2017  
(Defended December 2<sup>nd</sup>, 2016)

© 2016

Samantha Jo Iva Johnson  
ORCID: [0000-0001-6495-9892]

# DEDICATION

*For Kevin*

*“She is trying to guide his way home, from the waters that keep them apart.”*  
*-Roy Khan*

## ACKNOWLEDGEMENTS

There are few times in one's life where one has the opportunity thank the people around them who have lent support and laughter. As I conclude my formal education and experience the emotional upheaval that comes with it, it feels appropriate to *attempt* to thank as many people as I can. No person walks the path to and through graduate school alone and it is through the grace and love of other people that I have been able to come this far. I have been blessed with an amazing group of friends, family, and mentors who have walked with me at various parts of this journey. I stress that this is an attempt to acknowledge how much of my success is owed to others, but these words feel inadequate when compared to the love and dedication of those mentioned here.

Growing up in a small town, I never thought I would come this far in my education. I am not sure I even knew what a Ph.D was. Regardless, I was supported by an amazing cadre of teachers who took a strange little girl and transformed her into a lifelong student (though maybe still strange). For my early education, I thank Rob Pipal, for encouraging curiosity and engaging me. To Susan Khair, for nurturing a love of writing and forgiving me for choosing a career in science. Mary Sheedy, thank you for forcing me to take chemistry and guiding me through my younger years. You were the first person who said I would get a Ph.D and it turns out you were right (hopefully, as I technically don't have one while writing this). Steve Kaeuper, you gave me courage both in mathematics and in life. To Diane Davison, who not only morphed my love of talking into a useful skill, but became my friend. And finally, I thank John Fennell. Despite receiving the clumsiest chemistry student ever (evidenced by how many times I spilled or ignited chemicals in class), you gifted me a love of chemistry. However, there is only so much a teacher can do in terms of dexterity and balance, so I had to become a computational chemist.

I was blessed to have excellent mentors through college as well. Dr. Alan Weimer, thank you for taking a high school student and giving her a place in your lab for over four years, as well support on the journey to graduate school. To Dave King, I am eternally grateful because you had to actually work with said high school student. You truly made me a scientist, though I am not sure I will ever measure up to you. You taught me to be curious but critical and gave me all the tricks of the trade, including almost all the ones I use in my own mentorship. Thank you from the bottom of my heart. A special thank you to the Boettcher Foundation, for giving me the means to study. To Wendy Young, Joan Gabriele and Deb Viles, thank you for giving me a home on campus.

At Caltech, so many people have been instrumental in my ability to grow and learn. In my graduate work, I have been given so much support, including financial. Thank you to the National Science Foundation (Grant No. DGE-1144469) for their support of my work here and in Sweden. I would also like to acknowledge the Resnick Sustainability Institute for their support of my final two years. To Neil, Heidi, all the Resnick Scholars, and Lynda and Stewart Resnick, I owe you so much.

To my adviser Bill Goddard, thank you for taking me into your group and letting me witness the way you think. I deeply appreciate the opportunity. Thank you for all the guidance and support.

To my non-adviser but frequent mentor, Harry Gray, thank you for taking time with a student who was not strictly yours. You did not have to, but you often made time to share your wisdom



with me. I would also like to thank Jay Winkler and Bruce Brunschwig at this point for answering so many questions.

I am greatly indebted to my other “not strictly, but sometimes” adviser Petter Persson. I came to you disillusioned, frustrated, and ready to abandon dreams of science (not unlike many fourth year graduate students). You reminded me why I chose this field and what was to be enjoyed here. You filled so many roles: adviser, mentor, mentor via Skype, and dare I say, friend. Thank you for taking an American girl who cold emailed you in the middle of the night, giving her a chance, and (most-excruciatingly) navigating Swedish bureaucracy on her behalf. I look forward to many fruitful years of friendship and collaboration.

Finally, to the head of our catalysis subgroup and my officemate Robert “Smith” Nielsen, yo dawg. You taught me to ask the next question in research and how to care about the details (a lesson I am still learning). You taught me who Trevor Siemian was (before the Broncos did), how to make tiny Dove Chocolate wrapper dragons, and how to have a sense of humor in science. In the darkest times in the subbasement, you were truly a guiding light. You deserve every success.

To my committee members Professor Greer and Professor Faber: thank you for reading this document, if you are still hanging on. I appreciate your time, effort, and guidance. I look forward to your thoughts.

I have also been aided by an incredible group of staff members who I am lucky to have as friends. To Christy Jenstad, Michelle Rodriguez, and Daniel Yoder, I owe you my sanity. Thank you for helping me keep it through Disney-themed cocktails, dancing, and softball. To Mandy, thank you for helping me find ways to navigate. You were truly a catalyst to my growth, professionally and personally.

To two of my fantastic collaborators James Blakemore and Jenny Yang, thank you for being colleagues *and* friends. James, I still owe you a trip to Kansas, but when I get there I am beelining to the nearest public location to announce, “Ma’am! That is not a table.” Jenny, you are my role model in everything you do, personally and scientifically. I am holding you to that Seattle-to-Portland promise.

I have been incredibly lucky to work with a talented group of undergraduate and high school students: Sean, Sydney, Emily, Allison, Walther and Jeffrey. Thank you all for helping me find my calling, doing excellent work (some of which is featured here), and being awesome people. To Mrs. Patton and my students at CVHS, thank you for reminding me every Friday how full of wonder science and chemistry can be.

To my friends in the Lewis and Gray Groups, especially Sarah Del Cielo, Bryan Hunter, Brian Sanders, Astrid Mueller, Chris Roske, Noah Plymale, and Sonja Francis. Thank you for being my colleagues when I needed “time with the chemists” (as Kevin calls it) and my friends down the hall. You’ve been my partners-in-crime at ACS and CCI meetings. I imagine there are many beers to be shared with you all at various conferences and meetings in the future. Thank you for taking me under your wing.

I have been fortunate to be surrounded by a warm and loving group in the Goddard Group. Thank you Hai, Fan, Andres, and Jamil for being eternal sources of knowledge and support. To Caitlin Scott, your giggle and smile brought me through many a trying day. You have mentored me even beyond your time in our group and I thank you for that. Matt Gethers, you patiently

taught me LAMMPS and were a companion I could count on. The greasy t-butyl groups in this thesis are dedicated to you. On a day-to-day basis, my office mates in 07 have become family. Not enough can be said about how amazing you all are. Sijia, you put up with our incessant chatting all these years with a smile. You are my lady buddy in the office, my ACS roomie, and true friend. To Yufeng, who knows only one speed, you are an amazing cycling buddy, chemist, and friend. Jason and I will show up to your future ACS celebration in our walkers if we have to. And with that, Jason, who I once described as curmudgeonly, thank you for teaching me helpful skepticism. Many mornings began with a philosophical discussion about science, politics, jokes about Sweden... every discussion worth the time. You also introduced me to cycling through endless hounding. Thank you all for sharing and decorating 07 with me. I look forward to the camping trips to come.

My materials science class was quite close, especially in our early years here. The closeness was founded on a love of two things: doing homework together and hour-long lunches. Thank you John, Erik, Fadl, and by extension, Ivan, Jackie, Sarah, and Renee, Georgia, for being my mid-day refuge! To Chengyun, you'll always be part of my club. I am looking forward to visiting you in Tennessee and going to Dollywood. I'm sure there will be a lot of dancing and silly pictures involved.

While I was at Caltech, I may have found my second true love, cycling. To my cycling group, the Buffalo Riders, thank you for two great Big Bear trips and numerous Saturday morning rides, all ending with either beer or baked goods. Mark, Yufeng, Max, Carl, Sean, Kelly, and Dongwan, you guys are the best cycling buddies ever. Special thanks to Mark: your beginner ride is not for beginners, but Byblos Bakery and your friendship made it worth it.

To my discussion group at St. Rita: I appreciate your patience, companionship, teaching, and love. You've given my life in California dimension and meaning I did not know it could have.

My friends in Colorado continued to support me from afar. To Chris, Cookie & Morgan, Kelsey & Matanya, Jess, John, Max & Steve, and Nate: I love you guys. You helped get me here and you have stayed with me through times of little communication on my part. Thank you. Also, Cookie, I managed to not light myself on fire for several years. Thank you for encouraging me to pursue computation.

Jayme, Chris and Keagan: You were a slice of home right here in California. Thank you for the pedicures and the Bronco games and reminders that there is life beyond school.

Sunita and Oliver: from our first meeting to chaperoning a jazz club dinner to multiple triathlons, trips, parties, even editing parts of this thesis: My graduate school experience would not be complete without you. Thank you and I look forward to Indian and Japanese adventures to come!

Max and Ioana: Thank you both for the love and risotto. Max, you have supported Kevin and I more times than I can count. You were particularly amazing while I was away. Thank you for always lending a willing hand and ear.

Hannah and Andrew: from graduate school orientation until now, you have both been so close to us. So many late Saturday nights were spent over wine and cheese, talking or watching movies. Not to mention, so many Wednesday nights victorious in trivia. We've been through a lot this past year. You both mean so much to me.

My first friend at Caltech was Lisa Mauger, who I met during my prospective student visit. A fellow Coloradan, she took time to show me around campus, even showing me her apartment in the Cats so I knew what to look forward to. Most importantly, she took me to Ernie's, solidifying my graduate school choice. She dragged me to summer softball and taught me the art of trash talking even when you are on the worst team in the league. She is a role model in terms of generosity, social justice, and reliability. Thank you for being an overflowing font of joy and love in my life. Chris Marotta, you came a little later, but you hold no lower place. You are my football buddy and cooking companion. You brought me pot roast and cookies and you made me swim with you, even when I did not want to get up so early. These things truly helped me write this thesis. I consider you my advisor in my minor in "Dumb Internet Videos." Chris and Lisa, our trip to Munich was by far a highlight of the last five years. I always know I can count on you.

To my Mom and Dad: You've supported my education my entire life, even when you didn't know or understand the implications. You drove me sixty miles roundtrip every day for three years so I could receive a top-notch high school education. Who'd have thought I would take it this far? Thank you for the blind faith in what I was doing and love that enabled it. I am forever grateful for what you have done and love you both. I'll always be your freak of nature.

Grandma and Pops: You taught me so much about hard work, ingenuity, horse trading, and the old ways of doing things. I carry those lessons with me. I love you very much.

Keith, and Kacey: You were there with me in the beginning and you will be there with me in the end. Words cannot begin to convey your place in my heart. To have siblings that became my best friends is a true blessing in this life.

And finally to Kevin, to whom I dedicate this thesis, I truly would not be here without you in a very direct way. I had no intention of even applying to Caltech, but you started my application for me and continued to fill it out until, in your words, "It is no longer ethical for me to do this." I think you even hit the submit button, all because you believed in me. When my courage faltered, you raised me up. When I got restless, you encouraged me to roam. You have supported my dreams and schemes for eight years, no matter how small or silly. You are truly my world. I love you.



## ABSTRACT

Global energy demands are predicted to increase through 2040. In the spirit of meeting these demands, work focusing on increasing the efficiency of existing energy technologies, as well as improving energy storage is necessary. This work takes a catalytic approach to these challenges, focusing on Co, Rh, and Ir catalysts with pincer and bipyridine ligands. Density functional theory (DFT) can be used in order to gain a deeper understanding of how these catalysts behave. In the realm of improving existing technologies, the mechanism for oxidation of methane to methanol by Phebox Ir (Phebox = bis(oxazoliny)phenyl) is investigated with a focus on understanding how subtle substitutions to the ligand can help or hinder this reaction. It is shown that in this catalyst, two unwanted intermediates on the potential energy surface (an Ir<sup>IV</sup> state leading to catalyst deactivation and an Ir<sup>V</sup> state leading to over-oxidation) can potentially be avoided by adding trifluoromethyl groups to the ligand. For production of fuels from solar energy, two reactions are studied. Experimentally, CO<sub>2</sub> reduction to formate by (POCOP)Ir (POCOP = C<sub>6</sub>H<sub>3</sub>-2,6-[OP(*t*Bu)<sub>2</sub>]<sub>2</sub>) has been shown to selectively occur at moderate potentials. The mechanism by which this catalyst reduces CO<sub>2</sub> is elucidated. In particular, the impressive product selectivity afforded this catalyst for formate over hydrogen production is rooted in kinetics: high barriers for protonation inhibit the creation of H<sub>2</sub> adducts. In addition to this, substitutions to the ligand and metal center are investigated to further illuminate the relationship between kinetics and thermodynamics. Hydrogen evolution in Cp<sup>\*</sup>Rh(bpy) (bpy = 2,2'-bipyridine, Cp<sup>\*</sup> = pentamethylcyclopentadienyl) is investigated, centering on unexpected protonation at the Cp<sup>\*</sup> ligand rather than the metal center. This state is on the path for hydrogen evolution in the case of using weak acids, but in the presence of strong acids, the path through the traditional hydride is most likely. Finally, the attachment of these catalysts to electrode surfaces is discussed with the aim of making molecular catalysts a more viable option in industry. It is shown that chlorine present in the attachment process enables easy catalyst dissociation from the surface. Several non-halogen options are discussed as replacements. Throughout the thesis two themes emerge: the constant interaction between thermodynamics and kinetics to control mechanistic paths and products, and the ability of small modifications to have huge impacts on catalytic cycles.

## PUBLISHED CONTENT AND CONTRIBUTIONS

- D.W. Shaffer, **S.I. Johnson**, J.W. Ziller, R.J. Nielsen, W.A. Goddard, A.L. Rheingold, J.Y. Yang; Reactivity of a Series of Isostructural Cobalt Pincer Complexes with CO<sub>2</sub>, CO, and H<sup>+</sup>. *Inorganic Chemistry*. 2014. 53 (24) 13031. <http://dx.doi.org/10.1021/ic5021725>  
S.I.J. helped devise the computational mechanism, calculated all structures used in the manuscript, prepared the data and figures for the computational work, and participated in writing the manuscript.
- M. Zhou, M., **S.I. Johnson**, Y. Gao, T.J. Emge, R.J. Nielsen, W.A. Goddard III, A.S. Goldman, Activation and Oxidation of Mesitylene C–H Bonds by (Phebox)Iridium(III) Complexes. *Organometallics*. 2015. 34, 2879–2888 <http://dx.doi.org/10.1021/acs.organomet.5b00200>  
S.I.J. calculated all structures in the computational work, prepared the computational data, aided in explaining experimental results in accordance with computational results, and wrote the computational section of the manuscript.
- L. Aguirre Quintana; **S.I. Johnson**; S.L. Corona; W. Villatoro; W.A. Goddard III; M. K. Takase; D. G. VanderVelde; J. R. Winkler; H. B. Gray; and J.D. Blakemore; Proton-Hydride Tautomerism in Hydrogen Evolution Catalysis. *Proceedings of the National Academy of Sciences* 2016, 113 (23), 6409-6414. <http://dx.doi.org/10.1073/pnas.1606018113>  
S.I.J. participated in the conception of the project, guided undergraduate students to calculate structures, calculated structures herself, analyzed computational data and created figures representing the data, and participated in writing the manuscript.
- S.I. Johnson**; R.J. Nielsen; W.A. Goddard III. Selectivity for HCO<sub>2</sub><sup>-</sup> over H<sub>2</sub> in the Electrochemical Catalytic Reduction of CO<sub>2</sub> by (POCOP)IrH<sub>2</sub>. *ACS Catalysis*. 2016, 6362-6371. <http://dx.doi.org/10.1021/acscatal.6b01755>  
S.I.J. helped devise the mechanism, calculated most of the structures within the paper, analyzed the data and helped to prepare the manuscript.



## TABLE OF CONTENTS

Dedication.....	iii
ACKNOWLEDGEMENTS.....	iv
ABSTRACT.....	ix
PUBLISHED CONTENT AND CONTRIBUTIONS.....	x
Table of Contents.....	xii
Nomenclature.....	xx
Introduction.....	1
Current US and Global Energy Scenario.....	1
Keys to Catalysis.....	5
Ligand Classes.....	8
Role of Computation.....	9
Common Threads and Overview.....	12
References.....	14
C-H Activation Mechanisms in NNC and NCN Pincer Complexes: A computational study..	16
Introduction.....	16
Methods.....	18
Results and Discussion.....	19
Mesitylene Activation and Functionalization by the NCN pincer.....	19
Comparison of NNC and NCN pincer systems.....	23
Conclusions.....	28
References.....	30
Selectivity for HCO <sub>2</sub> <sup>-</sup> over H <sub>2</sub> in the Electrochemical Catalytic Reduction of CO <sub>2</sub> by (POCOP)Ir(H) <sub>2</sub> .....	32
Introduction.....	32
Methods.....	34
Results and Discussion.....	35
CO <sub>2</sub> Conversion.....	35
Electrochemical Catalyst Regeneration.....	38
Hydrogen Evolution.....	40
Cobalt Analogue.....	46
Hydricities as a Guiding Design Principle.....	46
Conclusions.....	50
References.....	52
Modifications on the (PEXEP) Pincer Platform: Thermodynamics and Kinetics of CO <sub>2</sub> Reduction and Hydrogen Evolution.....	54
Introduction.....	54
Methods.....	56
Results and Discussion.....	58
Modification of the <i>ipso</i> position.....	64
(PENEP)Co catalysts.....	64
(PONOP)Ir.....	66
Conclusions.....	67



References.....	69
Mechanisms for Hydrogen Evolution for Cp*Rh(bpy) .....	71
Introduction .....	71
Methods .....	73
Results and Discussion.....	74
Routes to First Protonation .....	74
Protonation from the Cp*H complex.....	77
Modified bipyridine ligands.....	83
References.....	86
Design of Robust Attachment of Bipyridine Ligands to Si for the Immobilization of Homogeneous Catalysts.....	87
Introduction .....	87
Methods .....	88
Results and Discussion.....	89
Effect of Chlorination on the Linker.....	89
Other bpy systems as replacements.....	94
Conclusion.....	99
References.....	100
Appendix A: Supplementary Calculations Supporting CO <sub>2</sub> Reduction .....	102
Appendix A.1: Calculation of the doubly reduced acetonitrile complex.....	102
Appendix A.2.....	103
Appendix A.4.....	105
Appendix A.5.....	106
Appendix A.6.....	107
Appendix A.7.....	108
References.....	108
Appendix B: Full Results on Modification of POCOP Pincers .....	110
Appendix B.1: Results of simulations involving substitutions of (R-POCOP)Ir .....	110
Appendix C: Molecular Coordinates .....	112



## LIST OF FIGURES AND SCHEMES

<b>Figure 1.1:</b> Global demand for energy, divided into contributions from developed (OECD) and developing countries. Figure courtesy of the US Energy Information Administration. <sup>1</sup>	1
<b>Figure 1.2:</b> Global demand for petroleum and liquid fuels with projection. Increasing demand is largely driven by demand in growing economies. Figure courtesy of the US Energy Information Administration. <sup>1</sup>	2
<b>Figure 1.3:</b> Model potential energy surface for catalyzed and uncatalyzed reactions.	5
<b>Figure 1.4:</b> Schematic of a. an arbitrary pincer, b. the side view of the arbitrary pincer, and c. bipyridine.	8
<b>Figure 2.1:</b> a. (NNC)Ir, b. (NCN)Ir (PheBox or NCN) ligand, c. theoretical NCN ligand ( $\Delta$ NCN)	17
<b>Scheme 2.1:</b> Binding of mesitylene in the (NCN) catalyst shows sensitivity to the X ligand, with X = OAc giving over 90% yield and TFA showing approximately 18% yield.	19
<b>Scheme 2.2:</b> Results of H/D exchange reactions, showing that the TFA analogue undergoes approximately twice as many turnovers as the OAc analogue.	20
<b>Scheme 2.3:</b> Ratios of aldehyde (DBAL) to carboxylic acid (DBAC) product for the OAc and TFA analogues.	20
<b>Scheme 2.4:</b> Calculated free energies (kcal/mol) for (1) C-H activation pathway and (2) Ir-oxo pathway in catalytic mesitylene oxidation using complexes <b>1</b> or <b>2</b> ; X = OAc or OCOCF <sub>3</sub> ; “Phebox” ligand was not shown but was implied, except in complexes <b>1</b> , <b>2</b> , <b>3</b> , and <b>4</b> ; no calculations performed for <b>6-OAc</b> and <b>6-OCOCF<sub>3</sub></b> .	21
<b>Figure 2.2:</b> (a) Calculated structure of TS1-OCOCF <sub>3</sub> and TS1-OCOCH <sub>3</sub> (peripheral atoms omitted for clarity) (b) Selected interatomic distances indicated (Å)	22
<b>Scheme 2.5:</b> Methane activation occurs in this scheme by concerted metalation/deprotonation. Due to the decreased <i>trans</i> influence, the NNC complex yields the lowest barrier.	24
<b>Scheme 2.6:</b> Two undesired pathways are shown. The top pathway displays the deactivated Ir <sup>IV</sup> complex and the lower pathway shows the formation of the iridium oxo complex.	25
<b>Scheme 2.7:</b> Activation of benzene is competitive with methane activation in both the NNC and NCN, as shown by <b>TS5</b> .	26
<b>Scheme 2.8:</b> Use of electron withdrawing group CF <sub>3</sub> aids in lowering the barrier for CMD while also raising the energy of undesired intermediates leading to deactivation and side reactions.	28
<b>Figure 3.1:</b> Meyer and Brookhart POCOP complex and their proposed mechanism.	32
<b>Scheme 3.1:</b> Plausible reaction pathways with calculated free energies (in kcal/mol) and bond lengths (in Ångstroms) for the Ir case.	35
<b>Figure 3.2:</b> Transition states for CO <sub>2</sub> RR (A.) and protonation by formic acid (B.).	37
<b>Figure 3.3:</b> The HOMO of <b>Mol 1</b> for iridium (left) and cobalt (right), showing the preference in iridium for the formation of the dihydride as opposed to the dihydrogen adduct in cobalt.	38
<b>Scheme 3.2:</b> Proposed regeneration of the catalyst occurs as solvent dissociates and the metal is reduced. Free energies (kcal/mol) and potentials (V vs NHE, blue) are reported.	39

<b>Figure 3.4:</b> The HSOMO of the Ir <sup>II</sup> hydride complex ( <b>Mol 7</b> ) shows the bent geometry and quasi d- $\pi$ orbital. ....	39
<b>Scheme 3.3:</b> Reaction of the iridium hydride anion with CO <sub>2</sub> is thermodynamically feasible, but is competitive with protonation. Free energies are reported in kcal/mol. ....	40
<b>Scheme 3.4:</b> Free energies illustrating the thermodynamic, but not kinetic, feasibility of hydrogen evolution. ....	40
<b>Scheme 3.5:</b> Free energies of protonation of the dihydride by different water cluster geometries. ....	41
<b>Scheme 3.6:</b> Intramolecular protonation of the dihydride. Bridging waters lower the barrier, but this path is not competitive with CO <sub>2</sub> reduction. Free energies are reported. ....	42
<b>Scheme 3.7:</b> Free energies for potential pathways for the formation of hydrogen involving carbonic acid, formic acid, and bicarbonate in water, pH = 7. ....	43
<b>Scheme 3.8:</b> Competing regeneration and CO <sub>2</sub> RR routes from the Ir <sup>I</sup> hydride anion with the preferred pathway in black. Free energies are reported. ....	44
<b>Figure 3.5:</b> Thermodynamic cycle used for calculating the hydricity of the iridium dihydride, hydride, and cobalt hydride in neat acetonitrile and water. ....	48
<b>Figure 4.1:</b> POCOP-Ir is substituted in the <i>para</i> position (R) with -NH <sub>2</sub> , -OH, -Me, -H, and -CF <sub>3</sub> , the arm groups (E) with -CH <sub>2</sub> and -O and the <i>ipso</i> position (X) with -C and -N to change the electronic structure of the catalyst. ....	55
<b>Figure 4.2:</b> Pathways for CO <sub>2</sub> reduction and hydrogen adduct formation are shown for three representative pincer complexes (R-POCOP, X = NH <sub>2</sub> , H, CF <sub>3</sub> ). Free energies in kcal/mol. ....	59
<b>Figure 4.3:</b> HOMO orbitals of a. CF <sub>3</sub> -POCOP and b. NH <sub>2</sub> -POCOP dihydride. Both analogues show mixing of the $\pi$ -system of the phenyl ring with the d <sub>xz</sub> orbitals of the metal. ....	60
<b>Figure 4.4:</b> Free energy for coordination of acetonitrile versus <i>para</i> (a.) and <i>meta</i> (b.) Hammett constants show that more electron withdrawing group favor acetonitrile coordination. ....	61
<b>Figure 4.5:</b> Calculated hydricity as a function of <i>para</i> and <i>meta</i> Hammett constants. ....	62
<b>Figure 4.6:</b> Transition states for hydride abstraction by CO <sub>2</sub> ( <b>TS 1</b> , green) and protonation of hydride ( <b>TS 2</b> , blue) as a function of hydricity. ....	63
<b>Scheme 4.1:</b> Calculated pKa values and CO <sub>2</sub> binding energies for the reduction of [(PCNCP)Co] and [(POCOP)Co]. ....	65
<b>Scheme 5.1:</b> Previous mechanisms for hydrogen evolution in this catalyst involved the generation of a Rh <sup>III</sup> hydride. Experimentally, protonation of the Cp* is seen. ....	71
<b>Scheme 5.2:</b> Protonation at the metal center to form the traditional hydride is the most kinetically feasible pathway. ....	74
<b>Figure 5.1:</b> Frontier orbitals of complexes <b>1</b> , <b>2</b> , and <b>3</b> . While in the original complex the HOMO is delocalized, on <b>3</b> it is localized in a dz <sup>2</sup> orbital. ....	75
<b>Scheme 5.3:</b> After formation of the hydride, the proton can bridge, forming the Rh <sup>I</sup> complex with the protonated Cp* ligand. ....	76
<b>Scheme 5.4:</b> Routes involving a second protonation by HDMF. Energies in kcal/mol and bond lengths in Ångstroms. ....	77
<b>Figure 5.2:</b> Relaxed coordinate scan moving the Rh-H distance 0.015 Å each step. ....	78
<b>Figure 5.3:</b> Relevant transition states, a. <b>TS 5</b> ; b. <b>TS 3</b> ; c. Attack on hydride from bottom. ...	79

<b>Figure 5.4:</b> Potential energy surface along a decreasing H-H bond distance with acid attack from the bottom.....	80
<b>Figure 5.5:</b> Varying the H-H distance and the Rh-H distances yields several critical points of interest, geometries of which can be seen in A., B., and C. ....	82
<b>Figure 5.6:</b> 5.6a.) Linear correlation between the Hammett constant of functional groups on bpy and energy difference between complexes 2 and 3 shows the effect of bpy on this complex. 5.6b.) As the functional groups become more electron withdrawing, the complex becomes harder to protonate. ....	83
<b>Scheme 5.5:</b> The hydride is slightly favored in phosphine-based ligand sets. ....	84
<b>Figure 6.1:</b> Relative energies (compared to A) of Cl binding motifs. ....	89
<b>Figure 6.2:</b> Molecular complexes with chlorinated linkers.....	90
<b>Figure 6.3:</b> Spin density of the reduced chlorinated bpy complex. The chloride ion is released and settles at a distance 5.27 Å away from the β-carbon.....	91
<b>Figure 6.4:</b> Spin density from two views on the reduced chlorinated complex 2 attached to a silicon cluster. The molecular and attached spin densities are quite similar to the molecular complex. The C-Cl distance is 3.62 Å, suggesting the chlorine has migrated from the linker.....	92
<b>Scheme 6.1:</b> The transition state for dissociation using a tris(trimethyl)silane toy system is shown in TS 1. While the overall barrier is dependent on the operating potential, the barrier energy from 5 is constant at 19.1 kcal/mol. This is accessible at room temperature. Additionally, the driving force for this complex gets stronger as more negative potentials are reached.....	93
<b>Figure 6.5:</b> Overall dissociation barrier as a function of potential. As more negative potentials are reached, the dissociation becomes more kinetically favorable. ....	94
<b>Figure 6.6:</b> Molecular test analogues used to investigate ways to utilize bpy's non-innocent properties. In the halogenated species 7 and 8, X= F, Br. ....	94
<b>Figure 6.7:</b> Spin density plots of the modified bpy ligands. In the fluorinated (7F), bis-CF <sub>3</sub> (9) and sp <sup>3</sup> -hybridized linker (11) cases, electron density is isolated on the bpy, behavior expected for the non-innocent ligand .....	95
<b>Figure 6.8:</b> Spin density plot of the surface-attached fluorinated complex. Density is mostly confined to the bpy ligand.....	96
<b>Figure 6.9:</b> Spin density on reduced 4-ethynyl-2,2'-bipyridine A) in molecular form and B) on the cluster surface.....	98
<b>Scheme A.1:</b> Free energies calculated in acetonitrile at -1.2V vs SHE. Reduction with loss of solvent is preferred to a two-electron reduction of the solvento complex, as previously proposed, <sup>1</sup> which leads to a reduced acetonitrile adduct. Energies in kcal/mol. ....	102
<b>Figure S1:</b> HOMO of Ir <sup>I</sup> complex .....	103
<b>Scheme A.4:</b> a) Structures of quaternary amine POCOP; b) Free energies of reactions featuring the full ligand versus the truncated ligand. ....	105
<b>Scheme A.5:</b> Free energies for protonation via the Y-shaped cluster.....	106
<b>Figure A.6:</b> Figures of points along the intrinsic reaction coordinate calculation. A. Point on the reverse path; B. The transition state; C. Point on the forward path. All bond lengths in Angstroms. For reference, the spectator Ir-H bond length is 1.70 Å. ....	107
<b>Figure A.7:</b> Hydricities of (POCOP) Ir compared to other hydridic compounds.....	108

**Figure B.1:** Full results of modifications of the *para* position of pincers. Trends here largely scale with electron withdrawing ability of the catalysts. Numerical results can be seen in the table below..... 110

## LIST OF TABLES

<b>Table 3.1:</b> Contribution of solvation free energy (kcal/mol) to hydride transfer reactions. ....	48
Effect of Modification on Pathways and Hydricity .....	58
<b>Table 4.1:</b> Hammett constants and calculated hydricities .....	62
<b>Table 4.2:</b> Free energies for coordination of MeCN to (R-PONOP)Ir complexes. ....	67
<b>Table 6.1:</b> Atomic charges and spin populations of the reduced bpy complex.....	91
<b>Table B.1:</b> All free energies ( $\Delta G$ ) of para substitutions on barriers and kinetics of CO <sub>2</sub> RR and HER.....	111

## NOMENCLATURE

**Bipyridine (bpy).** 2,2'-bipyridine, a nitrogen-based heterocycle which is commonly used as a ligand in organometallic catalysis

**Hydride.**  $H^-$ , a proton and two electrons.

**HOMO.** Highest occupied molecular orbital

**HSOMO.** Highest singly-occupied molecular orbital

**Ligand.** An organic molecule bound to a metal center

**LUMO.** Lowest unoccupied molecular orbital

**Ortho.** See Phenyl Substitution section below.

**Meta.** See Phenyl Substitution section below.

**NHE.** Normal Hydrogen Electrode

**Para.** See Phenyl Substitution section below.

**Phebox.** Bis(oxazoliny)phenyl ligand

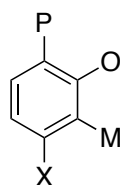
**POCOP.**  $C_6H_3-2,6-[OP(tBu)_2]_2$  ligand

**SHE.** Standard hydrogen electrode

**Turnover Number (TON).** Number of full catalytic cycles a catalyst completes

**Turnover Frequencies (TOF).** Number of turnovers in a given time span

**Phenyl substitutions.** If a group X is bound to a phenyl ring, as shown below, the ortho, meta, and para positions are indicated by O, M, and P, respectively.







## Chapter 1

### INTRODUCTION

#### Current US and Global Energy Scenario

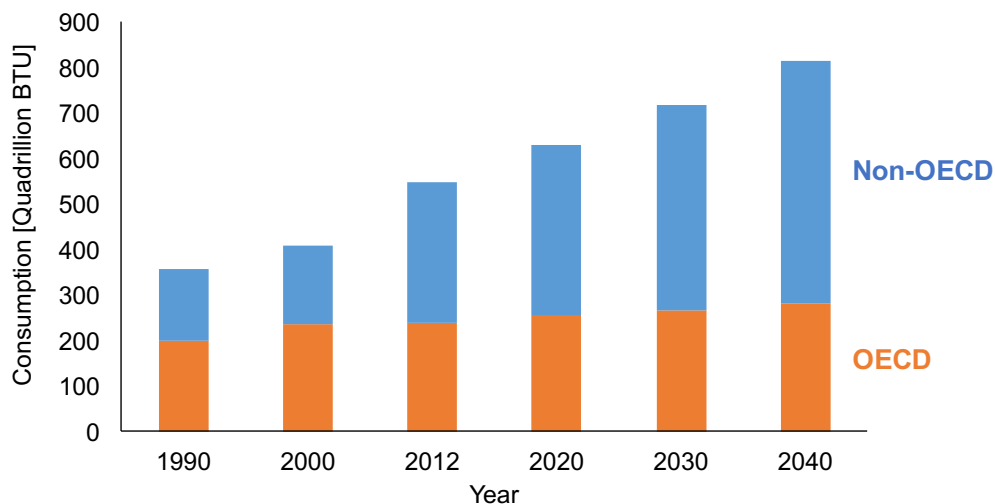


**Figure 1.1:** Global demand for energy, divided into contributions from developed (OECD) and developing countries. Figure courtesy of the US Energy Information Administration.<sup>1</sup>

As the global population increases, worldwide energy demand will grow with it. The overall predicted energy demand can be seen in Figure 1.1. In this figure, energy demand has been divided into two categories: demand from developed countries (defined by the US Energy Information Administration as countries belonging to the Organization for Economic Cooperation and Development [OECD])<sup>1</sup> and demand from developing economies. While demand in OECD countries is predicted to plateau and even decrease into the future, demand in developing countries will cause global energy demand to increase. The plateau in the US is attributed to increased appliance and vehicle efficiency, as well as a population shift to warmer regions, that require less heating.<sup>2</sup> Increasing demands in developing countries stems from higher demands for liquid fuels, personal travel, and materials in the industrial sector.<sup>1</sup>

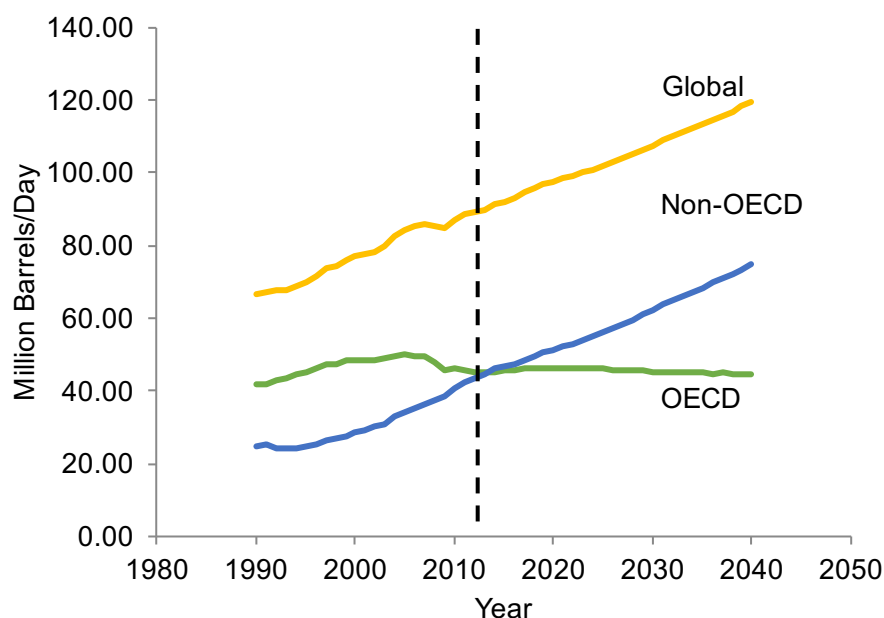


**Figure 1.2:** Global demand for petroleum and liquid fuels with projection. Increasing demand is largely driven by demand in growing economies. Figure courtesy of the US Energy Information Administration.<sup>1</sup>

In the United States, energy use can be divided into the following sectors: industrial, commercial, residential, and transportation. The largest consumer of energy is the industrial sector, comprising nearly one third of the U.S.'s energy use. This amount is predicted to grow into the future. Transportation contributes approximately 25% of the total energy use and is predicted to stay nearly the same. These two sectors are unique in that they are both significant users of petroleum and liquid fuels. According to the U.S. Energy Information Administration, “there are few substitutes for petroleum in construction, mining, agriculture, and manufacturing applications.”<sup>2</sup> Furthermore, petroleum accounted for 92% of the transportation sector’s energy usage (in 2010)<sup>3</sup>. The demand for petroleum and liquid fuels is not likely to subside. In fact, petroleum is the largest single source of fuel used in the United States, accounting for approximately 35% of primary energy use when divided by source.<sup>2,3</sup> In 2015, the U.S. net imported 4.21 million barrels of petroleum per day, with the top suppliers being Canada (40%), Saudi Arabia (11%), and Venezuela (9%).<sup>4</sup> Foreign petroleum sources composed about 24% of

US petroleum consumption in 2015. Demand for petroleum and liquid fuels is also projected to grow globally, as seen in Figure 2<sup>5</sup>.

The fastest growing energy sources in the United States are natural gas and renewable sources, including wind, solar, hydropower, and geothermal sources. Natural gas, a mixture of methane and other light hydrocarbons, is largely used in the US for industrial and electric power, and heating. One stumbling block for natural gas's expansion into the transportation sector or as a replacement for petroleum is its gaseous nature, which makes it difficult to store and transport.<sup>6</sup> While gas-to-liquid (GTL) technologies exist, including liquefied natural gas (LNG) and compressed natural gas (CNG), these technologies often encounter issues with storage and are relegated to fleet vehicles or ships<sup>7,8</sup>, or are prohibitively expensive<sup>9</sup>. Solar energy is the fastest growing renewable energy source and is predicted to continue growing 6% per year on average from 2015 to 2040.<sup>2</sup> Like natural gas, solar energy is faced with issues in energy storage.<sup>10-12</sup>

Growth in energy production to meet the rising demand often comes at a cost, especially when demand is met by fossil fuels. In 2015, China declared a red flag alert in Beijing due to hazardous pollution from coal plants north of the city.<sup>13</sup> CO<sub>2</sub> concentration in the atmosphere is predicted to increase without policies and technologies aimed at reducing emission.<sup>14</sup> Unmitigated increase in greenhouse gas emission (including CO<sub>2</sub> and CH<sub>4</sub>) is predicted by the Environmental Protection Agency (EPA) to have devastating effects on both the American environment and economy. Some of these effects include the loss of 35% of Hawaiian coral leading to recreational and tourism losses of \$1.1 billion, \$3.1 billion in predicted damages due to sea level rise and storm surge, and impacts on human health due to extreme temperatures and reduced air quality.<sup>15</sup> These losses represent damages to business, challenges to infrastructure, and decreasing ability for the economy to compete globally. Thus it is imperative to find and use clean liquid energy sources that also lower greenhouse gas emissions. Additionally, production of liquid fuels in the US presents a chance to improve energy security while also providing opportunities for strengthening the economy via export. Research aimed at meeting future demands can be directed in two broad thrusts: 1) improving existing energy technologies in terms of efficiency, or 2) investigating new methods of harvesting and storing energy. In this work, both approaches will be taken.

In the realm of existing energy technologies, natural gas is one of the fastest growing fuel sources in the US. However, much of the natural gas resources are tied up in stranded wells. These wells exist either in geographically isolated locations or locations that lack proper infrastructure. This includes methane trapped with other liquid hydrocarbons which is too difficult to transport.<sup>16,17</sup> Especially in this case, the infrastructure present is tailored to the transportation of liquid products. At room temperature and pressure, methane is a gas. As previously mentioned, there are some physical processes such as LNG and CNG meant to make methane easier to transport and their difficulty has been described.<sup>13</sup> However, there are also chemical processes aimed at converting methane into a transportable liquid. One such process is steam reformation of methane (SRM) to syngas, which can then be combined with the Fischer-Tropsch process to make higher order hydrocarbons.<sup>6,9,18</sup> Steam reformation occurs at temperatures in excess of 900 °C, requiring expensive alloys for reactors and plant components.<sup>9</sup> This in turn makes SRM a difficult option for wells in isolated locations, as the capital cost associated with the plant renders the process economically unviable, except in the case of very high oil prices.<sup>2</sup> Presently, methane recovered from isolated wells is typically flared to release CO<sub>2</sub> or released as methane directly, which has dire environmental impacts.<sup>14,15,19</sup> It also represents a source of waste in the process. Alternatively, chemical oxidation of methane to methanol, which is a liquid at room temperature, presents an attractive solution. Improvements made here could reduce the amount of energy required to transport natural gas, as well as enable more efficient recovery of energy resources from stranded wells. However, significant challenge lies in gently breaking the C-H bond, which at 105 kcal/mol is quite strong. Once one bond is broken, the remaining C-H bonds become weaker, leading to over-oxidation in most cases.

Solar energy presents an attractive option among renewables due to its large supply.<sup>11</sup> Utility-scale photovoltaics have grown in capacity from approximately 250 MW nationwide in 2010 to over 4000 MW in 2014, nearly a 16-fold increase.<sup>20</sup> The National Renewable Energy Lab's benchmark utility-scale installed price for PV has fallen, from \$4.39 in 2009 to \$1.77 in early 2015, largely attributed to decreasing costs of solar modules.<sup>20</sup> However, one challenge of solar energy is its intermittency: weather events, clouds, and the diurnal nature of the earth's solar cycle present a need for storage technologies. Batteries are problematic due to their low specific energies, implying that for a given energy storage capacity, they are quite heavy relative to conventional

liquid fuels. This is particularly relevant in the transportation sector, as the amount of energy required for long trips becomes intractably large. Their specific energies range from  $\sim 20$  W•h/kg for redox flow batteries to  $\sim 160$  W•h/kg for conventional lithium ion batteries.<sup>21</sup> By comparison, the specific energy of gasoline is around 170,000 W•h/kg.<sup>22</sup>

In order to achieve this kind of energy density, we can take a lesson from nature: photosynthesis is the process by which plants store solar energy as sugars made from water and CO<sub>2</sub>. By modifying this process to use sunlight to split water and provide protons and electrons to make fuels of our choosing, we create a process called *artificial photosynthesis*.<sup>10,11</sup> The harvested protons and electrons can be used to make hydrogen or can be combined with CO<sub>2</sub> to make carbon-based fuels. One advantage of using CO<sub>2</sub> as a feedstock is that one could close the loop in the carbon cycle. Fuels made from CO<sub>2</sub> release CO<sub>2</sub> when burned, which is then recovered to make more fuel. Unfortunately, these reactions can be incredibly complex and energy intensive. Even the basic case of  $2\text{H}^+ + 2\text{e}^- \rightarrow \text{H}_2$  can have puzzling and varied routes.<sup>23,24</sup> The one-electron reduction of CO<sub>2</sub> to the anionic radical occurs at -1.90 V vs SHE in water<sup>25</sup>, too high for commodity fuel production. CO<sub>2</sub> reduction can also have a variety of routes and products.<sup>9,26,27</sup>

### Keys to Catalysis

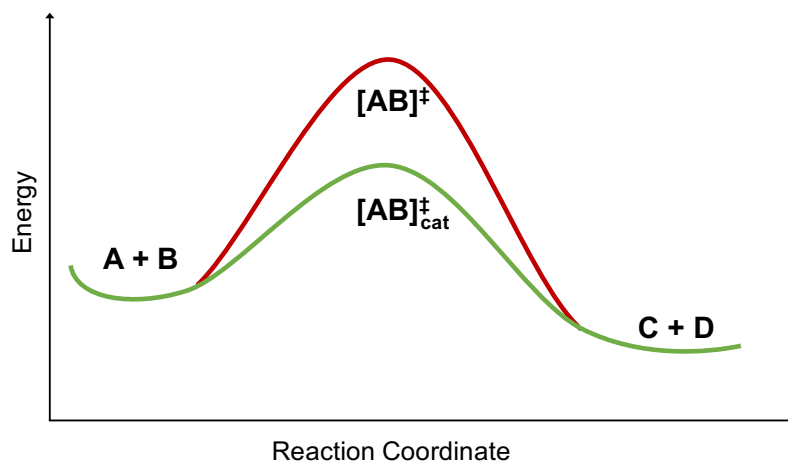


**Figure 1.3:** Model potential energy surface for catalyzed and uncatalyzed reactions.

One common thread between these two seemingly disparate energy problems is that they both involve high energy reactions with stable, small molecules. In order to reduce the energy requirement for these reactions (and thus lower their cost), we turn to catalysis. The potential energy surface (PES) for a model reaction ( $A + B \rightarrow C + D$ ) is seen in Figure 1.3. In this reaction, A and B represent our reactants and C + D are the products. These complexes are all referred to as *intermediates*. On a PES, intermediates are defined as minima. Moving along our reaction coordinate from A and B to C and D (left to right), we encounter a barrier in the energy surface, which is denoted as  $[AB]^\ddagger$ . The double dagger superscript is indicative of AB's status as a *transition state*. We define the transition state as the energy maximum in this figure, which features a two-dimensional PES. However, real PESs are usually multi-dimensional, so we define the transition state more rigorously as the saddle point in a PES dividing products and reactants in quasi-equilibrium.<sup>28,29</sup> The transition state energy (or activation energy) is related to the reaction rate coefficient, which helps to determine how quickly a reaction will progress. This was seen empirically by Svante Arrhenius, a Swedish chemist, and appears as his Arrhenius equation<sup>30</sup>. The related Eyring equation can be derived from transition state theory and has a similar functional form.<sup>31</sup> The Arrhenius equation can be seen in Eq. 1, where  $E_a$  is the activation energy, R is the gas constant, T is the temperature, and A is a pre-exponential factor.

$$k = Ae^{\frac{-E_a}{RT}} \quad (1)$$

The rate constant  $k$  is then related to the actual rate of reaction by multiplying it by some function of the reactant concentration.<sup>18</sup> This is a simplified description of the field of chemical kinetics and for further reference, the reader is referred to texts focusing solely on the topic.<sup>32-34</sup>

In Figure 1.3, there are two barriers,  $[AB]^\ddagger$  and  $[AB]^\ddagger_{\text{cat}}$ , which represent the uncatalyzed and catalyzed reactions, respectively. In the uncatalyzed case there is a higher barrier.

The catalyst is a material that lowers a reaction's barrier without affecting its thermodynamics, resulting in a faster reaction. A popular metaphor is that of traveling through a mountain range: one can walk directly over a mountain but will expend a lot of energy. This represents the uncatalyzed case. Alternatively, one can take a mountain pass or a tunnel through the mountain, metaphorically choosing the catalyzed route. In both cases, one starts and ends in the same place, but the amount of energy expended (and inherently the time it takes) varies by case. By

definition, at the end of the reaction, the catalyst is unchanged and can proceed with more catalysis. A reaction which is aided by a molecule or surface, but the molecule or surface is changed at the end and does not react in the same way is said to be *stoichiometric*, whereas a reaction in which a molecule aids in reaction and is returned to its original state to aid again is referred to as *catalytic*. In order to be catalytic, a catalyst's PES must have moderate barriers, but also must have intermediates that are not too low in energy. These create thermodynamic sink states, which are difficult to overcome. One common type of sink occurs when something binds too strongly to the catalyst, effectively poisoning it. If something does not bind at all, catalysis cannot be done. This is called the Sabatier principle (a.k.a. the Goldilocks principle). Catalysis relies on optimization of all factors.

From these definitions, three concepts emerge: turnover, turnover number, and turnover frequency. Turnover is when the catalyst is returned to its original state to start another catalytic cycle. Turnover number (TON) is defined as the number of turnovers completed. Turnover frequency (TOF) is the turnovers completed in a given time span.<sup>18</sup> High TON and TOF are crucial in catalysis as they represent a fast and efficient reaction.<sup>9</sup> Other key characteristics of a good catalyst are high product and reactant *selectivity*, meaning that the catalyst only reacts with and produces desired molecules. Unwanted side reactions can poison a system<sup>35</sup>, create side products that are difficult to separate,<sup>36</sup> or lead to a catalyst's deactivation and failure<sup>37</sup>. In terms of industrial catalysts, it is important to keep in mind the efficiency of a catalyst. To this goal, Sheldon describes the E-factor of a catalyst, defined as the ratio of undesired product to desired products.<sup>38</sup> Undesired products represent wasted energy and increased separations downstream. Different chemical sectors have different E-factors. For example, in the field of pharmaceuticals, an E-factor of 25-100 is suitable, since the desired products are quite expensive and can absorb costs associated with waste. However, in the field of bulk chemicals (which includes fuels), much smaller ratios of 1-5 are required for the economic viability of processes.<sup>38</sup> In efficient fuels catalysts, waste must be minimal.

Broadly, catalysis can be separated into several categories, including homogeneous catalysis, heterogeneous catalysis, and biocatalysis.<sup>18</sup> Homogeneous catalysis refers to when the catalyst and substrates are of the same phase, most often in the liquid phase. Conversely, heterogeneous catalysis refers to situations where the catalyst and the product are of different phases. In



industry, this typically involves a solid catalyst in liquid or gas substrate. Biocatalysis refers to enzymatic catalysis, where proteins perform reactions. Catalysts can further be separated into chemical catalysis and electrocatalysis<sup>39</sup>, which work in an electrochemical cell<sup>27</sup>. Each type of catalyst has advantages and disadvantages, which will be discussed in Chapter 6. However, in this study we will focus on homogeneous, molecular catalysts with a single metal center surrounded by organic ligands.

A recent technoeconomic analysis of H<sub>2</sub> produced by photoelectrochemical cells found that while fuel-forming catalysts were not a large portion of the overall cost, they were the least abundant component of the cells, which was cause for alarm.<sup>40</sup> In this thesis, I study the PESs and mechanisms of existing, successful fuel-forming catalysts in order to determine the source of their selectivity, high TON and TOF, and resistance to degradation. With this in mind, I will work towards design of earth-abundant catalysts. The overarching focus will be on group 9 transition metals: Co, Rh, and Ir. I will also focus on two broad ligand structures: pincer catalysts and bipyridine-based (bpy) catalysts. These catalysts are all studied with the goal of improving energy sources, both established and emerging.

### Ligand Classes

The first class of catalysts studied here are called pincer catalysts because they literally grip the metal like the pincers of a bug. A generalized form can be seen in Figure 1.4a and b.

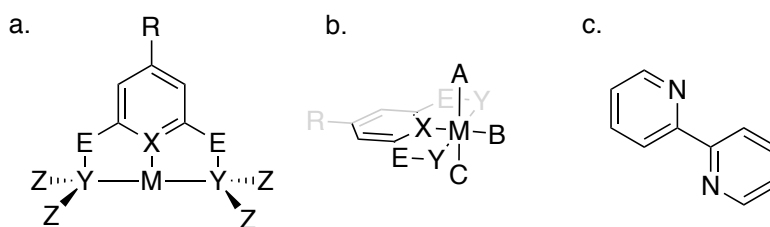


**Figure 1.4:** Schematic of a. an arbitrary pincer, b. the side view of the arbitrary pincer, and c. bipyridine.

These pincers are tridentate ligands, meaning they bind to the metal in three places. They are typically planar due to the aryl ring in the middle (though non-aryl groups can be used<sup>41</sup>), though some bending can occur along the Y-M-Y axis<sup>42</sup>. In Fig. 1.4a, we see the different positions in the pincer ligand labeled. Each position in the pincer is unique, as it modifies the electronic structure

of the catalyst in a different way.<sup>42-46</sup> The R groups can be used as a solvation aid<sup>47</sup>, or to modify the electronics at the metal center without interfering sterically. The E groups can affect bending of the pincer, as well as be used in second sphere coordination to lower reaction barriers<sup>48</sup>. The Y and Z groups can be used to affect the sterics at the metal center, creating reaction pockets or blocking reaction sites at the metal.<sup>42</sup> Finally, the X position has significant control over the coordination of groups directly across the metal (position B in Fig. 1.4b).<sup>49</sup> In many of the systems studied here, full octahedral coordination is found around the metal, meaning six groups bind. Three positions are taken up by the pincer and the other three can be seen in the side view of Figure 1.4.b. Positions A and C are referred to as the axial positions, and B is referred to as the equatorial position. One of the reasons for the pincer ligand's ubiquity in catalysis is its modular nature: since each position of the pincer has a subtle effect, these groups are routinely swapped out to tune catalysts. Part of their modularity results from the synthetic processes used to make them.<sup>43,50</sup>

The second class of catalysts that will be investigated are bipyridine (bpy) based catalysts. Bpy is a non-innocent ligand (meaning that it is able to host an electron upon reduction)<sup>51</sup> that is found in many catalytic systems<sup>52-57</sup>. It often binds with transition metals through the nitrogen groups and can also be modified, such as to make vinyl bipyridine<sup>58</sup>, though not as extensively as the pincer scaffold.

### Role of Computation

In this study, I use density functional theory as the primary tool in order to understand the PES of these catalysts. Density functional theory is rooted in the Schrodinger equation, and in this work, primarily the time-independent version.<sup>59</sup> The Schrödinger equation allows for the solution of energy levels and wave function for a collection of electrons and nuclei. It can be seen in Eq. 2.

$$\hat{H}\Psi = E\Psi \quad (2)$$

In this equation, operator  $\hat{H}$  is referred to as the Hamiltonian. In a system consisting of M nuclei and N electrons,  $\hat{H}$  in atomic units as follows:

$$\hat{H} = -\frac{1}{2} \sum_{i=1}^N \nabla_i^2 - \frac{1}{2} \sum_{I=1}^M \frac{1}{M_I} \nabla_I^2 - \sum_{i=1}^N \sum_{I=1}^M \frac{Z_I}{r_{iI}} + \sum_{i=1}^N \sum_{j>i}^N \frac{1}{r_{ij}} + \sum_{I=1}^M \sum_{J>I}^M \frac{Z_I Z_J}{r_{IJ}} \quad (3)$$

In this equation, the first two terms refer to the kinetic energy of the electrons and nuclei, respectively. The third term gives the interaction between electrons and the nuclei. The fourth and fifth terms give the interaction between pairs of electrons and pairs of nuclei, respectively. This equation can be solved exactly for the hydrogen atom and for “hydrogen-like” atoms, but additional electrons complicate the system intractably. Unfortunately, most interesting catalysis involves more than one or two electrons. Thus begins the journey into quantum chemical methods, which involves a collection of approximations made with the goal of solving the Schrödinger equation as exactly as possible for the multi-electron system.

The first major approximation is the Born-Oppenheimer Approximation, which approximates electrons as moving in a field of fixed nuclei. This is a consequence of the nuclear mass being much larger than that of the electron. This approximation reduces the problem to largely solving for electronic motion and effects, making the fifth term in Eq. 3 effectively a constant. The second major approximation is that of Hartree and Fock, which reduces the N-electron problem to N non-interacting one-electron problems, then introduces the Hartree-Fock (HF) potential to account for the electron-electron interactions. The reader is referred to the classic text by Szabo and Ostlund for further details.<sup>60</sup>

While the HF scheme was a large leap forward, it was plagued with error due to electron-electron interactions, as well issues with scaling to larger systems. In response to this, Hohenberg and Kohn proposed in their 1964 landmark theory the use of electron density rather than N-electron wave function.<sup>61</sup> This paper effectively gave birth to modern density functional theory. Through proof by contradiction, they were able to show that the electron density was a unique property of the system. It showed that the energy is functional of the 3-dimensional electron density. Previously, 3N-dimensional wave function had been used, so this represented a large improvement in scaling. It also showed that if the exact form of the functional including quantum effects, the electron-electron interaction, and kinetic energy were known, an exact solution to the Schrodinger Equation would be found.<sup>59</sup> However, it gives no information on what this functional looks like.

However, this is easier said (and proved) than done! The Kohn-Sham approach<sup>62</sup> is a direct consequence of the Hohenberg-Kohn theorems, presents a blueprint for using the theorems iteratively to find a solution. Key to this blueprint is the separation of the Hamiltonian into portions that can be solved exactly for a non-interacting system and the remaining unknown portions (primarily those involving electron-electron interactions) are collected in a term called the exchange-correlation functional. More depth on this subject can be found in Koch and Holthausen.<sup>59</sup> The exchange-correlation functional puts the functional in density functional theory, as judicious choice of functional is key to accurate results. In this thesis, I primarily use B3LYP<sup>63</sup> and M06<sup>64</sup>. Both are hybrid functionals, which combine differing amounts of Hartree-Fock exchange and an empirically-fit function to derive the functional.

From these calculations, one can derive a variety of useful characteristics of a catalytic system.<sup>59</sup> One can calculate the geometry of intermediates on the PES, as well as the geometry of transition states (with help from transition state theory<sup>28</sup>). One can also glean energies from these calculations to infer which paths will be most likely. The energies in this thesis generally are Gibbs free energies in solution, except where otherwise mentioned. In each chapter, a separate methods section is present as there are subtle differences between the methods used in each chapter.

One advantage of computation in catalysis is that small adjustments can be made to the structure of the catalyst being studied. These adjustments can be as small as rotating a piece of the molecule to see an energy change to something as large as calculating an entirely new pathway for a related catalyst with new functional groups. In each case, the atomistic states along the pathways can be seen in full detail, a luxury often not afforded to experiment.<sup>18</sup> A potential molecule can be screened for an effect without the trial of making it in the lab. Molecules that do not exist yet can be predicted and some that cannot be made at all for various experimental reasons can be made computationally as a toy system. This freedom is attractive, but as Stan Lee wrote, "With great power comes great responsibility". Errors exist in DFT calculations due to a variety of reasons including, for instance, errors in functionals<sup>65</sup>, or unforeseen side reactions<sup>37</sup> so it is important to continually validate. In this study, I have worked closely with experimental groups to create constant iteration of explanation of observations and prediction of new catalysts.

### **Common Threads and Overview**

Two overarching motifs can be seen in this thesis beyond the connection of energy sciences. The first is the capacity of small modifications in structure to have large effects on catalytic ability. Gaining a true intuition for how subtle atomic effects can improve a catalyst is the key to most chapters. This plays on one of the strengths of computational catalysis and can be used to help predict new generations of catalysts which build on the strength of previous generations. The second motif is the interplay of thermodynamics, represented by the energy of intermediates, and kinetics, represented by transition states. The connection between thermodynamics and kinetics cannot be stressed enough. However, while thermodynamics may dictate the overall boundaries of possibility for a catalytic system, kinetics dictate which path is actually taken. The wrestling of these two effects is a hallmark of many of the catalysts studied in this work and can be seen throughout.

The outline of the thesis is as follows. Chapter 2 focuses on an iridium-based catalyst competent for C-H activation in mesitylene, a methane surrogate. This chapter includes elucidation of the mechanism for this C-H activation, as well as predictions to help the catalyst improve their competence for selective methane activation. Chapter 3 is the first of two chapters focusing on iridium and cobalt catalysts for CO<sub>2</sub> reduction to formate. This chapter centers on the mechanism by which these catalysts actually complete this reduction, as well as investigating the effects of solvent on the thermodynamics of the reaction. A key point in this chapter is how this catalyst is able to avoid the thermodynamically-preferred hydrogen evolution, which is an unwanted side reaction. Chapter 4 follows this closely with investigating how subtle atomic changes to the ligands in these catalysts affect both the thermodynamics and kinetics of the system. Chapter 5 shifts to investigating a rhodium catalyst for desired hydrogen evolution, and looks to explain an unexpected experimental result. The chapter goes on to elucidate how this catalyst makes hydrogen and how modifications on the ligand affect that path. Finally, Chapter 6 is a departure from the realm of strict homogenous molecular catalysis, instead focusing on how to make these catalysts more viable for industrial purposes. Molecular catalysts typically are more active, with less side reactions than heterogeneous catalysts, yet separation of the catalyst from product can be expensive and can render these catalysts uneconomic except in the case of specialty chemicals.<sup>18</sup> Furthermore, in the field of electrocatalysis, physical closeness of a catalyst

to an electrode can speed up processes by reducing the time required for diffusion-based electron transfer.<sup>66,67</sup> Thus, this chapter operates at the boundary between chemistry and materials science. It primarily focuses on meeting the challenge of robust attachment of bipyridine-based catalysts on Si electrodes. Much effort has been devoted to predicting new schemes for attachment.

## References

- (1) EIA; Energy, D. o., Ed. Washington DC, 2016.
- (2) EIA; Energy, D. o., Ed. Washington DC, 2016.
- (3) Lee, A.; Zinaman, O.; Logan, J.; Energy, D. o., Ed.; NREL: 2012.
- (4) EIA In *Frequently Asked Questions*; Department of Energy: 2016; Vol. 2016.
- (5) EIA; Energy, D. o., Ed. 2016.
- (6) Olah, G. A. *Angew. Chem. Int. Ed.* **2013**, *52*, 104-107.
- (7) DOE; Energy, E. E. a. R., Ed.; Department of Energy: 2016.
- (8) DOE; Energy, D. o., Ed. 2015.
- (9) *Activation of Small Molecules: Organometallic and Bioinorganic Perspectives*; Wiley-VCH, 2006.
- (10) Gray, H. B. *Nat. Chem.* **2009**, *1*, 7-7.
- (11) Lewis, N. S.; Nocera, D. G. *Proc. Natl. Acad. Sci. USA* **2006**, *103*, 15729-15735.
- (12) Lewis, N. S. *Chem. Rev.* **2015**, *115*, 12631-12632.
- (13) Wong, E. In *New York Times* New York City, 2015, p A10.
- (14) Paltsev, S.; Monier, E.; Scott, J.; Sokolov, A.; Reilly, J. *Clim. Change* **2015**, *131*, 21-33.
- (15) EPA; Agency, U. S. E. P., Ed. Office of Atmospheric Programs, 2015.
- (16) DOE; OFE, Ed.; Vol. 2016.
- (17) Chung, L.-H.; Chan, S.-C.; Lee, W.-C.; Wong, C.-Y. *Inorg. Chem.* **2012**, *51*, 8693-8703.
- (18) Rothenberg, G. *Catalysis: Concepts and Green Applications*; Wiley-VCH: Weinheim, 2008.
- (19) Lashof, D. A.; Ahuja, D. R. *Nature* **1990**, *344*, 529-531.
- (20) Chung, D.; Davidson, C.; Fu, R.; Ardani, K.; Margolis, R.; NREL, Ed. 2015.
- (21) Dunn, B.; Kamath, H.; Tarascon, J.-M. *Science* **2011**, *334*, 928-935.
- (22) DOE 2014.
- (23) Solis, B. H.; Maher, A. G.; Dogutan, D. K.; Nocera, D. G.; Hammes-Schiffer, S. *Proc. Natl. Acad. Sci. USA* **2016**, *113*, 485-492.
- (24) Halpern, J.; Peters, E. J. *Chem. Phys.* **1955**, *23*, 605-605.
- (25) Schwarz, H. A.; Dodson, R. W. *J. Phys. Chem.* **1989**, *93*, 409-414.
- (26) Aresta, M. *Carbon Dioxide Reduction and Uses as a Chemical Feedstock*; Wiley-VCH: Weinheim, Germany, 2006.
- (27) Costentin, C.; Robert, M.; Saveant, J.-M. *Chem. Soc. Rev.* **2013**, *42*, 2423-2436.
- (28) Truhlar, D. G.; Garrett, B. C.; Klippenstein, S. J. *J. Phys. Chem.* **1996**, *100*, 12771-12800.
- (29) Beynon, J. H.; Gilbert, J. R. *Application of transition state theory to unimolecular reactions : an introduction*; Wiley, 1984.
- (30) Arrhenius, S. *Zeit. Phys. Chem.* **1899**, *28*, 317.
- (31) Eyring, H. *Chem. Rev.* **1935**, *17*, 65-77.
- (32) Connors, K. A. *Chemical Kinetics: The Study of Reaction Rates in Solution*; Wiley-VCH, 1990.
- (33) Marin, G. B.; Yablonsky, G. S. *Kinetics of Chemical Reactions: Decoding Complexity*; Wiley-VCH, 2011.
- (34) *Transition State Modeling for Catalysis*; Truhlar, D. G.; Morokuma, K., Eds.; American Chemical Society, 1999.
- (35) Periana, R. A.; Taube, D. J.; Gamble, S.; Taube, H.; Satoh, T.; Fujii, H. *Science* **1998**, *280*, 560.
- (36) Taheri, A.; Berben, L. A. *Chem. Comm.* **2016**, *52*, 1768-1777.
- (37) Young, K. J. H.; Oxgaard, J.; Ess, D. H.; Meier, S. K.; Stewart, T.; Goddard, I. I. W. A.; Periana, R. A. *Chem. Comm.* **2009**, *0*, 3270-3272.
- (38) Sheldon, R. A. *J. Chem. Technol. Biotechnol.* **1997**, *68*, 381-388.
- (39) Bard, A. J.; Faulkner, L. R. *Electrochemical Methods: Fundamentals and Applications*; 2nd ed., 2001.
- (40) Shaner, M. R.; Atwater, H. A.; Lewis, N. S.; McFarland, E. W. *Energy Environ. Sci.* **2016**, *9*, 2354-2371.
- (41) Polukeev, A. V.; Marcos, R.; Ahlquist, M. S. G.; Wendt, O. F. *Organometallics* **2016**, *35*, 2600-2608.
- (42) Roddick, D. M. In *Organometallic Pincer Chemistry*; van Koten, G., Milstein, D., Eds.; Springer Berlin Heidelberg: Berlin, Heidelberg, 2013, p 49-88.
- (43) Choi, J.; MacArthur, A. H. R.; Brookhart, M.; Goldman, A. S. *Chem. Rev.* **2011**, *111*, 1761-1779.
- (44) van der Boom, M. E.; Milstein, D. *Chem. Rev.* **2003**, *103*, 1759-1792.
- (45) Morales-Morales, D.; Jensen, C. M.; Elsevier: Amsterdam, 2007.
- (46) *Organometallic Pincer Chemistry*; van Koten, G.; Milstein, D., Eds.; Springer, 2013.
- (47) Kang, P.; Meyer, T. J.; Brookhart, M. *Chem. Sci.* **2013**, *4*, 3497-3502.

- (48) Schmeier, T. J.; Dobreiner, G. E.; Crabtree, R. H.; Hazari, N. J. *Am. Chem. Soc.* **2011**, *133*, 9274-9277.
- (49) Wang, D. Y.; Choliy, Y.; Haibach, M. C.; Hartwig, J. F.; Krogh-Jespersen, K.; Goldman, A. S. *J. Am. Chem. Soc.* **2016**, *138*, 149-163.
- (50) Albrecht, M.; van Koten, G. *Angew. Chem. Int. Ed.* **2001**, *40*, 3750-3781.
- (51) Saji, T.; Aoyagui, S. *J. Electroanal. Chem. Interfacial Electrochem.* **1975**, *58*, 401-410.
- (52) Blakemore, J. D.; Hernandez, E. S.; Sattler, W.; Hunter, B. M.; Henling, L. M.; Brunschwig, B. S.; Gray, H. B. *Polyhedron* **2014**, *84*, 14-18.
- (53) Bolinger, C. M.; Story, N.; Sullivan, B. P.; Meyer, T. J. *Inorg. Chem.* **1988**, *27*, 4582-4587.
- (54) Chardon-Noblat, S.; Deronzier, A.; Ziessel, R.; Zsoldos, D. *J. Electroanal. Chem.* **1998**, *444*, 253-260.
- (55) Hawecker, J.; Lehn, J. M.; Ziessel, R. *Chem. Commun.* **1984**, 328-330.
- (56) Ishida, H.; Tanaka, H.; Tanaka, K.; Tanaka, T. *Chem. Commun.* **1987**, 131-132.
- (57) Young, K. J. H.; Mironov, O. A.; Periana, R. A. *Organometallics* **2007**, *26*, 2137-2140.
- (58) Lattimer, J. R. C.; Blakemore, J. D.; Sattler, W.; Gul, S.; Chatterjee, R.; Yachandra, V. K.; Yano, J.; Brunschwig, B. S.; Lewis, N. S.; Gray, H. B. *Dalton T.* **2014**.
- (59) Koch, W.; Holthausen, M. C. *A Chemist's Guide to Density Functional Theory*; 2nd ed.; Wiley-VCH: Weinheim, 2001.
- (60) Szabo, A.; Ostlund, N. S. *Modern Quantum Chemistry: Introduction to Advanced Electronic Structure Theory*; Dover: Mineola, NY, 1996.
- (61) Hohenberg, P.; Kohn, W. *Phys. Rev.* **1964**, *136*, B864-B871.
- (62) Kohn, W.; Sham, L. J. *Phys. Rev.* **1965**, *140*, A1133-A1138.
- (63) Lee, C. T.; Yang, W. T.; Parr, R. G. *Phys. Rev. B* **1988**, *37*, 785-789.
- (64) Zhao, Y.; Truhlar, D. G. *Theor. Chem. Acc.* **2008**, *120*, 215-241.
- (65) Zhao, Y.; Truhlar, D. G. *J. Chem. Theory Comp.* **2009**, *5*, 324-333.
- (66) Abbruña, H. D. *Coord. Chem. Rev.* **1988**, *86*, 135-189.
- (67) Wrighton, M. S. *Science* **1986**, *231*, 32-37.



*Chapter 2*C-H ACTIVATION MECHANISMS IN NNC AND NCN PINCER  
COMPLEXES: A COMPUTATIONAL STUDY

With contributions from Robert J. Nielsen, Meng Zhou, Alan Goldman,  
and William A. Goddard III

*Some material adapted from:*

M. Zhou, M., **S.I. Johnson**, Y. Gao, T.J. Emge, R.J. Nielsen, W.A. Goddard III, A.S. Goldman, Activation and Oxidation of Mesitylene C–H Bonds by (Phebox)Iridium(III) Complexes. *Organometallics*. 2015. 34, 2879–2888

**Introduction**

Methane co-captured with liquid hydrocarbons in “stranded” (geographically-isolated) wells presents a daunting technical issue. The infrastructure at these wells is tailored to handle liquid products, rather than gaseous methane. In response, this natural gas is typically either flared releasing CO<sub>2</sub> or directly released as methane into the atmosphere. This is environmentally treacherous as both gasses contribute directly to global warming.<sup>1</sup> In response, gas-to-liquid (GTL) technologies have been proposed as a way to efficiently use the methane at hand. Conventional steam-refining of methane (SRM) occurs at temperatures greater than 900 °C, requiring the use of expensive materials for reactors.<sup>2</sup> The result is that over 65% of the cost of constructing a SRM plant goes to capital costs, making it impractical for use in these stranded wells.<sup>2</sup> In fact, current GTL technologies are only competitive in cases defined by US Energy Information Administration as “High Oil Price” cases: where oil prices spike to higher than \$200 per barrel.<sup>3</sup> Low-cost, low-temperature catalytic conversion of methane to methanol would be the ideal solution in isolated locations since methanol is a liquid at room temperature, making it easy to transport to population centers.<sup>4</sup> It can be used directly or in a methanol fuel cell.<sup>4</sup> Previous work towards this goal has been far-reaching, involving a wide variety of metals and ligand platforms.<sup>5-11</sup> Key discoveries include Shilov’s Pt complex, which unfortunately involved irreversible decomposition.<sup>12</sup> Periana’s bipyrimidine Pt complex displayed a high yield, as well as introducing a product protection scheme. In this catalyst, a methyl ester is made rather than methanol. The higher stability of the methyl ester protects the product from over-oxidation.<sup>13</sup> However, this catalyst also was plagued by decomposition. Efforts to avoid this decomposition included moving to less-electrophilic iridium with the hope of less degradation in the presence

of water. Computational chemistry has been used previously to identify potential iridium-based candidates for catalytic activity<sup>14</sup> as well as to improve existing catalysts. Crucial to improving C-H functionalization catalysts is understanding how existing catalysts function and why they fail to meet turnover frequency and turnover number (TOF and TON, respectively) or selectivity criteria. This involves understanding where potential failure points exist in the mechanism. Gaining this understanding is a strength of computational chemistry, since atomic states along the full potential energy surface can be explored.

Methane oxidation to methanol can be separated into two parts: C-H activation, where the methyl bond is cleaved, and functionalization, where the new functional group is bound to methane. In the case of methanol, this functional group is a hydroxyl group, but other groups can be used in product protection schemes.<sup>15</sup> Two broad modes of C-H activation catalyzed by organometallic iridium have been observed. Heterolytic cleavage of C-H bonds involving Ir<sup>III</sup> and a coordinated base yields an Ir<sup>III</sup>-R bond and coordinated “XH.”<sup>16,17</sup> Alternatively, Ir<sup>V</sup> oxo motifs are known to convert alkanes to alcohols without a metal alkyl intermediate. There is evidence that these reactions proceed either via hydrogen atom abstraction and an alkyl radical<sup>18</sup> or via the concerted insertion of a singlet Ir-oxene into the C-H bond.<sup>19</sup>

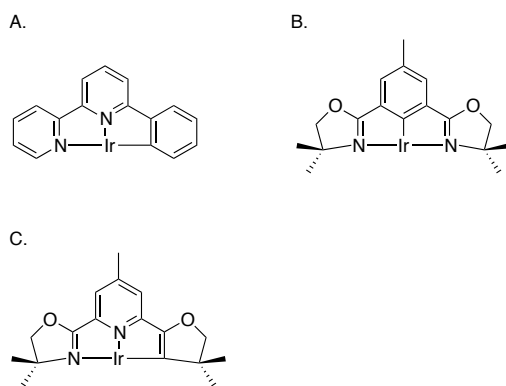


**Figure 2.1:** a. (NNC)Ir, b. (NCN)Ir (PheBox or NCN) ligand, c. theoretical NCN ligand (*t*NCN)

An organometallic catalyst must be able to activate the strong C-H bonds in methane, resist oxidation by the requisite oxidant to a state inactive toward C-H activation, facilitate the formation of carbon-heteroatom bonds (functionalization) from an Ir-CH<sub>3</sub> intermediate, and react with methane faster than products. Functionalization of methane and alkanes has been

seen in a variety of systems<sup>13,15,20</sup> and may proceed through either electrophilic attack of the oxidant on the Ir-C bond or by reductive elimination from an oxidation state of Ir higher than Ir<sup>III</sup>. However, this is out of the scope of the present study.

In this study, two iridium complexes competent for non-radical C-H activation are studied computationally to determine how alterations to their structure can extend their lifetime and activity. Both catalysts are pincer complexes, so modular changes to the structure are feasible, making these systems ideal for study.<sup>21</sup> (NNC)Ir<sup>III</sup>(TFA)(C<sub>2</sub>H<sub>4</sub>)Et (Figure 2.1a, NNC =  $\eta^3$ -6-phenyl—4,4'-di-tert-butyl-2,2'-bipyridine) catalyzes H/D exchange between 35 atm CH<sub>4</sub> and solvent trifluoroacetic acid (HTFA) at 180 °C with a TOF of 2.12 x 10<sup>-2</sup> s<sup>-1</sup>. In the presence of 0.4207 mmol oxidant at 180 °C, methane is converted to methyltrifluoroacetate, but the catalyst decomposes on a similar timescale so that a low TON (6.3) is achieved.<sup>15</sup> The NNC framework resulted from a quantum-mechanical rapid prototyping process<sup>14</sup> that screened putative catalysts by activation barriers for H<sub>3</sub>C-H activation, redox and M-CH<sub>3</sub> functionalization reactions followed by synthetic elaboration to aid synthesis of the  $\eta^3$  complex.<sup>15</sup> The second iridium complex, bis(oxazolonyl)phenyl iridium (NCN or Phebox, Figure 2.1b), was shown to dehydrogenate octane<sup>22</sup> and catalytically activate benzene and various alkanes in benzene and alkane solvent<sup>23</sup> and has been investigated previously in methane activation.<sup>24</sup> These catalysts are named NNC and NCN due to the order in which the terdentate pincer binds to the metal. First, we will investigate experimental results and mechanisms using two monodentate ligands, acetate (OAc) and trifluoroacetate (TFA), in conjunction with the NCN catalyst. In these studies, mesitylene is used as a liquid-phase methane surrogate, as it provides three alkyl sp<sup>3</sup> methyl groups for reaction. This study is followed by the comparison between NNC and NCN ligands for C-H activation in methane, as well as predictions for future iterations on this catalyst.

## Methods

Geometry optimization, frequency, and solvation calculations were completed using the B3LYP hybrid functional<sup>25,26</sup> with Los Alamos small core potentials<sup>27</sup> and 2- $\zeta$  basis set on Ir and 6-31G\*\* on organics.<sup>28,29</sup> Single point energies were calculated using the M06 functional<sup>30</sup> with the LACV3P\*\*++ basis set with augmented *f*-functions and diffuse functions on iridium.<sup>31</sup> All other atoms were calculated using the 6-311G\*\*++ basis set.<sup>32,33</sup> Solvation energies in benzene and

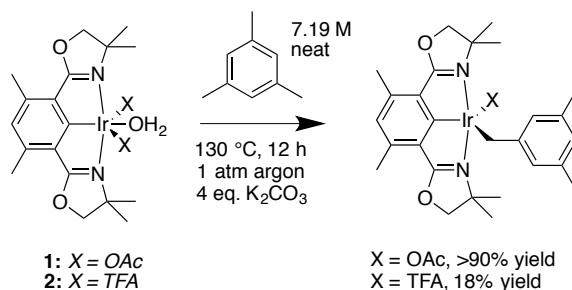
trifluoroacetic acid (TFAH) were calculated using the Poisson-Boltzmann polarizable continuum model. Dielectric constant of 2.238 and probe radius of 2.60 Å were used for solvation in benzene. Free energies of liquid benzene and TFAH were obtained by calculating the 1 atm free energy and subtracting the empirical free energy of vaporization (1.4<sup>34</sup> and 1.1<sup>35</sup> kcal/mol, respectively). In order to validate transition state geometries, analytical frequency calculations were performed. Free energies were calculated with the following equation:

$$G = E_{M06} + G_{solv} + E_{ZPE} + H_{vib} + H_{TR} - T(S_{vib} + S_{elec})$$

where  $G_{solv}$  is the energy of solvation,  $E_{ZPE}$  is the zero point energy correction,  $H_{TR}$  and  $S_{TR}$  are the rotational and translational enthalpy and entropy, and  $H_{vib}$  and  $S_{vib}$  are the vibrational enthalpy and entropy, respectively. The electronic portion of the entropy is included in the  $S_{elec}$  term. The enthalpic and entropic contributions are provided by the frequency calculations. In the case of one-electron and two-electron oxidation, one quarter and one half equivalent of  $O_2$  was used as the oxidant at a potential of 1.2 V vs NHE, respectively. In order to calculate reaction energies involving  $Ag_2O$ , DFT calculations were performed using  $O_2$  (1 atm) as oxidant, then corrected using the difference between the standard potentials for the reduction of  $O_2$  to water (1.23 V vs NHE) and  $Ag_2O(s)$  to  $Ag(s)$  and water (1.17 V vs NHE).<sup>36</sup> 1.4 kcal/mol per electron was added to the values obtained using  $O_2$  as the oxidant. Previous studies have shown good agreement between these computational methods and experiment.<sup>37,38</sup> All calculations were done in Jaguar.<sup>39</sup>

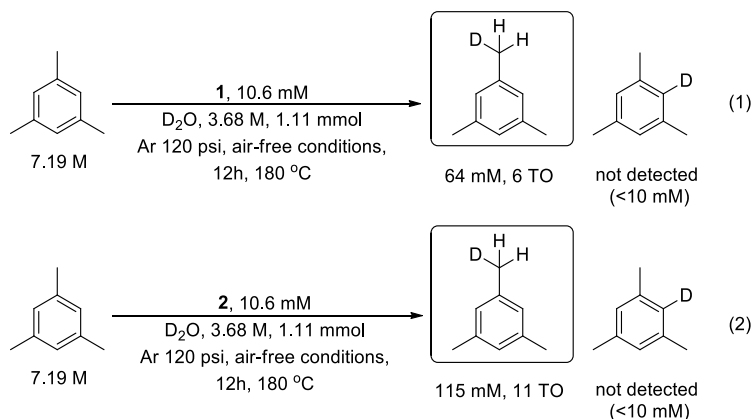
## Results and Discussion

### *Mesitylene Activation and Functionalization by the NCN pincer*



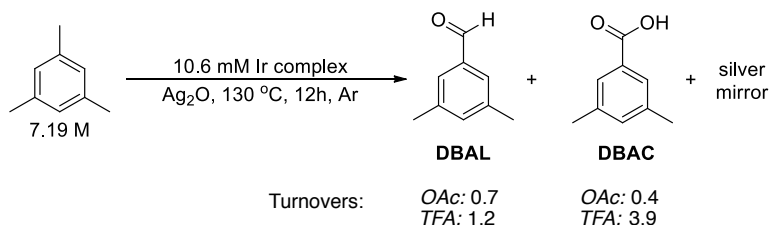
**Scheme 2.1:** Binding of mesitylene in the (NCN) catalyst shows sensitivity to the X ligand, with X = OAc giving over 90% yield and TFA showing approximately 18% yield.

Experiments were graciously done by Meng Zhou and coworkers at the Goldman Group of Rutgers University. Relevant results are summarized here, but for full experimental details, the reader is referred to the corresponding paper.<sup>40</sup> Scheme 2.1 shows the results of C-H activation of the  $sp^3$  hybridized carbon of mesitylene by the aquo analogue of NCN with 4 equivalents of  $K_2CO_3$  at elevated temperatures. While the mechanism for this reaction will be discussed *vide infra*, it can be assumed that the X ligand is lost as HX. The OAc complex (**1**) shows 90% yield of the bound mesitylene group; however, the TFA analogue (**2**) only shows 18% yield.



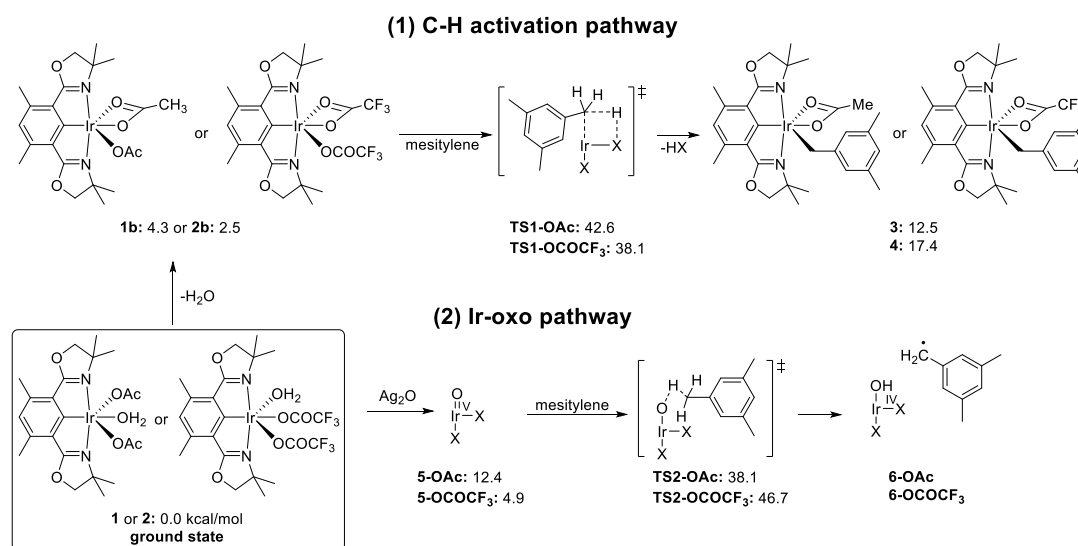
**Scheme 2.2:** Results of H/D exchange reactions, showing that the TFA analogue undergoes approximately twice as many turnovers as the OAc analogue.

Despite the lower yield of the bound mesitylene complex, the **2** ligand (TFA) shows nearly twice as many turnovers in H/D exchange experiments than **1** (OAc) in  $D_2O$  at elevated temperatures (Scheme 2.2). No benzylic H/D exchange was detected within the limits of the experiments. This result implies that at some point even in the TFA complexes, mesitylene is bound to the Ir center.



**Scheme 2.3:** Ratios of aldehyde (DBAL) to carboxylic acid (DBAC) product for the OAc and TFA analogues.

The reaction shown in Scheme 2.3 further corroborates mesitylene is bound at some point. In both cases 3,5-dimethylbenzaldehyde (**DBAL**) and 3,5-dimethylbenzoic acid (**DBAC**) are formed in differing ratios. In **1**, more aldehyde than carboxylic acid is formed, implying that less over-oxidation occurs. However, there is only 1.1 turnover of total product formed. In the case of **2**, three times the DBAC is formed than DBAL, implying more over-oxidation. However, multiple turnovers of product are formed. In order to improve this catalysts ability to functionalize mesitylene (as a first step to understanding methane oxidation), a computational mechanistic search was undertaken.



**Scheme 2.4.** Calculated free energies (kcal/mol) for (1) C-H activation pathway and (2) Ir-oxo pathway in catalytic mesitylene oxidation using complexes **1** or **2**; X = OAc or OCOCF<sub>3</sub>; “Phebox” ligand was not shown but was implied, except in complexes **1**, **2**, **3**, and **4**; no calculations performed for **6-OAc** and **6-OCOCF<sub>3</sub>**

Two proposed pathways for mesitylene C-H bond activation by complexes **1** and **2** are shown in Scheme 2.4. The experimentally prepared aquo complexes were taken as the ground states for all calculations. Two different ground states were calculated for the two coordinating ligands. In complex **1**, the ground state for the acetate complex, the coordinated aquo ligand prefers to occupy the equatorial position, whereas in complex **2**, the ground state for the trifluoroacetate complex, the aquo ligand prefers the axial position. In pathway (1), C-H activation of mesitylene

proceeds *via* **TS1** with binding of the benzylic carbon to iridium occurring concertedly with hydrogen transfer to the oxygen of the anionic ligand (a concerted metalation-deprotonation or CMD mechanism).<sup>36,41,42</sup>

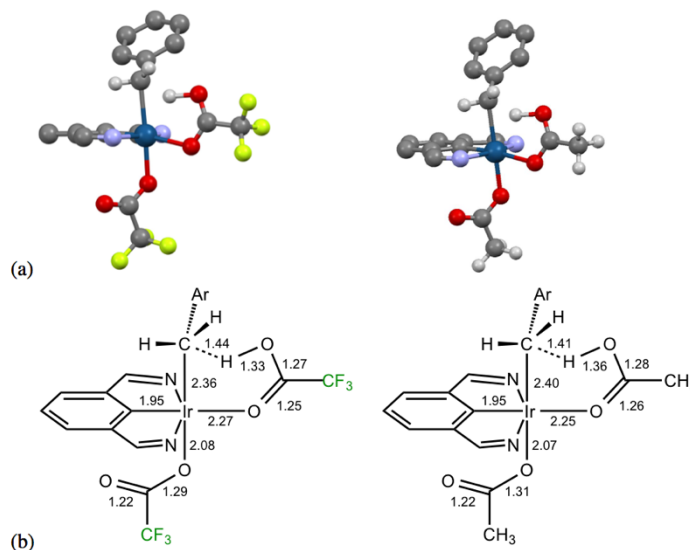


**Figure 2.2:** (a) Calculated structure of **TS1-OCOCF<sub>3</sub>** and **TS1-OCOCH<sub>3</sub>** (peripheral atoms omitted for clarity) (b) Selected interatomic distances indicated (Å)

In C-H activation by complex **1**, the transition state **TS1-OAc** has an activation barrier of 42.6 kcal/mol. The trifluoroacetate analog, **TS1-OCOCF<sub>3</sub>** (Fig. 2.2), is lower in free energy, 38.1 kcal/mol. Proceeding along the reaction coordinate from **TS1**, the acetic acid or trifluoroacetic acid (HX) molecule is eliminated to give complex **3** or **4**. Notably, although **TS1-OAc** has a higher energy than **TS1-OCOCF<sub>3</sub>**, formation of the reaction product, **3** (from **TS1-OAc**), is significantly less endergonic than formation of complex **4** (from **TS1-OCOCF<sub>3</sub>**) (by 6.2 kcal/mol). These transition states and relevant bond lengths can be seen in Figure 2.2. Thus the calculations are consistent with both the faster kinetics of H/D exchange catalyzed by **2** vs. **1**, and the observations indicating that C-H activation by **2** to give the mesityl complex **4** is thermodynamically less favorable than the reaction of **1** to give **3**. It should be noted however that the calculated differences in both the reaction kinetics and thermodynamics are much greater than is indicated by the experimental results.

Once formed, complexes **3** or **4** may undergo a variety of possible routes discussed in the literature to form a C-O bond;<sup>43,44</sup> the complexity of such reactions, particularly with Ag<sub>2</sub>O as oxidant, is beyond the scope of this work. An alternative oxidation pathway begins with the direct oxidation to give Ir-oxo complexes **5**. Iron, manganese, and ruthenium oxo complexes typically can undergo a fast hydrogen abstraction reaction with alkanes, often leading to over-oxidation.<sup>45,46</sup> This reaction yields a carboradical and Ir<sup>IV</sup> hydroxide complex, shown in **6**. The formation of **5-OAc** is uphill from **1** by 12.4 kcal/mol, while the formation of **5-OCOCF<sub>3</sub>** is only uphill from **2** by 4.9 kcal/mol.

The transition state for hydrogen abstraction by the oxo group is shown by **TS2**. At 38.1 kcal/mol, the calculated barrier for hydrogen abstraction by Ir-oxo complex **5-OAc**, *via* transition state **TS2-OAc**, is lower than **TS2-OCOCF<sub>3</sub>** (46.7 kcal/mol), by 8.6 kcal/mol. Given that the trifluoroacetate complex **2** is the more effective catalyst for oxidation, and given that a calculated comparison of two such closely analogous transition states should be quite reliable, this argues strongly against the oxo pathway (at least for catalysis by complex **2**). In marked contrast, for the C-H activation pathway, **TS1-OCOCF<sub>3</sub>** is significantly lower than **TS1-OAc**, in accord with the observation that complex trifluoroacetate complex **2** catalyzes both oxidation and H/D exchange faster than complex **1**.

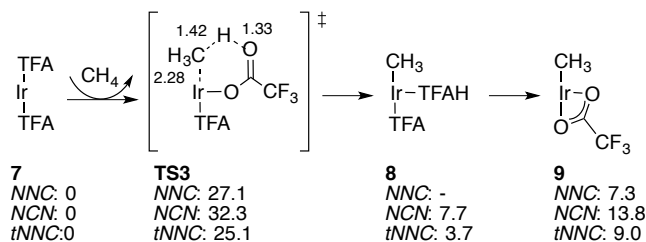
Thus the calculations predict that the trifluoroacetate ligand favors the kinetics of C-H activation (in accord with the faster H/D exchange) as compared with the acetate ligand, while it disfavors the oxo pathway. This may suggest that trifluoroacetate in this type of system is more promising than acetate for C-H functionalization, since the oxo pathway (if operative) is less likely to afford the intriguing selectivity that is offered by transition-metal catalyzed C-H activation.<sup>45</sup> As such, all further comparison will be using TFA as the monodentate ligand.

#### *Comparison of NNC and NCN pincer systems*

Free energy surfaces for the heterolytic activation of methane by both the NNC and NCN catalysts are seen in Scheme 2.5. The mechanism proceeds by the non-aquo complex **7**, concertedly transferring a proton from methane to coordinated trifluoroacetate and binding carbon to iridium in the CMD scheme, as shown by **TS3**. The protonated TFA is then released by the catalyst and the remaining TFA forms a  $\kappa^2$  bond to the iridium to form **9**. The structure



for **9** has been observed experimentally in benzene and alkane activation by Ito et al.<sup>23</sup>, supporting this mechanism. Comparing the transition state and intermediate energies, the NNC catalyst has a lower activation barrier of 27.1 kcal/mol, lower when compared to the NCN catalyst, which has an activation barrier of 32.3 kcal/mol. Both of these activation energies are accessible in the temperatures used for methane activation. The free energy for **9** is similarly higher in the NCN catalyst than the NNC catalyst, suggesting it may be difficult to isolate.<sup>40</sup>

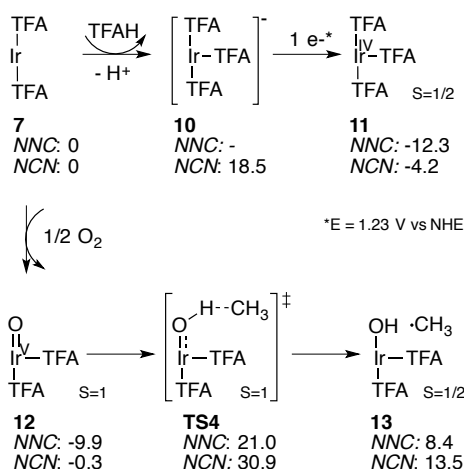


**Scheme 2.5:** Methane activation occurs in this scheme by concerted metalation/deprotonation. Due to the decreased *trans* influence, the NNC complex yields the lowest barrier.

A problem that has plagued these catalysts is the formation of an oxidized, deactivated Ir<sup>IV</sup> state<sup>46</sup>, which features three bound TFA molecules as seen in Scheme 2.6. The free energies of the Ir<sup>IV</sup> intermediates **11** are calculated using O<sub>2</sub> as an oxidant. The NNC catalyst forms **11**<sup>NNC</sup> quite easily, as it is downhill from the resting state **7** by 12.3 kcal/mol. This suggests that this state provides a thermodynamic sink. In contrast, **11**<sup>NCN</sup> is downhill by 4.2 kcal/mol from the resting state, but is less exergonic than the NNC ligand. In this sense, the NCN catalyst performs better in that it is more resistant to oxidation by one electron over a wider range of oxidation potentials, as seen experimentally, though is still exergonic to form.<sup>40</sup> In fact, this state may be one reason for the limited turnovers for Phebox in the previously-described mesitylene activation and functionalization.

Another undesired reaction that can occur is the formation of an Ir<sup>V</sup> oxo, which can then participate in hydrogen atom transfer (HAT) reactions. Radical activation is undesirable because it is typically unselective among C-H bonds and can therefore lead to over-oxidation to CO<sub>2</sub>.<sup>45</sup> This reaction should be avoided if the goal is selective oxidation of methane. The free energy surface for radical fast hydrogen transfer can be seen in Scheme 2.6. After the Ir<sup>V</sup>-oxo, **12**, is formed, methane transfers a hydrogen through a radical mechanism to the oxygen, yielding an

iridium hydroxide complex and a radical methyl group. The methyl group then quickly bonds with the hydroxide. In the NNC catalyst, the oxo represents a potential resting state for the system, as formation is still exergonic by -9.9 kcal/mol, whereas the NCN oxo complex is thermally neutral with the previous ground state **7**. The transition state barrier, **TS4**, is uphill 21 kcal/mol for the NNC catalyst from **7**<sup>NNC</sup>, and is uphill by 30.9 kcal/mol from the new assumed resting state of **12**<sup>NNC</sup>. In the NCN system, **TS4**<sup>NCN</sup> is uphill 30.9 and 31.2 kcal/mol from states **7** and **12**, respectively. From their respective resting states, the NNC and NCN systems have similar HAT barriers. These barriers are also competitive with **TS3**, suggesting oxidation may be a competitive process in non-radical methane activation.

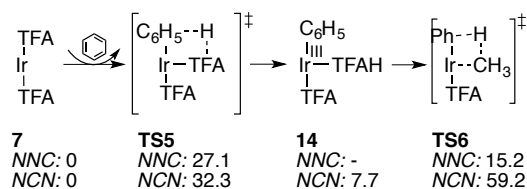


**Scheme 2.6:** Two undesired pathways are shown. The top pathway displays the deactivated Ir<sup>IV</sup> complex and the lower pathway shows the formation of the iridium oxo complex.

The barrier for formation of the oxo is not calculated. This barrier is assumed to be quick due to work by Brown et al<sup>47</sup>, which proposed a bimolecular reaction in trimesityliridium, where two iridiums bond with dioxygen, cleaving the bond. This mechanism is supported kinetically by second order reaction rates with respect to iridium. No intermediate has been seen, which suggests that this reaction proceeds quickly.<sup>47</sup> If this is the case, then the formation of **TS3** is the rate-limiting step and the energies of **12** are indicative of the tendency to proceed through the radical pathway.

In benzene, phenyl activation can occur as a competing reaction. Alternatively, the activation of benzene could provide a mediated pathway that lowers the activation barrier for methane, as

can be seen in Scheme 2.7. In this mechanism, benzene is first activated in a manner similar to methane. Subsequently, methane transfers a hydrogen to the phenyl group, which is released. The methyl group then binds to iridium. In both the NNC and NCN catalysts, the barrier for activation of benzene is lower than that of methane. Additionally, the intermediate analogous to **9** is seen experimentally in the NCN catalyst<sup>23</sup>, which provides experimental evidence for the proposed computational mechanism. The hydrogen transfer step, **TS6**, is low in energy for the NNC catalysts at 15.2 kcal/mol and is thermally accessible. However, in the NCN catalyst, the transfer is much too high in energy (59.2 kcal/mol in benzene) for the reaction to be thermally feasible. Since the phenyl-activated intermediate is seen experimentally in NCN, this may be a competing reaction. This highlights the importance of solvent choice in catalysis: choosing another solvent such as TFAH<sup>6</sup> or halogenated benzene ameliorates this problem.



**Scheme 2.7:** Activation of benzene is competitive with methane activation in both the NNC and NCN, as shown by **TS5**.

Significant differences can be seen between the pathways available to the NNC and NCN pincers. These differences can be attributed to the position of the carbon in the pincer. In the NCN case, the carbon competes for the orbital with the atoms directly across from it, frustrating bonding in the equatorial position. In the NNC system, nitrogen in the pyridine ring is less effective as a donor<sup>48</sup>, which affects the bonding of relevant methyl and TFA molecules less. This can be seen explicitly if we examine an NNC analog of Phebox, which can be seen in Figure 2.1c. This theoretical molecule is obtained by switching the position of the carbon in the pincer, but retaining the rest of the Phebox structure. Activation of methane using this theoretical pincer molecule follows the same motif as in Scheme 2.1, where it is referred to as tNNC. However, the tNNC analog has a lower free energy for molecules **9** and **11** than its NCN analog, which is to be expected based off the current hypothesis. This also agrees with other work investigating nitrogen groups in the *ipso* position to the metal.<sup>24</sup> When comparing the formation of the Ir<sup>IV</sup> deactivated complex **7**, the tNNC forms it favorably (-18.9 kcal/mol) as expected. When

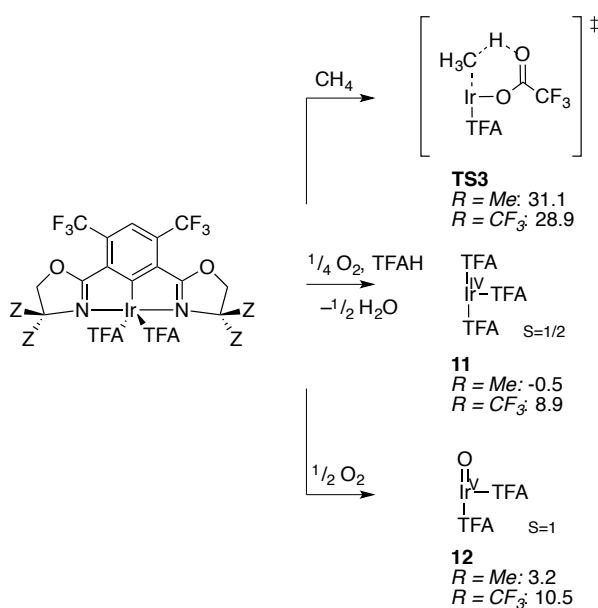
comparing bond lengths between the iridium and the oxygen of the equatorial TFA in **7**, the original NNC molecule has a length of 2.16 Å, while the tNNC molecule forms a shorter bond length of 2.07 Å. The increased bond length when C is *trans* to the TFA is expected because competition for the orbital is a determining factor in the behavior of Phebox as a catalyst.

The strong influence of the *trans* effect explains much of the other observed behavior of the NNC catalyst. In the phenyl-mediated activation pathway **TS6**, the two carbons *trans* to one another frustrate the molecule, leading to an increased transition state energy. It also increases the energy **11**: having three TFA groups bound to the iridium is unfavorable because one of the TFAs must reside opposite the C-Ir bond. Finally, the effect is also seen in the ground state. In the NNC system and in other molecules the TFA will form a  $\kappa^2$  bond with the Ir. However, in the NCN system, the bond with the TFA group is only to a single oxygen, or  $\kappa^1$ , despite their orientations being similar. This suggests again the important effect that the carbon in the pincer has on the position *trans* to it.

With this information about the importance of the *ipso* carbon in hand, the pincer can be modified in order to lower the barrier for CMD (**TS3**), while raising the energy of undesired intermediates **11** and **12**. Increased competition for the orbital shared by the *ipso* carbon and the equatorial position disfavors undesired states; increased electron density in this position may improve performance. Directing groups on the phenyl backbone can be used in order to achieve this goal. For example, CF<sub>3</sub> groups are *meta*-directing,<sup>49</sup> so hypothetically these groups could be used to modify electron density at the *ipso* carbon if cleverly placed. Computational results of this prediction can be seen in Scheme 2.8.

Upon adding CF<sub>3</sub> groups to the *meta* positions of the pincer (CH<sub>3</sub> groups in the Z groups), the barrier for CMD is lowered by approximately 1 kcal/mol, a negligible amount. More promising, however, is the increase in energy of intermediates **11** and **12**. Whereas in the unmodified example, the formation of the deactivated complex **11** was exergonic (-4.2 kcal/mol), but with appropriate CF<sub>3</sub> groups is now thermoneutral. Complex **12** is also more endergonic to form. The situation can further be improved by using R = CF<sub>3</sub> in addition the CF<sub>3</sub> *meta* substitution, fully trifluoromethylating the catalyst. The barrier for **TS3** is further decreased to 28.9 kcal/mol, and the energy for **11** and **12** now significantly endergonic. The effect of the Z group can be attributed to the electron withdrawing nature of CF<sub>3</sub> groups<sup>50</sup>, as it removes electron

density from the Ir center and gently tunes the catalyst to be slightly more electrophilic. This could potentially hit a sweet spot between the less electrophilic, non-fluorinated Ir complex and the more electrophilic noble metals previously used.<sup>12</sup> Additionally, the CF<sub>3</sub> groups may have an electrostatic effect, as they may repel the oxygen of TFA, making it more difficult to coordinate.<sup>51</sup> While Ir complexes with *meta*-CF<sub>3</sub> groups<sup>52,53</sup> and Z = CF<sub>3</sub> groups<sup>51</sup> have been made independently, a complex with full trifluoromethylation may be synthetically difficult to produce. However, the above mechanistic study suggests that efforts toward these molecules could yield a very interesting catalyst and should be pursued.



**Scheme 2.8:** Use of electron withdrawing group CF<sub>3</sub> aids in lowering the barrier for CMD while also raising the energy of undesired intermediates leading to deactivation and side reactions.

## Conclusions

While the activation energy of the NNC catalyst is lower than that of NCN catalyst, the characteristics of the NCN Phebox pincer help it avoid some of the pitfalls that had previously plagued the NNC catalyst, including oxidation. However, Phebox has its own pitfalls, including an inability to transfer hydrogen between a phenyl group and methyl group, making phenyl activation a competing reaction rather than a helpful one when the catalysis is performed in benzene. Steps to avoid the formation of **12** and bias the reaction towards a non-radical pathway can be taken, including using a different oxidant and using ligand modifications presented here.

Another route is to investigate PCP ligands, which have been shown to avoid the Ir<sup>V</sup> state.<sup>54</sup>

The overarching goal is to protect these iridium catalysts from over-oxidation, while maintaining high turnover numbers. The fluorinated complexes are a potential improvement in this direction, but more work should be done to understand their ability to catalyze methane oxidation. Future work largely involves understanding functionalization better and applying this to the fluorinated ligand sets. Additionally, more reasonable oxidants than Ag<sub>2</sub>O, or even oxygen, should be considered, both for experiment and calculational work. Nonetheless, the interesting characteristics of Phebox and its fluorinated derivatives make it a potential candidate for use in methane activation.

## References

- (1) Lashof, D. A.; Ahuja, D. R. *Nature* **1990**, *344*, 529-531.
- (2) Aresta, M. *Carbon Dioxide Reduction and Uses as a Chemical Feedstock*; Wiley-VCH: Weinheim, Germany, 2006.
- (3) EIA; Energy, D. o., Ed. Washington DC, 2016.
- (4) Olah, G. A. *Angew. Chem. Int. Ed.* **2013**, *52*, 104-107.
- (5) Tenn, W. J.; Young, K. J. H.; Bhalla, G.; Oxgaard, J.; Goddard, W. A.; Periana, R. A. *J. Am. Chem. Soc.* **2005**, *127*, 14172-14173.
- (6) Ahlquist, M.; Periana, R. A.; Goddard Iii, W. A. *Chem. Comm.* **2009**, 2373-2375.
- (7) Cheng, M.-J.; Bischof, S. M.; Nielsen, R. J.; Goddard Iii, W. A.; Gunnoe, T. B.; Periana, R. A. *Dalton T.* **2012**, *41*, 3758-3763.
- (8) Crabtree, R. H. *J. Organomet. Chem* **2004**, *689*, 4083-4091.
- (9) Stahl, S. S.; Labinger, J. A.; Bercaw, J. E. *J. Am. Chem. Soc.* **1996**, *118*, 5961-5976.
- (10) Hashiguchi, B. G.; Bischof, S. M.; Konnick, M. M.; Periana, R. A. *Acc. Chem. Res.* **2012**, *45*, 885-898.
- (11) Periana, R. A.; Mironov, O.; Taube, D.; Bhalla, G.; Jones, C. *Science* **2003**, *301*, 814-818.
- (12) Shilov, A. E. *Activation of Saturated Hydrocarbons by Transition Metal Complexes*; Reidel: Dordrecht, Netherlands, 1984.
- (13) Periana, R. A.; Taube, D. J.; Gamble, S.; Taube, H.; Satoh, T.; Fujii, H. *Science* **1998**, *280*, 560.
- (14) Muller, R. P.; Philipp, D. M.; Goddard, W. A., III *Top. Catal.* **2003**, *23*, 81-98.
- (15) Young, K. J. H.; Oxgaard, J.; Ess, D. H.; Meier, S. K.; Stewart, T.; Goddard, I. I. I. W. A.; Periana, R. A. *Chem. Comm.* **2009**, *0*, 3270-3272.
- (16) Davies, D. L.; Donald, S. M. A.; Al-Duaij, O.; Macgregor, S. A.; Pölleth, M. J. *Am. Chem. Soc.* **2006**, *128*, 4210-4211.
- (17) Ess, D. H.; Nielsen, R. J.; Goddard Iii, W. A.; Periana, R. A. *J. Am. Chem. Soc.* **2009**, *131*, 11686-11688.
- (18) Groves, J. T. *J. Chem. Educ.* **1985**, *62*, 928.
- (19) Zhou, M.; Balcells, D.; Parent, A. R.; Crabtree, R. H.; Eisenstein, O. *ACS Catal.* **2011**, *2*, 208-218.
- (20) Conley, B. L.; Ganesh, S. K.; Gonzales, J. M.; Tenn, W. J.; Young, K. J. H.; Oxgaard, J.; Goddard, W. A.; Periana, R. A. *J. Am. Chem. Soc.* **2006**, *128*, 9018-9019.
- (21) Albrecht, M.; van Koten, G. *Angew. Chem. Int. Ed.* **2001**, *40*, 3750-3781.
- (22) Allen, K. E.; Heinekey, D. M.; Goldman, A. S.; Goldberg, K. I. *Organometallics* **2013**, *32*, 1579-1582.
- (23) Ito, J.-i.; Kaneda, T.; Nishiyama, H. *Organometallics* **2012**, *31*, 4442-4449.
- (24) Pahls, D. R.; Allen, K. E.; Goldberg, K. I.; Cundari, T. R. *Organometallics* **2014**, *33*, 6413-6419.
- (25) Becke, A. D. *J. Chem. Phys.* **1993**, *98*, 5648-5652.
- (26) Lee, C. T.; Yang, W. T.; Parr, R. G. *Phys. Rev. B* **1988**, *37*, 785-789.
- (27) Hay, P. J.; Wadt, W. R. *J. Chem. Phys.* **1985**, *82*, 299-310.
- (28) Francl, M. M.; Pietro, W. J.; Hehre, W. J.; Binkley, J. S.; Gordon, M. S.; Defrees, D. J.; Pople, J. A. *J. Chem. Phys.* **1982**, *77*, 3654-3665.
- (29) Hehre, W. J.; Ditchfie.R; Pople, J. A. *J. Chem. Phys.* **1972**, *56*, 2257-2261.
- (30) Zhao, Y.; Truhlar, D. G. *Theor. Chem. Acc.* **2008**, *120*, 215-241.
- (31) Martin, J. M. L.; Sundermann, A. *J. Chem. Phys.* **2001**, *114*, 3408-3420.
- (32) Krishnan, R.; Binkley, J. S.; Seeger, R.; Pople, J. A. *J. Chem. Phys.* **1980**, *72*, 650-654.
- (33) Clark, T.; Chandrasekhar, J.; Spitznagel, G. W.; Schleyer, P. V. J. *Comp. Chem.* **1983**, *4*, 294-301.
- (34) Deshpande, D. D., Pandya M.V., *Trans. Faraday Soc.* **1967**, *63*, 2149-2157.
- (35) Kreglewski, A. *Bull. Acad. Pol. Sci. Ser. Sci Chim.* **1962**, *10*, 629-633.
- (36) Pourbaix, M.; Gauthier Villars Paris, 1963.
- (37) Zhao, Y.; Truhlar, D. G. *J. Chem. Theory Comp.* **2009**, *5*, 324-333.
- (38) Young, K. J. H.; Lokare, K. S.; Leung, C. H.; Cheng, M.-J.; Nielsen, R. J.; Petasis, N. A.; Goddard III, W. A.; Periana, R. A. *J. Mol. Catal. A: Chem.* **2011**, *339*, 17-23.
- (39) Bochevarov, A. D.; Harder, E.; Hughes, T. F.; Greenwood, J. R.; Braden, D. A.; Philipp, D. M.; Rinaldo, D.; Halls, M. D.; Zhang, J.; Friesner, R. A. *Int. J. Quantum Chem.* **2013**, *113*, 2110-2142.
- (40) Zhou, M.; Johnson, S. I.; Gao, Y.; Emge, T. J.; Nielsen, R. J.; Goddard, W. A.; Goldman, A. S. *Organometallics* **2015**, *34*, 2879-2888.
- (41) Jones, C. J.; Taube, D.; Ziatdinov, V. R.; Periana, R. A.; Nielsen, R. J.; Oxgaard, J.; Goddard, W. A. *Angewandte Chemie International Edition* **2004**, *43*, 4626-4629.
- (42) Lapointe, D.; Fagnou, K. *Chem. Lett.* **2010**, *39*, 1118-1126.

- (43) Conley, B. L.; Tenn, W. J.; Young, K. J. H.; Ganesh, S. K.; Meier, S. K.; Ziatdinov, V. R.; Mironov, O.; Oxgaard, J.; Gonzales, J.; Goddard, W. A.; Periana, R. A. *J. Mol. Catal. A: Chem.* **2006**, *251*, 8-23.
- (44) Young, K. J. H.; Oxgaard, J.; Ess, D. H.; Meier, S. K.; Stewart, T.; Goddard, I. I. W. A.; Periana, R. A. *Chem. Comm.* **2009**, 3270-3272.
- (45) Labinger, J. A. *Catal. Lett.* **1988**, *1*, 371-375.
- (46) Fu, R.; Bercaw, J. E.; Labinger, J. A. *Organometallics* **2011**, *30*, 6751-6765.
- (47) Jacobi, B. G.; Laitar, D. S.; Pu, L.; Wargocki, M. F.; DiPasquale, A. G.; Fortner, K. C.; Schuck, S. M.; Brown, S. N. *Inorg. Chem.* **2002**, *41*, 4815-4823.
- (48) Wang, D. Y.; Choliy, Y.; Haibach, M. C.; Hartwig, J. F.; Krogh-Jespersen, K.; Goldman, A. S. *J. Am. Chem. Soc.* **2016**, *138*, 149-163.
- (49) Carey, F. A. *Organic Chemistry*; 7th ed., 2007.
- (50) Hansch, C.; Leo, A.; Taft, R. W. *Chem. Rev.* **1991**, *91*, 165-195.
- (51) Roddick, D. M. In *Organometallic Pincer Chemistry*; van Koten, G., Milstein, D., Eds.; Springer Berlin Heidelberg: Berlin, Heidelberg, 2013, p 49-88.
- (52) Cai, J.-G.; Yu, Z.-T.; Yuan, Y.-J.; Li, F.; Zou, Z.-G. *ACS Catal.* **2014**, *4*, 1953-1963.
- (53) Brulatti, P.; Gildea, R. J.; Howard, J. A. K.; Fattori, V.; Cocchi, M.; Williams, J. A. G. *Inorg. Chem.* **2012**, *51*, 3813-3826.
- (54) Adams, J. J.; Lau, A.; Arulsamy, N.; Roddick, D. M. *Organometallics* **2011**, *30*, 689-696.



## Chapter 3

SELECTIVITY FOR  $\text{HCO}_2^-$  OVER  $\text{H}_2$  IN THE ELECTROCHEMICAL CATALYTIC REDUCTION OF  $\text{CO}_2$  BY  $(\text{POCOP})\text{Ir}(\text{H})_2$ 

With contributions from Robert J. Nielsen and William A. Goddard III

**S.I. Johnson;** R.J. Nielsen; W.A. Goddard III. Selectivity for  $\text{HCO}_2^-$  over  $\text{H}_2$  in the Electrochemical Catalytic Reduction of  $\text{CO}_2$  by  $(\text{POCOP})\text{IrH}_2$ . *ACS Catalysis*. 2016, 6362-6371.

## Introduction

A major challenge for society is to develop energy efficient, earth-abundant catalysts that can selectively reduce  $\text{CO}_2$  to liquid fuels or other valuable organics<sup>1</sup>. Multiple paths from  $\text{CO}_2$  to liquid fuels exist, including chemical (hydrogenation)<sup>2-6</sup> and electrocatalytic (applying a sufficient voltage in a protic medium) routes. Many transition metal electrocatalysts exist to facilitate reactions generating formate or  $\text{CO}$ <sup>5-8</sup> but for most, product selectivity is an issue.

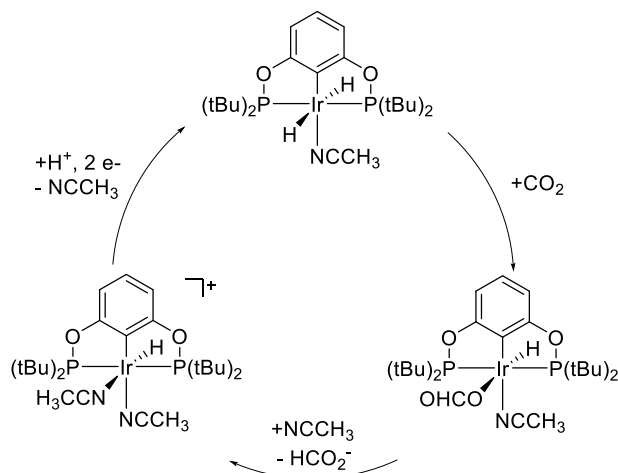


**Figure 3.1:** Meyer and Brookhart POCOP complex and their proposed mechanism

Among electrocatalysts for the  $\text{CO}_2$  reduction reaction ( $\text{CO}_2\text{RR}$ ),  $[\text{Ru}(\text{bpy})_2(\text{CO})_2]^{2+}$  has been shown to reduce  $\text{CO}_2$  to  $\text{CO}$  in acetonitrile and methanol<sup>9</sup>. Rhodium and iridium analogues of this complex have also been developed and shown to electrocatalytically produce formate, though with significant competition from hydrogen evolution.<sup>10</sup> In the case of

$[\text{Rh}(\text{bpy})_2(\text{OTf})_2][\text{OTf}]$ , Faradaic efficiencies for  $\text{H}_2$  production ranged between 5 and 20%, decreasing when water was added. Faradaic efficiency refers to the percent of electrons that go to the desired reaction versus an undesired reaction. It is essentially a quantifier for selectivity. Both Kubiak and Sauvage's work with Ni cyclam reducing  $\text{CO}_2$  to CO in water and acetonitrile shows that earth abundant metals can serve as electrocatalysts.<sup>11,12</sup> The Ni-cyclam system produced CO with 60% Faradaic efficiency and  $\text{H}_2$  at 10% Faradaic efficiency at a potential of -1.61 V. By changing the potential to -1.21 V, the  $\text{H}_2$  production was reduced to zero.<sup>11</sup> These systems illustrate the challenge posed by the thermodynamic preference for reduction of protons over  $\text{CO}_2$ .  $(\text{bpy})\text{Re}(\text{CO})_3^-$  and  $(\text{bpy})\text{Mn}(\text{CO})_3^-$  notably reduce  $\text{CO}_2$  to CO in the presence of weak acids with limited or no  $\text{H}_2$  production.<sup>13,14</sup> Some pincer complexes are also interesting in this regard, including a (PPP)Pd complex studied by Dubois that electrochemically reduced  $\text{CO}_2$  to CO, though this was in competition with HER.<sup>15</sup> Berben and coworkers' recent  $[\text{Fe}_4\text{N}(\text{CO})_{12}]^-$  system also displays high selectivity, producing formate with 96% Faradaic yield.<sup>16,17</sup> Understanding of the atomistic origin of selectivity in electrocatalysis is valuable but unclear.

An advance was the (POCOP)Ir catalyst in Figure 3.1, which Meyer and Brookhart showed reduces  $\text{CO}_2$  to formate in acetonitrile with 5% water, while wasting only 15% of the current on hydrogen generation. Hydrogen evolution was shown to be a side reaction occurring at the electrode, rather than one directly catalyzed by the metal complex.<sup>18</sup> Furthermore, by adding a quaternary amine functional group to the aryl group of the pincer, they were able to perform electrocatalytic reduction in water with only 5% Faradaic efficiency for  $\text{H}_2$  evolution, which again was determined to occur at the electrode.<sup>19,20</sup> Additionally, this catalyst can be noncovalently attached to carbon nanotubes maintaining high TON.<sup>20</sup> The mechanism of the acetonitrile/water system was studied computationally by Cao et al., who implied that regenerating an  $\text{Ir}^{\text{III}}$  dihydride involved reduction of coordinated acetonitrile rather than  $\text{Ir}^{\text{I}}$ .<sup>21</sup> Hazari et al. also explored an alternative mechanism of  $\text{CO}_2$  insertion for hydrogenation reactions, coordinating  $\text{CO}_2$  to the five-coordinate iridium dihydride complex, as opposed to Cao's hydride transfer to  $\text{CO}_2$  from  $\text{Ir}(\text{H})_2(\text{NCCH}_3)$ .<sup>22</sup> An alternative mechanism has also been suggested in which  $\text{CO}_2$  is primarily reduced by an anionic  $\text{Ir}^{\text{I}}$  hydride rather than the  $\text{Ir}^{\text{III}}$  dihydride.<sup>23</sup>

Toward the goal of understanding this unique catalyst, we report here a series of first principles density functional theory calculations including solvent effects in water to elucidate the mechanism by which CO<sub>2</sub> is reduced by the (POCOP)Ir catalyst. Our proposed mechanism, which relies on CO<sub>2</sub>RR via the Ir<sup>III</sup> hydride, is consistent with all current experiments and the surprising result that only formate is produced without HER. We examine reaction mechanisms with various proton sources leading to hydrogen generation to show that these barriers are high enough that HER is kinetically disfavored. We also investigate whether the cobalt analogue, which has been synthesized previously,<sup>24</sup> can carry out the same chemistry. We find here that the reaction barrier and overpotential are too high and that hydrogen would likely be produced. We conclude by proposing strategies for designing formate-selective CO<sub>2</sub> reduction catalysts, including an analysis of thermodynamic driving forces and the effects of solvation.

## Methods

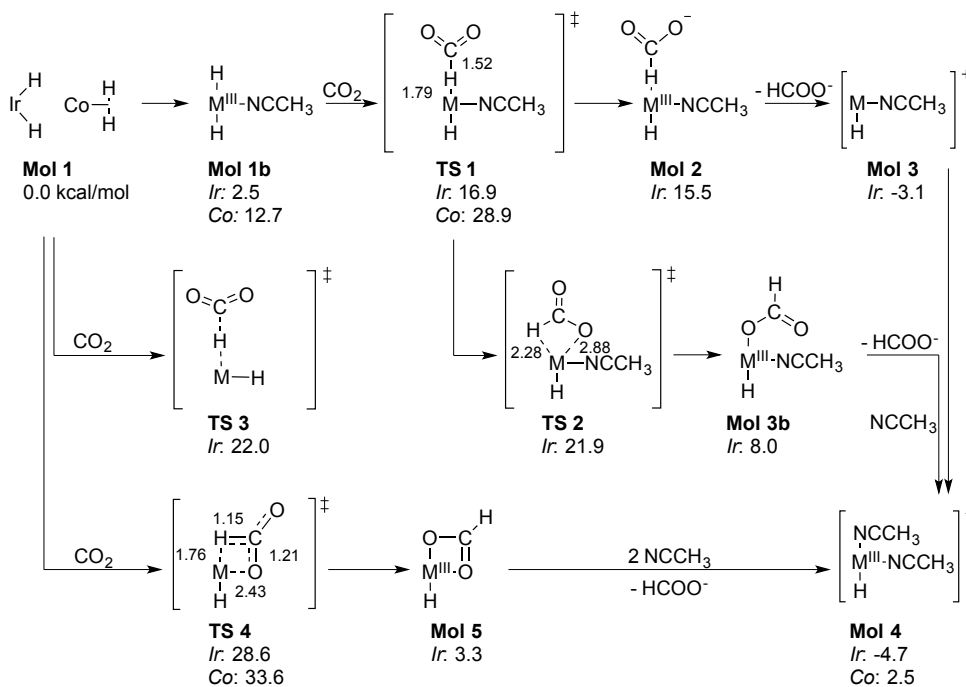
Geometry optimization, frequency, and solvation calculations were performed using the B3LYP hybrid density functional<sup>25,26</sup> with the Los Alamos small core potential<sup>27</sup> and 2- $\zeta$  basis set on metals and 6-31G\*\* on organics.<sup>28,29</sup> Single point energies were completed using the M06 functional<sup>30</sup> with LACV3P\*\*++ augmented with *f*-functions<sup>31</sup> and diffuse functions on cobalt and iridium atoms and the 6-311G\*\*++ basis on organics.<sup>32,33</sup> Solvent effects representing neat water were calculated using an implicit solvation model, using a dielectric constant of 80.37 and a solvent radius of 1.40 Å. To determine accurate free energies for solvent molecules, the 1 atm ideal gas free energy of water was computed using the appropriate statistical mechanics formulae, and the empirical free energies of vaporization (2.05 kcal/mol<sup>34,35</sup> water in water and 2.45 for 1M MeCN in water) were subtracted. The empirical solvation energy of formate in water<sup>36</sup> was used. For hydricity calculations, solvation by acetonitrile was modeled using implicit solvation with a dielectric constant of 37.5 and probe radius of 2.19 Å. Solvation of acetonitrile in acetonitrile was determined from the empirical free energy of vaporization to be 1.27 kcal/mol.<sup>37</sup>

The free energies of organometallic species were calculated using:

$$G = E_{M06} + G_{solv} + E_{ZPE} + H_{vib} + H_{TR} - T(S_{vib} + S_{elec} + S_{TR})$$

where  $G_{\text{solv}}$  is the free energy of solvation,  $E_{\text{ZPE}}$  is the zero point energy correction,  $H_{\text{TR}}$  ( $^{12}/_2 k_{\text{B}}T$ ) is the translational and rotational enthalpy, and  $S_{\text{vib}}$ ,  $S_{\text{elec}}$ , and  $S_{\text{TR}}$  are the vibrational, electronic and translational and rotational entropies, respectively. Gas phase translational and rotational entropies were modified by corrections suggested by Wertz.<sup>38</sup> For redox processes, free energies were calculated assuming an operating potential of -1.2V vs NHE. All calculations were completed in Jaguar.<sup>39</sup>

## Results and Discussion



**Scheme 3.1:** Plausible reaction pathways with calculated free energies (in kcal/mol) and bond lengths (in Ångstroms) for the Ir case.

### *CO<sub>2</sub> Conversion*

Multiple paths for the reaction of (POCOP)Ir(H)<sub>2</sub> (**Mol 1**) with CO<sub>2</sub> are shown in Scheme 3.1, along with the calculated free energies including implicit solvation by water. **Mol 1**, the reference state for all calculations, represents the catalyst sans coordinating acetonitrile.<sup>40</sup> Several transition states can be calculated without the presence of acetonitrile. In the lower pathway through **TS 4**, which outlines the mechanism described by Hazari et al.,<sup>22</sup> CO<sub>2</sub> reacts directly with the ground state of the catalyst. In this route, CO<sub>2</sub> can concertedly abstract a hydride and coordinate to the

metal through one of the oxygens at the empty octahedral position. In **Mol 5** the hydride is abstracted and the newly created formate ion is coordinated in  $\kappa^2$  fashion to the metal. Both  $\kappa^1$  and  $\kappa^2$  conformations were calculated, with  $\kappa^2$  yielding the lowest energy. Formate then dissociates and is replaced by two solvent molecules in **Mol 4**, which then must be reduced to regenerate **Mol 1**. The primary barrier for this process, **TS 4**, is thermally inaccessible at room temperature so this pathway is not likely.

An alternative pathway involves hydride transfer to an uncoordinated CO<sub>2</sub>. This can occur directly or after coordination by an acetonitrile as proposed by Cao et al.<sup>21</sup> The coordination of acetonitrile to **Mol 1** to form **Mol 1b** costs 2.5 kcal/mol. We find that constraining the H-Ir-H fragment in **Mol 1** to its linear configuration as in **Mol 1b** requires 19.6 kcal/mol of strain energy, but this is balanced by the binding of acetonitrile. This configuration forces the two hydrides to be *trans* to one another, a configuration that has been shown to be beneficial towards hydride donation<sup>1</sup>. With all octahedral positions filled, CO<sub>2</sub> can abstract a hydride directly, as shown in **TS 1**. In this transition state, the CO<sub>2</sub> has been bent to an angle of 147°, showing that donation of electron density into the  $\pi$  system of CO<sub>2</sub> has occurred. A representation of this transition state can be seen in Figure 3.2a. The barrier for this process is thermally accessible at 16.9 kcal/mol, which is far lower than **TS 4** and matches the activation energy suggested by transition state theory and the turnover frequency of 7.3 s<sup>-1</sup> derived from cyclic voltammetry (CV) data.<sup>19</sup> Alternatively, the barrier for hydride transfer directly from **Mol 1** to uncoordinated CO<sub>2</sub> is 22.0 kcal/mol, as shown in **TS 3**. In this transition state, the spectator hydride rotates closer to the equatorial position, while the active hydride stays in the axial position to be abstracted by the CO<sub>2</sub>, giving a H-Ir-H angle of 89.3°. This represents a large distortion relative to **TS 1** and increases the overall barrier. The alternative transition state wherein CO<sub>2</sub> abstracts equatorial hydride was reported by Osadchuk et al. to have a barrier of 19.0 kcal/mol, which is still higher than those involving coordination of acetonitrile.<sup>23</sup> This demonstrates that by enforcing an octahedral geometry, binding acetonitrile lowers the hydride transfer barrier, explaining the observation that small amounts of acetonitrile must be present for CO<sub>2</sub> reduction to progress.<sup>19</sup> Water is not effective in this role, as it does not allow  $\pi$ -backbonding and coordinates weakly (*vide infra*). In fact the analogue of **TS 1** in which water replaces MeCN poses a barrier of 25.7 kcal/mol. Additionally, work by Ramakrishnan *et al.* suggests that in similar pincer systems, a

$\pi$ -acidity in the ligand *vis* to the hydride can aid by driving the formation of the formate ligand downhill in energy.<sup>41</sup>

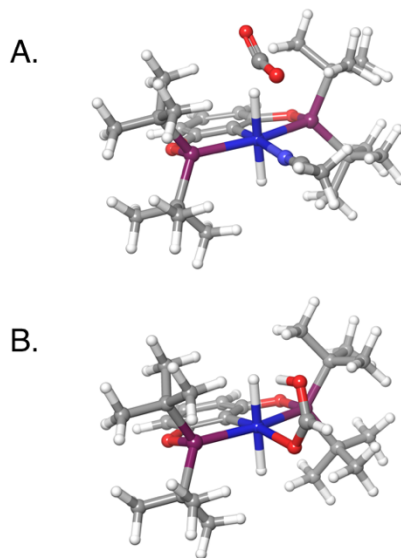


**Figure 3.2:** Transition states for CO<sub>2</sub>RR (A.) and protonation by formic acid (B.).

Following hydride transfer through **TS 1**, a shallow minimum exists, **Mol 2**, in which formate is coordinated through the hydrogen atom. In the mechanism proposed by Cao et al, formate reorients via **TS 2** to coordinate through oxygen, forming intermediate **Mol 3b**. Formate is then released and another solvent molecule coordinates, forming **Mol 4**, which is ready for regeneration. The energy for **TS 2** in iridium is 21.9 kcal/mol, making it difficult to overcome at the experimental temperatures. Instead, formate can simply dissociate, forming **Mol 3**, which is lower in energy than **Mol 3b**, rendering **TS 2** unnecessary. In water, the formate ion can be better solvated, which further favors this pathway as noted by Meyer and coworkers.<sup>19</sup>

The geometries and HOMOs for **Mol 1** can be seen in Figure 3.3. In the iridium compound, the H-Ir-H bond angle is 62° with an H-H distance of 1.62 Å, suggesting the formation of a true dihydride, rather than a dihydrogen adduct. Ir<sup>I</sup> is nucleophilic and able to form strong covalent bonds, which encourage the formation of the dihydride.

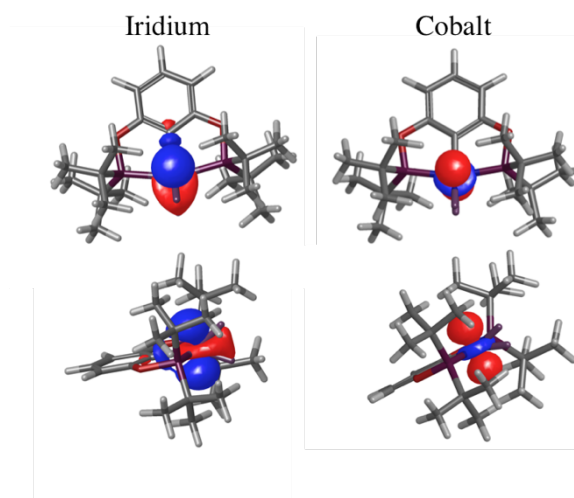
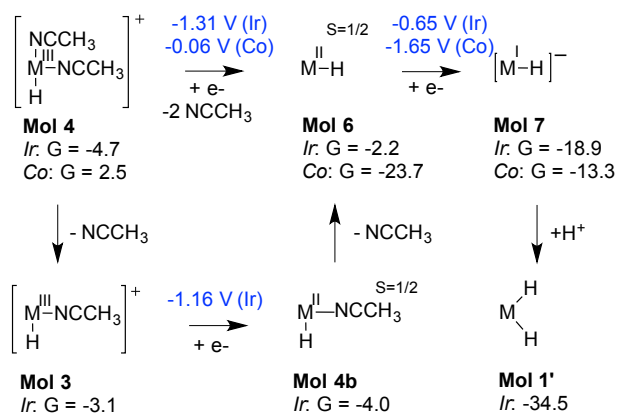


**Figure 3.3:** The HOMO of **Mol 1** for iridium (left) and cobalt (right), showing the preference in iridium for the formation of the dihydride as opposed to the dihydrogen adduct in cobalt.

### *Electrochemical Catalyst Regeneration*

Since all potential paths yield the Ir<sup>III</sup> monohydride exergonically, electrochemical regeneration from **Mol 4** is examined in Scheme 3.2. In the net reduction, the two acetonitrile molecules are released and the metal is reduced by two electrons, forming a metal hydride. In this process, the first reduction of **Mol 4** to **Mol 6** is the potential-determining step, as it has a potential of -1.31 V (free energies are calculated at an applied potential of -1.2 V) and requires solvent loss and a change in geometry. This is in agreement with the irreversible reduction potential of -1.3 V vs NHE, measured experimentally by Brookhart et al. for (POCOP)Ir(H)(NCMe)<sub>2</sub><sup>+</sup> under argon.<sup>19</sup> This process may be aided by initial dissociation of one acetonitrile molecule (**Mol 3**). The doublet iridium hydride has a bent geometry with a C-Ir-H angle of 143°. The HSOMO is a quasi d-π orbital, shown in Figure 3.4. Another electron further reduces the Ir<sup>II</sup> hydride to a square planar anionic singlet **Mol 7** spontaneously at the operating potential of -1.2 V vs NHE. This further aligns with experimental work by Brookhart et al., as the cyclic voltammetry data obtained for this catalyst indicate an irreversible two electron reduction.<sup>18,19</sup> Finally, exergonic protonation of the metal and coordination of solvent regenerates the original catalyst. This mechanism is in contrast to that of Cao et al., which features a concerted two electron reduction of **Mol 4** to make a compound with a bent acetonitrile ligand.<sup>21</sup> In this case, the acetonitrile has been reduced, rather than the metal center. Examination of this reaction can be seen in Appendix

A.1. The Ir<sup>I</sup> product of reduction (**Mol 7**) is 39.0 kcal/mol more stable than Ir<sup>III</sup> coordinated by a reduced acetonitrile ligand.



**Scheme 3.2:** Proposed regeneration of the catalyst occurs as solvent dissociates and the metal is reduced. Free energies (kcal/mol) and potentials (V vs NHE, blue) are reported.

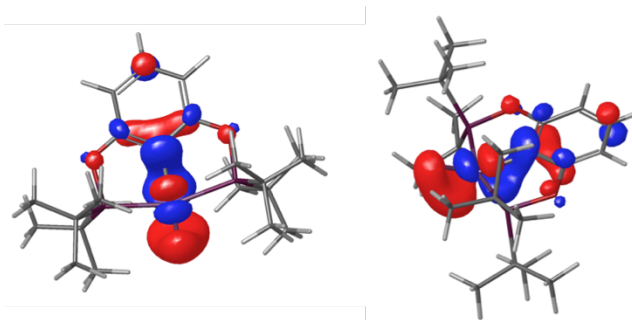
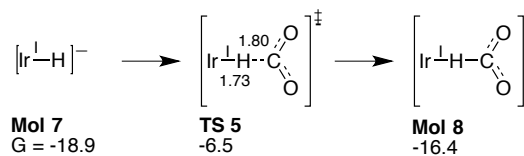


**Figure 3.4:** The HSOMO of the Ir<sup>II</sup> hydride complex (**Mol 7**) shows the bent geometry and quasi d- $\pi$  orbital.

The ability of the iridium hydride anion, **Mol 7**, to reduce CO<sub>2</sub> was also evaluated (Scheme 3.3). In **TS 5**, the CO<sub>2</sub> molecule abstracts the hydride, resulting in coordinated formate, similar to **TS 1**. The hydride abstraction transition state was found to have an energy of -6.5 kcal/mol, or a barrier of 12.4 kcal/mol from the immediately preceding intermediate, slightly lower than that of **TS 1**. We attempted to find a transition state analogous to **TS 4**, but oxygen does not coordinate to the axial positions in this case. The HOMO and HOMO-1 of the molecule (Appendix A.2) explain this behavior, as the oxygen atoms in CO<sub>2</sub> are repelled by the high electron density in the axial positions. This transition state being fully accessible raises the possibility of a secondary catalytic cycle that involves hydride transfer from Ir<sup>I</sup> followed by



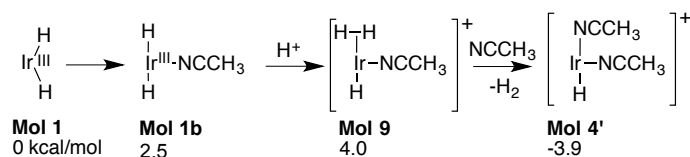
protonation to generate the Ir<sup>III</sup> monohydride **Mol 4**, as recently discussed by Osadchuk et al.<sup>23</sup> A secondary cycle has been reported for (PCNCP)IrH<sub>3</sub> systems, where both the trihydride and dihydride Ir<sup>III</sup> complexes are capable of CO<sub>2</sub>RR.<sup>42</sup> Additionally, the Ir<sup>I</sup> hydride, as well as the ground state, could also be a precursor to hydrogen evolution. To explore potential hydrogen evolution reactions and CO<sub>2</sub>RR from the Ir<sup>I</sup> hydride, a look into the kinetics of proton transfer reactions is necessary.



**Scheme 3.3:** Reaction of the iridium hydride anion with CO<sub>2</sub> is thermodynamically feasible, but is competitive with protonation. Free energies are reported in kcal/mol.

## Hydrogen Evolution

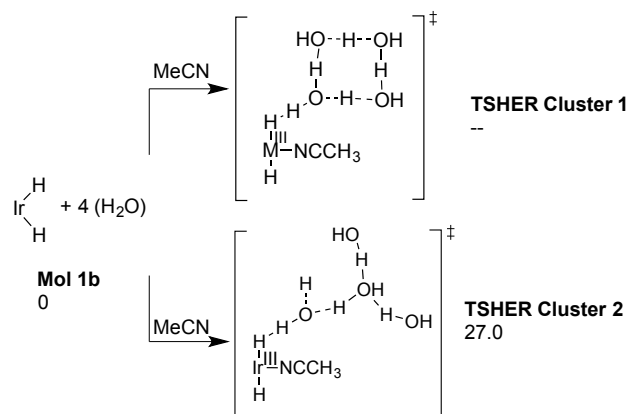
It is remarkable that this catalyst is selective for formate generation over hydrogen evolution in water, even though both Ir<sup>III</sup> dihydride and Ir<sup>I</sup> hydride are intermediates from which an HER mechanism could branch. In the case of the Ir<sup>III</sup> dihydride complex, looking only at the thermodynamics of intermediates (Scheme 3.4), it would appear that hydrogen evolution is feasible, as all energies are thermally accessible. This implies that the impediment to hydrogen evolution is the reactivity of metal hydrides, not their formation, as has been found in other systems.<sup>43</sup> In work by Kang et al., it was suggested that the preference for dihydride (over dihydrogen adduct) was the source of this selectivity.<sup>20</sup>



**Scheme 3.4:** Free energies illustrating the thermodynamic, but not kinetic, feasibility of hydrogen evolution.

If HER is not thermodynamically prohibited, it may be limited by kinetics. In order to explore kinetics, potential routes for hydrogen evolution are considered in Schemes 3.5-3.7. Scheme 3.5

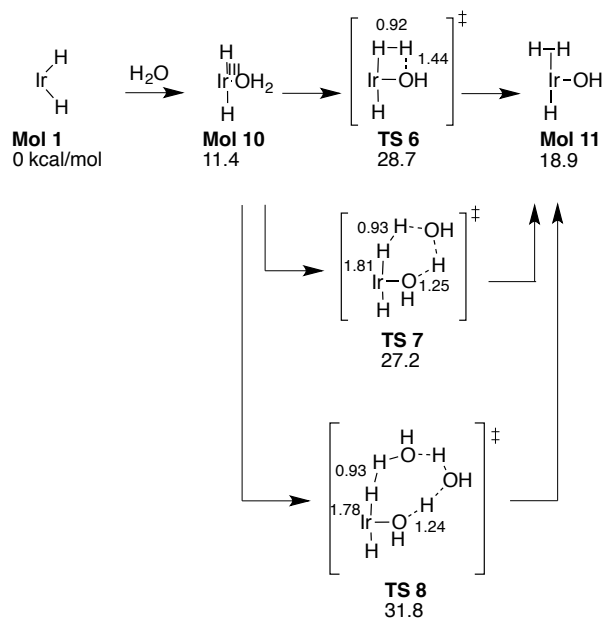
shows protonation of the hydride by an external water cluster, which then proceeds to **Mol 9**, the dihydrogen complex. The shapes of the water clusters were chosen to maximize solvation of the water donating a proton. The two geometries included a square water cluster, (Cluster 1), and a Y-shaped cluster (Cluster 2.) Multi-water clusters have been used in CO<sub>2</sub> reduction and other organometallic studies<sup>44,45</sup>, and we find the cluster, combined with implicit solvation, accurately reproduces the pKa's of water (Appendix A.3). The water cluster was present for both the ground state and the transition states, ensuring that when comparing barrier heights, the energy of forming the water cluster does not affect the results. In this reaction, Cluster 1 is unstable and quickly relaxes to Cluster 2. This may be due to the steric effect of the t-butyl groups. The activation energy of 27.0 kcal/mol for Cluster 2 is much higher than the competing CO<sub>2</sub>RR pathway (**TS 1**). While **Mol 9** appears to be thermodynamically accessible, the path through external protonation by weak acids is not.



**Scheme 3.5:** Free energies of protonation of the dihydride by different water cluster geometries

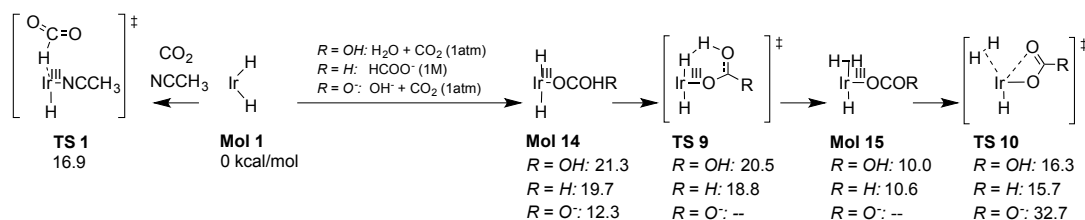
In Scheme 3.6, the intramolecular reaction between coordinated water and hydride can be seen. The complex **Mol 1** first undergoes coordination by water to form **Mol 10**. This is unfavorable, especially relative to coordination by acetonitrile: the t-butyl groups create a hydrophobic pocket, and the lack of  $\pi$ -acidity in water removes back bonding between water and the metal. The Ir-OH<sub>2</sub> distance in **Mol 15** (2.33 Å) is much longer than the Ir-N distance in **Mol 1** (2.11 Å). The preference for acetonitrile is also seen experimentally.<sup>20</sup> Coordinated water then transfers a proton to the hydride. Three configurations for this have been considered, each with increasing number of bridging water molecules to relieve strain. Note that the competing activation barrier

for reacting with CO<sub>2</sub>, **TS 1**, is 16.9 kcal/mol. In the case without bridging waters, **TS 6**, the barrier is 28.7 kcal/mol, which is too high to be competitive with CO<sub>2</sub> reduction. Adding one bridging water (**TS 7**) lowers the calculated barrier to 27.2 kcal/mol, while adding a second bridging water (**TS 8**) increases the barrier. This signifies that adding water molecules does not significantly decrease the calculated barrier. This route also does not appear to be possible.



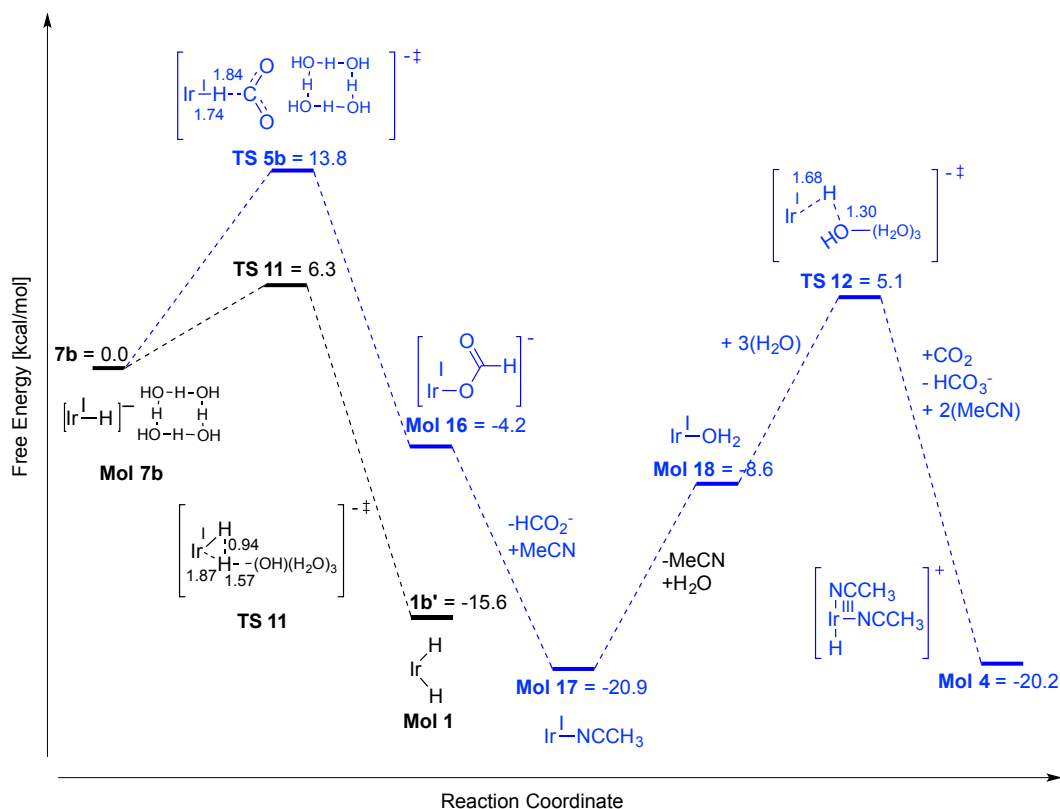
**Scheme 3.6:** Intramolecular protonation of the dihydride. Bridging waters lower the barrier, but this path is not competitive with CO<sub>2</sub> reduction. Free energies are reported.

It is worth noting the entropies of activation for **Mol 1b** + CO<sub>2</sub> (0.035M) → **TS 1** for CO<sub>2</sub> reduction and **Mol 1b** → **TSHER Cluster 2** for internal protonation leading to HER are -20.3 cal/mol·K (using the calculated  $\Delta S_{\text{vib}}^{\ddagger}$ ,  $\Delta S_{\text{CO}_2}(1\text{atm} \rightarrow 1\text{M, aq}) = -23.0 \text{ cal/mol}\cdot\text{K}^{46}$  and 0.035 M for the concentration of CO<sub>2</sub> in water<sup>47</sup>) and -4.5 cal/mol·K, respectively. Selectivity towards CO<sub>2</sub> reduction therefore benefits from the low temperature of the reaction.



**Scheme 3.7:** Free energies for potential pathways for the formation of hydrogen involving carbonic acid, formic acid, and bicarbonate in water, pH = 7

In addition to water, other proton sources generated in reaction conditions could be involved in HER. Formic acid, bicarbonate, or carbonic acid formed *in situ*, with  $pK_A$ 's nearer the reaction conditions than  $H_3O^+$  or  $H_2O$ , could catalyze HER. In order to explore these possibilities, the paths for proton transfer from these three species are compared in Scheme 3.7. First, the proton source coordinates to form **Mol 14**. It is important that for all species, as with water, this is unfavorable. From **Mol 14**, a proton is then transferred from the bound acid to the hydride (**TS 9**), forming a dihydrogen adduct (**Mol 15**).<sup>48</sup> Dihydrogen dissociates and is replaced by the chelating carboxylate in **TS 10**. In the case of bicarbonate, no stable hydrogen adduct could be located, suggesting that the proton transfer and dihydrogen release are one concerted reaction. The barriers for HER are higher in free energy than hydride transfer to  $CO_2$  in water (16.9 kcal/mol), although the activation barriers *following* coordination of the acid are very low. However, in equilibrium with one atmosphere  $CO_2$  and at the turnover numbers reported, these species would be present in concentrations  $\leq 0.1M$ . This highlights the importance of reaction conditions on product selectivity, as it appears that as more carboxylates accumulate, these reactions may become competitive with  $CO_2RR$ .



**Scheme 3.8:** Competing regeneration and CO<sub>2</sub>RR routes from the Ir<sup>I</sup> hydride anion with the preferred pathway in black. Free energies are reported.

The Ir<sup>I</sup> hydride anion **Mol 7** is another potential precursor for both hydrogen evolution and CO<sub>2</sub> reduction.<sup>23</sup> From this intermediate, protonation could lead to formation of a dihydrogen adduct and with the simultaneous coordination of solvent, H<sub>2</sub> can be liberated. However, both from experiment and calculations it can be concluded that this does not occur. Rather than making an H<sub>2</sub> adduct, protonation could also yield the Ir<sup>III</sup> dihydride **Mol 1**, completing the catalytic cycle. On the other hand, the Ir<sup>I</sup> hydride could reduce CO<sub>2</sub>, beginning an alternative cycle. In Scheme 3.8, these paths are compared. The thermodynamic reference state is **Mol 7** (for intermediates) or **Mol 7b**, which is **Mol 7** with a four-water cluster present (for transition states that include a four-H<sub>2</sub>O cluster).

The lowest barrier found for protonating the monohydride is via **TS 11**, with a 6.3 kcal/mol activation barrier for proton transfer with respect to **Mol 7b** in water. The geometry of **TS 11** is interesting, as the incoming proton appears to bond simultaneously with the hydride and the

metal. Bond lengths from the proton to the hydride and the proton to the metal are 0.94 Å and 1.87 Å, respectively. For reference, in **Mol 7b**, the Ir hydride bond length is 1.71 Å. This suggests a late transition state that leads to protonation of the metal and regeneration of **Mol 1**. No dihydrogen adduct was located. That **TS 11** leads to the dihydride was confirmed by intrinsic reaction coordinate (IRC) calculations. Figures along this pathway can be seen in Appendix A.6. The equilibrium between dihydride and dihydrogen has been seen in other organometallic compounds<sup>49-51</sup>, with certain Fe compounds similarly preferring dihydride formation<sup>52</sup>. A transition state utilizing the Y-shaped cluster can be seen in the Appendix A.5 of the Supporting Information, with a higher barrier of 12.8 kcal/mol. An additional structure with a higher energy of 14.0 kcal/mol was reported by Osadchuk et al. in which the Ir atom is directly protonated at the axial position.<sup>23</sup> We could not identify a saddle point on the potential energy surface (in vacuum or including continuum solvation) with this geometry. The lower barrier of the hydridic protonation path **TS 11** is in agreement with other inorganic<sup>51</sup>, biological,<sup>53,54</sup> and heterogeneous<sup>44</sup> examples demonstrating that direct protonation at the metal is often difficult.

The route in blue shows the path in which the Ir<sup>I</sup>-H anion is the active state for CO<sub>2</sub>RR. The initial transition state **TS 5b**, the reduction of CO<sub>2</sub> by the metal hydride, has a higher barrier than protonation in the presence of the cluster, implying that protonation will dominate. Without the water cluster included for consistency in **TS 5b**, the activation energy of **TS 5** is 12.4 kcal/mol. Osadchuk et al. identified several routes by which the Ir<sup>III</sup> complex can be regenerated via protonation by a water cluster. They found feasible barriers from the Ir<sup>I</sup> aquo complex, **Mol 18**. However, we find that coordination of acetonitrile to Ir<sup>I</sup>, neglected in Reference [23], forms the thermodynamic sink **Mol 17**. The formation of **Mol 17** is 12.3 kcal/mol more exergonic than the aquo complex, implying that this would be the ground state of the alternative, Ir<sup>I</sup>-based catalytic cycle. This makes the overall barrier for regeneration via **TS 12** 26.0 kcal/mol, higher than any barrier in the Ir<sup>III</sup>-based cycle. Additionally one would expect to see this complex in the NMR, but only **Mol 4** is reported.<sup>18,19</sup> While this cycle may operate as a side reaction, the low energies of **TS 11** and **Mol 17** lead us to conclude the majority of CO<sub>2</sub>RR in water results from the Ir<sup>III</sup> dihydride, in agreement with the mechanism proposed by Meyer and Brookhart.<sup>18,19</sup> Experimental clarification of this Ir<sup>III</sup>/Ir<sup>I</sup> dilemma raised by DFT calculations will have

important implications for arguments regarding the design of selective CO<sub>2</sub>RR catalysts (*vide infra*).

### Cobalt Analogue

In the interest of using earth-abundant metals, we replaced iridium with cobalt and evaluated the same mechanistic pathway. As shown in Scheme 3.1, cobalt prefers to dissociate solvent to form a cobalt dihydrogen complex (**Mol 1**), unlike iridium. The predicted dihydrogen adduct geometry is shown in Figure 3.3. The H-H bond length in the cobalt complex is 0.86 Å, indicative of a dihydrogen bond. In the iridium complex, the H-H distance is 1.66 Å. This is a consequence of the first row metals forming weaker covalent bonds. The result is that **Mol 1** is the more stable state preceding hydride transfer for the cobalt catalyst. This is problematic as it results in both transition states for hydride transfer to CO<sub>2</sub> (**TS 1** and **TS 4**) being thermally inaccessible.

The regeneration pathway for the cobalt case is also unfavorable. As shown in Scheme 3.2, the cobalt catalyst has the behavior opposite of iridium in that the first reduction to the Co<sup>II</sup> complex, **Mol 6**, is facile, with a potential of -0.06 V vs NHE. However, the second reduction to Co<sup>I</sup> at -1.65 V vs NHE is too negative to be practical. The first reduction to Co<sup>II</sup> involves the loss of two solvent molecules. Previous work has shown that large *t*-butyl groups in the wings of the pincer can sterically destabilize an octahedral complex, encouraging the formation of square planar complexes in iridium pincer complexes.<sup>55</sup> Using a smaller metal like cobalt will enhance this effect, raising the potential for reduction to the square planar cobalt analogue of **Mol 6**. The reduction to Co<sup>I</sup> is more difficult, however, than the analogous reduction to Ir<sup>I</sup>. The C-M and M-H covalent bonds must be made and orthogonalized by hybridizing *s* and *d*<sub>σ</sub> orbitals. This is not favorable for Co for which the 3d orbitals are much smaller than the 4s (in contrast the 5d and 6s orbitals have similar size).<sup>56</sup> These difficulties suggest that (POCOP)Co will not function as a CO<sub>2</sub>RR electrocatalyst.

### Hydricities as a Guiding Design Principle

The hydricities of H<sub>2</sub>, formate and the various hydrides discussed above are useful for illustrating the effect of reaction conditions on reaction thermochemistry. Much work has been done to

measure hydricities of CO<sub>2</sub>RR and HER catalysts in different solvents<sup>16,57,58</sup> and with different coordinating ions and ligand modifications<sup>15,59-63</sup>, to which modeling can add additional understanding. Here we reference driving forces for hydride transfer to the H<sub>2</sub>/H<sup>+</sup> couple, eschewing the poorly-characterized hydride ion commonly used to define hydricities (Figure 3.5). Our calculated driving forces can be converted to the traditional hydricities by adding  $\Delta G$  for H<sub>2</sub>(1atm)  $\rightarrow$  H<sup>-</sup>(1M) + H<sup>+</sup> in the conditions of interest. This value varies among references, but at pH = 0 we adopt 76.6 kcal/mol in acetonitrile<sup>64</sup> and 34.2 kcal/mol in water, recently recommended by Appel et al.<sup>65</sup> In water, we discuss values both at the standard 1M H<sup>+</sup> and at pH=7, representative of the experimental conditions. Solvation of a proton in acetonitrile is calculated using from Tissandier's proton solvation energy in water<sup>66</sup> and adding the free energy of solvent transfer recommended by Pegis et al.<sup>67</sup> The hydricity of formate in acetonitrile is from Dubois et al.<sup>62</sup> and in water was calculated using free energies of formation: HCOO<sup>-</sup>(1M) + H<sup>+</sup>(1M)  $\rightarrow$  CO<sub>2</sub>(1atm) + H<sub>2</sub> (1atm),  $\Delta G = -10.3$  kcal/mol.<sup>46</sup>

The driving force for the iridium dihydride complex in neat acetonitrile is -31.5 kcal/mol. This is insufficient to reduce CO<sub>2</sub>, given the driving force (-33 kcal/mol) of formate in neat acetonitrile. However, in water the formate ion is stabilized<sup>68</sup>, effectively raising its hydricity about 6 kcal/mol above that of **Mol 1**. Operating at pH 7 rather than the standard state of pH 0 further reduces the tendency toward proton reduction. These values can be seen graphically in Figure 3.5, which shows the same narrowing of hydricity ranges shown in other multi-solvent studies.<sup>57,59</sup>



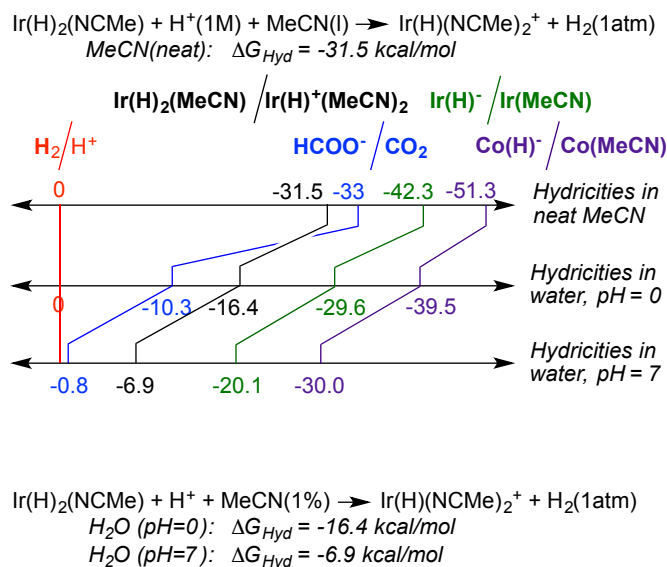


**Figure 3.5:** Thermodynamic cycle used for calculating the hydricity of the iridium dihydride, hydride, and cobalt hydride in neat acetonitrile and water

Calculated solvation energies shed further light on solvent effects. Table 3.1 provides the difference between the solvation energies of hydride donors and their conjugate Lewis acids. Entries 1-3 show that stabilization of the organometallic cations generated by hydride transfer is roughly equal in both solvents. Also, solvation does not drive the coordination of acetonitrile ligands. Kang et al.<sup>19</sup> added a quaternary amine solvation handle to the (POCOP<sup>tBu2</sup>) ligand to facilitate catalysis in water. These complexes, denoted with the superscript “quat”, can be seen in Appendix A.4. Generation of the dicationic **Mol4**<sup>quat</sup> is stabilized by solvation more so than monocationic **Mol4**, but again the effect is similar in both solvents.

**Table 3.1:** Contribution of solvation free energy (kcal/mol) to hydride transfer reactions.

I / J	$\Delta G_{\text{solv},J} - \Delta G_{\text{solv},I}, \text{MeCN}$	$\Delta G_{\text{solv},J} - \Delta G_{\text{solv},I}, \text{Water}$
(Mol 1b + MeCN) / Mol 4	-25.0	-25.6
Mol 1b / Mol 3	-23.0	-27.7
(Mol1 + 2MeCN) / Mol4	-28.9	-26.3
(Mol1b <sup>quat</sup> + MeCN) / Mol4 <sup>quat</sup>	-68.1	-67.7
Mol1b <sup>quat</sup> / Mol3 <sup>quat</sup>	-69.5	-68.4
CH <sub>3</sub> COO <sup>-</sup> / CO <sub>2</sub> (1 atm)	58.8 <sup>a</sup>	77.6 <sup>a</sup>
HCOO <sup>-</sup> / CO <sub>2</sub> (1 atm)	64.2	77.7

<sup>a</sup>Reference 71

Empirical solvation energies for formate in both solvents were not found, so computed values were used and solvation energies of acetate were used for qualitative comparison. The effect of the solvent on hydricities is clearly not due to solvation of the Ir complexes, but to changes in solvation of formate. By comparison, the empirical solvation energies of a similar ion, acetate, in acetonitrile and water differ by 18.8 kcal/mol.<sup>69</sup> This implies that while the coordinating solvent can decrease the hydricity, the stronger hydride donating force comes largely from the stabilization of the formate ion in water versus acetonitrile rather than a solvation effect on the metal complex. Thus, the presence of water will drive formate production forward through stabilization of the product, as noted by Meyer et al.<sup>18</sup>

Two hydricity-based strategies may be proposed for rational design of formate-selective catalysts. One is to overshoot the hydricity of the  $\text{CO}_2/\text{HCO}_2^-$  couple to accelerate  $\text{CO}_2\text{RR}$ . This approach is illustrated by the potential  $\text{Ir}^{\text{I}}$  and  $\text{Co}^{\text{I}}$ -based cycles, as both monohydrides are stronger hydride donors than formate by 20 or 30 kcal/mol in water. In its favor, the  $\text{Ir}^{\text{I}}$  cycle features a low activation barrier for hydride transfer to  $\text{CO}_2$ , the same moderate overpotential as the  $\text{Ir}^{\text{III}}$  cycle, and no competing route to hydrogen evolution. The motif that allows this cycle to avoid HER is the basic lone-pair of  $\text{Ir}^{\text{I}}$ , since protonating this lone pair to generate the dihydride is favorable relative to making a H-H bond. While effective, this motif is generally correlated to (a) a lower reduction potential earlier in the catalytic cycle and (b) a stronger covalent contribution to M-H bonding, and therefore loosely correlated to the abundance of the metal. The iridium metal center is reducing enough to break the putative dihydrogen adduct into the dihydride, and still deliver  $\text{H}^-$  from  $\text{Ir}^{\text{III}}$  to  $\text{CO}_2$ . The  $\text{Co}^{\text{I}}$  analogue supports this interpretation. The reactive hydride shows a strong driving force for reacting with neutral water but is not basic enough to break the H-H bond. Thus, the dihydrogen adduct easily forms and hydrogen evolution is predicted. Creutz et al. measured the rates with which ruthenium hydrides reacted with hydronium and  $\text{CO}_2$  in water.<sup>45</sup> The decreased hydricity of  $(\text{tpy})(\text{bpy})\text{RuH}^+$  relative to  $(\text{C}_6\text{Me}_6)(\text{bpy})\text{RuH}^+$  by 9 kcal/mol led to an acceleration of both reactions approximately a thousandfold, supporting no hope for accelerating  $\text{CO}_2$  reduction *relative* to HER.

A second strategy is to design the catalyst and conditions to be in a range just hydridic enough to reduce  $\text{CO}_2$ , while minimizing the rate of hydrogen evolution.<sup>8,17</sup> The weaker hydricity of the  $\text{Ir}^{\text{III}}$  dihydride puts it in this range. Additionally, the basic metal center ensures the breakup of

any potential dihydrogen adduct. The activation parameters computed for hydride transfer from the Ir<sup>I</sup> hydride (**Mol 7**) and the Ir<sup>III</sup> dihydride (**Mol 1**) support this strategy. Although the Ir<sup>I</sup> hydride offers 13 kcal/mol more driving force to this reaction, the activation free energy is only 3 kcal/mol lower. The activation *enthalpies* (7.8 kcal/mol for Ir<sup>I</sup>, 8.4 for Ir<sup>III</sup>, calculated from aqueous CO<sub>2</sub>) are almost equal. The reaction with Ir<sup>I</sup> has an earlier transition state. As a guiding principal, choosing the most hydridic catalyst does not ensure selective CO<sub>2</sub>RR. The same view has been reached by Taheri and Berben by studying the behavior of [HFe<sub>4</sub>N(CO)<sub>12</sub>]<sup>-</sup> and [HFe<sub>4</sub>C(CO)<sub>12</sub>]<sup>2-</sup>. The carbide provides more driving force for hydride transfer and reduces only protons in the presence of CO<sub>2</sub>, while the nitride with a moderate hydricity of 15 in water catalyzes CO<sub>2</sub> reduction selectively.<sup>17</sup>

Hydricity calculations alone predict the Ir<sup>III</sup> dihydride to be competent for hydrogen evolution, though we have shown that the kinetics of the system slow HER relative to CO<sub>2</sub>RR in a variety of ways. Just as HER kinetics are not fixed by  $\Delta G_{\text{H}}$ , so CO<sub>2</sub>RR kinetics may not be either. As hydricities are purely thermodynamic quantities, they may not capture subtleties in the system such as hydrogen bonding, steric crowding, or hydrophobic pockets which may affect a transition state barrier. The hydricity of the Ir<sup>III</sup> dihydride can be compared to other complexes with measured hydricities, as shown in Appendix A.7. Dubois and coworkers<sup>15,60</sup> found that plotting the first reduction potential of (P<sub>4</sub>)Ni and Pd complexes against their measured hydricities displayed a linear correlation, with more hydridic complexes also having a more negative first reduction potential. While (POCOP)Ir's hydricity is similar to the more hydridic Ni and Pd complexes, a more negative first reduction potential is required to achieve it. As a 3<sup>rd</sup> row metal, Ir makes a very strong metal-hydride covalent bond and prefers not to undergo an odd-electron reduction, making this first reduction more difficult. This implies that more energy is required to achieve the hydricity in (POCOP)Ir compared to the 1<sup>st</sup> and 2<sup>nd</sup> row metals in standard ligand sets and that this behavior may be typical of other 3<sup>rd</sup> row metals.

## Conclusions

(POCOP)Ir presents an interesting case of a selective CO<sub>2</sub>RR catalyst that efficiently produces formate in the presence of water without evolving hydrogen. The iridium-based catalyst is shown through a mechanistic study to have an accessible barrier for CO<sub>2</sub> reduction (via hydride transfer

from a six-coordinate dihydride) and is able to be electrocatalytically regenerated through an Ir<sup>I</sup> hydride intermediate (-1.31 V vs NHE calculated for the one-electron reduction of (POCOP)Ir<sup>III</sup>(H)(MeCN)<sub>2</sub><sup>+</sup>). In the cobalt analogue, both CO<sub>2</sub> reduction ( $\Delta G^\ddagger = 28.9$  kcal/mol) and electrochemical regeneration are prohibited (-1.65 V vs NHE calculated for the one-electron reduction of (POCOP)Co<sup>II</sup>(H)) under mild conditions. (POCOP)Co also prefers the formation of a dihydrogen adduct, in contrast to Ir, which prefers the formation of the dihydride.

Hydrogen evolution via protonation of Ir<sup>III</sup> and Ir<sup>I</sup> hydrides by water, is prohibited by high activation barriers (in excess of 25 kcal/mol). HER barriers within 2 kcal/mol of the CO<sub>2</sub>RR barrier are predicted if catalyzed by molar concentrations of carboxylates. A number of factors cooperate to promote selectivity for CO<sub>2</sub> reduction over the thermodynamically favored reduction of protons. Generically, the neutral-pH, aqueous solvent minimizes the disparity between the driving forces for two-electron reductions of protons and CO<sub>2</sub>.  $\text{H}_2(\text{g}) + \text{CO}_2(\text{g}) \rightarrow \text{HCO}_2^-(1\text{M}) + \text{H}^+$  is only one kcal/mol uphill in water at pH = 7.<sup>46</sup> Since the entropy of activation for hydride transfer to CO<sub>2</sub> is more negative than that for reduction of water, selectivity also benefits from the mild, ambient temperature of the reaction. The binding of acetonitrile to the (POCOP)IrH<sub>2</sub> species simultaneously *promotes* hydride transfer to CO<sub>2</sub> and *inhibits* intramolecular pathways by which water and carboxylates can catalyze HER. The low concentration of carboxylates, which can act as 2<sup>nd</sup> coordination sphere proton relays, also raises these barriers for HER. In both the transition states for hydride transfer to CO<sub>2</sub> and to uncoordinated water, the iridium-hydride covalent bond is broken and replaced with an H-C or H-H sigma-adduct. However, only the latter reaction requires a strong bond (H-OH) to be broken simultaneously. Significant barriers for proton transfer from weak acids to reduced metals similarly promote selectivity toward the reduction of CO<sub>2</sub> to CO by catalysts whose metals bind CO<sub>2</sub> directly<sup>14,43,70</sup>. The basicity of the Ir<sup>I</sup> center encourages protonation to occur leading to the formation of an additional strong Ir-H bond rather than the evolution of H<sub>2</sub>. Protonolysis of Ir<sup>I</sup>-hydride bonds to generate H<sub>2</sub> is also kinetically unfavorable. These results suggest that a moderate hydricity is key in selective CO<sub>2</sub> reduction to formate.

## References

- (1) Schmeier, T. J.; Dobreiner, G. E.; Crabtree, R. H.; Hazari, N. *J. Am. Chem. Soc.* **2011**, *133*, 9274-9277.
- (2) Kaska, W. C.; Nemeh, S.; Shirazi, A.; Potuznik, S. *Organomet.* **1988**, *7*, 13-15.
- (3) Langer, R.; Diskin-Posner, Y.; Leitun, G.; Shimon, L. J. W.; Ben-David, Y.; Milstein, D. *Angew. Chem. Int. Ed.* **2011**, *50*, 9948-9952.
- (4) Ahlquist, M. S. G. *J. Mol. Cat. A: Chem.* **2010**, *324*, 3-8.
- (5) Jessop, P. G.; Joó, F.; Tai, C.-C. *Coord. Chem. Rev.* **2004**, *248*, 2425-2442.
- (6) Benson, E. E.; Kubiak, C. P.; Sathrum, A. J.; Smieja, J. M. *Chem. Soc. Rev.* **2009**, *38*, 89-99.
- (7) Costentin, C.; Robert, M.; Saveant, J.-M. *Chem. Soc. Rev.* **2013**, *42*, 2423-2436.
- (8) Taheri, A.; Berben, L. A. *Chem. Comm.* **2016**, *52*, 1768-1777.
- (9) Ishida, H.; Tanaka, H.; Tanaka, K.; Tanaka, T. *Chem. Commun.* **1987**, 131-132.
- (10) Bolinger, C. M.; Story, N.; Sullivan, B. P.; Meyer, T. J. *Inorg. Chem.* **1988**, *27*, 4582-4587.
- (11) Froehlich, J. D.; Kubiak, C. P. *Inorg. Chem.* **2012**, *51*, 3932-3934.
- (12) Beley, M.; Collin, J. P.; Ruppert, R.; Sauvage, J. P. *Chem. Commun.* **1984**, 1315-1316.
- (13) Hawecker, J.; Lehn, J. M.; Ziessel, R. *Chem. Commun.* **1984**, 328-330.
- (14) Smieja, J. M.; Sampson, M. D.; Grice, K. A.; Benson, E. E.; Froehlich, J. D.; Kubiak, C. P. *Inorg. Chem.* **2013**, *52*, 2484-2491.
- (15) Dubois, D. L.; Miedaner, A.; Haltiwanger, R. C. *J. Am. Chem. Soc.* **1991**, *113*, 8753-8764.
- (16) Taheri, A.; Thompson, E. J.; Fettingner, J. C.; Berben, L. A. *ACS Catal.* **2015**, *5*, 7140-7151.
- (17) Taheri, A.; Berben, L. A. *Inorg. Chem.* **2016**, *55*, 378-385.
- (18) Kang, P.; Cheng, C.; Chen, Z.; Schauer, C. K.; Meyer, T. J.; Brookhart, M. J. *J. Am. Chem. Soc.* **2012**, *134*, 5500-5503.
- (19) Kang, P.; Meyer, T. J.; Brookhart, M. *Chem. Sci.* **2013**, *4*, 3497-3502.
- (20) Kang, P.; Chen, Z.; Brookhart, M.; Meyer, T. *Top. Catal.* **2014**, *58*, 30-45.
- (21) Cao, L.; Sun, C.; Sun, N.; Meng, L.; Chen, D. *Dalton Trans.* **2013**, *42*, 5755-5763.
- (22) Bernskoetter, W. H.; Hazari, N. *Eur. J. Inorg. Chem.* **2013**, 4032-4041.
- (23) Osadchuk, I.; Tamm, T.; Ahlquist, M. S. G. *ACS Catal.* **2016**, 3834-3839.
- (24) Hebden, T. J.; St. John, A. J.; Gusev, D. G.; Kaminsky, W.; Goldberg, K. I.; Heinekey, D. M. *Angew. Chem. Int. Ed.* **2011**, *50*, 1873-1876.
- (25) Becke, A. D. *J. Chem. Phys.* **1993**, *98*, 5648-5652.
- (26) Lee, C. T.; Yang, W. T.; Parr, R. G. *Phys. Rev. B* **1988**, *37*, 785-789.
- (27) Hay, P. J.; Wadt, W. R. *J. Chem. Phys.* **1985**, *82*, 299-310.
- (28) Francl, M. M.; Pietro, W. J.; Hehre, W. J.; Binkley, J. S.; Gordon, M. S.; Defrees, D. J.; Pople, J. A. *J. Chem. Phys.* **1982**, *77*, 3654-3665.
- (29) Hehre, W. J.; Ditchfie.R; Pople, J. A. *J. Chem. Phys.* **1972**, *56*, 2257-2261.
- (30) Zhao, Y.; Truhlar, D. G. *Theor. Chem. Acc.* **2008**, *120*, 215-241.
- (31) Martin, J. M. L.; Sundermann, A. *J. Chem. Phys.* **2001**, *114*, 3408-3420.
- (32) Clark, T.; Chandrasekhar, J.; Spitznagel, G. W.; Schleyer, P. V. *J. Comp. Chem.* **1983**, *4*, 294-301.
- (33) Krishnan, R.; Binkley, J. S.; Seeger, R.; Pople, J. A. *J. Chem. Phys.* **1980**, *72*, 650-654.
- (34) Dojcansky, J.; Heinrich, J. *Chem. Zvesti* **1974**, *28*, 157-159.
- (35) Putnam, W. E.; McEachern, D. M. J.; Kilpatrick, J. E. *J. Chem. Phys.* **1965**, *42*, 749-755.
- (36) Kelly, C. P.; Cramer, C. J.; Truhlar, D. G. *J. Phys. Chem. B* **2006**, *110*, 16066-16081.
- (37) Bridgeman, O. C.; Aldrich, E.W., *J. Heat Transfer* **1964**, *86*, 279-286.
- (38) Wertz, D. H. *J. Am. Chem. Soc.* **1980**, *102*, 5316-5322.
- (39) Bochevarov, A. D.; Harder, E.; Hughes, T. F.; Greenwood, J. R.; Braden, D. A.; Philipp, D. M.; Rinaldo, D.; Halls, M. D.; Zhang, J.; Friesner, R. A. *Int. J. Quantum Chem.* **2013**, *113*, 2110-2142.
- (40) While other work has posited that five-coordinate (POCOP)Ir(H)<sub>2</sub> can oscillate between Y-shaped (distorted trigonal bipyramidal) and T-shaped (square pyramidal) depending on solvent conditions (see refs. 40 and 41), the reported geometry is Y-shaped, which was confirmed using large basis set calculations in solvent.
- (41) Ramakrishnan, S.; Waldie, K. M.; Warnke, I.; De Crisci, A. G.; Batista, V. S.; Waymouth, R. M.; Chidsey, C. E. D. *Inorg. Chem.* **2016**, *55*, 1623-1632.
- (42) Osadchuk, I.; Tamm, T.; Ahlquist, M. S. G. *Organometallics* **2015**, *34*, 4932-4940.
- (43) Keith, J. A.; Grice, K. A.; Kubiak, C. P.; Carter, E. A. *J. Am. Chem. Soc.* **2013**, *135*, 15823-15829.
- (44) Huang, Y.; Nielsen, R. J.; Goddard, W. A.; Soriaga, M. P. *J. Am. Chem. Soc.* **2015**, *137*, 6692-6698.

- (45) Creutz, C.; Chou, M. H.; Hou, H.; Muckerman, J. T. *Inorg. Chem.* **2010**, *49*, 9809-9822.
- (46) Wagman, D. D.; Evans, W. H.; Parker, V. B.; Schumm, R. H.; Halow, I. *The NBS tables of chemical thermodynamic properties. Selected values for inorganic and C1 and C2 organic substances in SI units*, National Standard Reference Data System, 1982.
- (47) Morrison, T. J.; Billett, F. J. *Chem Soc.* **1952**, 3819-3822.
- (48) In the case of R = OH, Mol 12 is a shallow minimum on the potential energy surface, but due to the loss of the zero point energy of the OH bond, it is higher in free energy than the subsequent transition state, TS 4. This effectively makes the energy of Mol 12 the barrier in this process.
- (49) Albinati, A.; Bakhmutov, V. I.; Belkova, N. V.; Bianchini, C.; de los Rios, I.; Epstein, L.; Gutsul, E. I.; Marvelli, L.; Peruzzini, M.; Rossi, R.; Shubina, E.; Vorontsov, E. V.; Zanobini, F. *Eur. J. Inorg. Chem.* **2002**, 1530-1539.
- (50) Belkova, N. V.; Collange, E.; Dub, P.; Epstein, L. M.; Lemenovskii, D. A.; Lledos, A.; Maresca, O.; Maseras, F.; Poli, R.; Revin, P. O.; Shubina, E. S.; Vorontsov, E. V. *Chem. Eur. J.* **2005**, *11*, 873-888.
- (51) Besora, M.; Lledos, A.; Maseras, F. *Chem. Soc. Rev.* **2009**, *38*, 957-966.
- (52) Baya, M.; Maresca, O.; Poli, R.; Coppel, Y.; Maseras, F.; Lledos, A.; Belkova, N. V.; Dub, P. A.; Epstein, L. M.; Shubina, E. S. *Inorg. Chem.* **2006**, *45*, 10248-10262.
- (53) Eilers, G.; Schwartz, L.; Stein, M.; Zampella, G.; de Gioia, L.; Ott, S.; Lomoth, R. *Chem. Eur. J.* **2007**, *13*, 7075-7084.
- (54) Carroll, M. E.; Barton, B. E.; Rauchfuss, T. B.; Carroll, P. J. *J. Am. Chem. Soc.* **2012**, *134*, 18843-18852.
- (55) Lokare, K. S.; Nielsen, R. J.; Yousufuddin, M.; Goddard III, W. A.; Periana, R. A. *Dalton Trans.* **2011**, *40*, 9094-9097.
- (56) Ohanessian, G.; Goddard, W. A. *Acc. Chem. Res.* **1990**, *23*, 386-392.
- (57) Tsay, C.; Livesay, B. N.; Ruelas, S.; Yang, J. Y. *J. Am. Chem. Soc.* **2015**, *137*, 14114-14121.
- (58) Creutz, C.; Chou, M. H. *J. Am. Chem. Soc.* **2009**, *131*, 2794-2795.
- (59) Pitman, C. L.; Brereton, K. R.; Miller, A. J. M. *J. Am. Chem. Soc.* **2016**, *138*, 2252-2260.
- (60) Berning, D. E.; Miedaner, A.; Curtis, C. J.; Noll, B. C.; Rakowski DuBois, M. C.; DuBois, D. L. *Organometallics* **2001**, *20*, 1832-1839.
- (61) Ciancanelli, R.; Noll, B. C.; DuBois, D. L.; DuBois, M. R. *J. Am. Chem. Soc.* **2002**, *124*, 2984-2992.
- (62) Price, A. J.; Ciancanelli, R.; Noll, B. C.; Curtis, C. J.; DuBois, D. L.; DuBois, M. R. *Organometallics* **2002**, *21*, 4833-4839.
- (63) Fong, H.; Peters, J. C. *Inorg. Chem.* **2015**, *54*, 5124-5135.
- (64) Wayner, D. D. M.; Parker, V. D. *Acc. Chem. Res.* **1993**, *26*, 287-294.
- (65) Connelly, S. J.; Wiedner, E. S.; Appel, A. M. *Dalton Trans.* **2015**, *44*, 5933-5938.
- (66) Tissandier, M. D.; Cowen, K. A.; Feng, W. Y.; Gundlach, E.; Cohen, M. H.; Earhart, A. D.; Coe, J. V.; Tuttle, T. R. *J. Phys. Chem. A* **1998**, *102*, 7787-7794.
- (67) Pegis, M. L.; Roberts, J. A. S.; Wasylenko, D. J.; Mader, E. A.; Appel, A. M.; Mayer, J. M. *Inorg. Chem.* **2015**, *54*, 11883-11888.
- (68) Matsubara, Y.; Fujita, E.; Doherty, M. D.; Muckerman, J. T.; Creutz, C. J. *J. Am. Chem. Soc.* **2012**, *134*, 15743-15757.
- (69) Marenich, A. V. K., C. P.; Thompson, J. D.; Hawkins, G. D.; Chambers, C. C.; Giesen, D. J.; Winget, P.; Cramer, C. J.; Truhlar, D. G.; Minnesota, U. o., Ed. Minneapolis, MN, 2012.
- (70) Bourrez, M.; Molton, F.; Chardon-Noblat, S.; Deronzier, A. *Angew. Chem. Int. Ed.* **2011**, *50*, 9903-9906.

## Chapter 4

# MODIFICATIONS ON THE (PEXEP) Pincer Platform: THERMODYNAMICS AND KINETICS OF CO<sub>2</sub> REDUCTION AND HYDROGEN EVOLUTION

With contributions from Sean Najmi, Yufeng Huang, David Shaffer, Robert J. Nielsen,  
Jenny Yang, and William A. Goddard III

*Some material adapted from:*

D.W. Shaffer, **S.I. Johnson**, J.W. Ziller, R.J. Nielsen, W.A. Goddard, A.L. Rheingold, J.Y. Yang; Reactivity of a Series of Isostructural Cobalt Pincer Complexes with CO<sub>2</sub>, CO, and H<sup>+</sup>. *Inorganic Chemistry*. 2014. 53 (24) 13031

### Introduction

In the previous chapter, we work towards the goal of using solar power to electrochemically reduce CO<sub>2</sub> (CO<sub>2</sub>RR) to formate or higher order reduction products.<sup>1-3</sup> In this chapter, we continue that work through systematic modification to understand why so few catalysts are able to complete this reaction selectively, as competition by proton reduction leading to the hydrogen evolution reaction (HER) is often present.<sup>4,5</sup> Two notable successful exceptions stand out: (POCOP)Ir ([C<sub>6</sub>H<sub>3</sub>-2,6-[OP(*t*Bu)<sub>2</sub>]<sub>2</sub>]IrH<sub>2</sub>), as made by Meyer and Brookhart<sup>6-9</sup> and the mechanism described in the previous chapter, and [Fe<sub>4</sub>N(CO)<sub>12</sub>]<sup>-</sup>, as made by Berben and coworkers<sup>10</sup>. Both catalysts are able to reduce CO<sub>2</sub> to formate in water without significant competition from HER. In the case of (POCOP)Ir, Faradaic efficiency of 93% is achieved, with the competing HER shown to occur at the electrode rather than the Ir catalyst.<sup>8</sup> Berben sees 96% Faradaic efficiency in [Fe<sub>4</sub>N(CO)<sub>12</sub>]<sup>-</sup> clusters.<sup>10</sup> Despite the selectivity of the parent compound, substitution of the N atom for carbon in the tetrairon clusters exclusively produces H<sub>2</sub>.<sup>11</sup> Our group recently studied the mechanism for CO<sub>2</sub>RR by (POCOP)Ir via density functional theory (DFT) with the goal of understanding its impressive selectivity, showing that hydrogen production was limited by high kinetic barriers for protonation of the Ir dihydride.<sup>12</sup> In both Berben and our studies, hydricity, or the ability of a hydride donor to give up a hydride, was calculated, either experimentally or computationally. When compared to another hydricity, it can indicate the thermodynamic driving force for donation from a hydride donor to a hydride acceptor. The hydricity of a transition metal complex can be obtained through a variety of

methods, though most recent measurements involve use of a thermodynamic cycle.<sup>5</sup> They are also often referenced to the reaction of a proton and a hydride to make H<sub>2</sub>.<sup>13</sup> These measurements are also often made at equilibrium, so little indication of a H<sup>-</sup> transfer rate is made, though occasionally kinetic hydricities have been measured.<sup>14</sup> Hydricities as a design principle have been used previously, both in catalyst design<sup>15-19</sup> and in understanding the effect of experimental conditions.<sup>20-22</sup> In order to donate a hydride to CO<sub>2</sub> to make formate, the hydricity of the compound must be less than 24 kcal/mol, or the hydricity of the CO<sub>2</sub>/HCOO<sup>-</sup> couple. Theoretically, however, no lower bound to this range exists, except that too low a hydricity represents unnecessary energy input into the system. The hydricity of (POCOP)Ir in water was calculated to be 18.6 kcal/mol, (referenced to a  $\Delta G_{\text{water}}(\text{H}^+ + \text{H}^- \rightarrow \text{H}_2) = 34.2$  kcal/mol<sup>13</sup>). Experimentally, the hydricities of the [Fe<sub>4</sub>N(CO)<sub>12</sub>]<sup>-</sup> and [Fe<sub>4</sub>C(CO)<sub>12</sub>]<sup>2-</sup> complexes were calculated to be 15.5 and <15 kcal/mol, respectively.<sup>11</sup> Since the carbon analog catalyst did evolve hydrogen, Berben and coworkers proposed a “formate window”. This window establishes a lower bound to the range of suitable hydricities by suggesting that in complexes with hydricities lower than 15 kcal/mol, selectivity for CO<sub>2</sub>RR over HER would be lost<sup>11</sup> as driving force for HER would be too strong. Previous (POCOP)Ir work appears to support this, as a monohydride anion complex on the path of CO<sub>2</sub>RR has a calculated hydricity of 5.4 kcal/mol and sees faster protonation than CO<sub>2</sub>RR ( $\Delta G_{\text{HER}}^\ddagger = 6.3$  kcal/mol vs  $\Delta G_{\text{CO}_2\text{RR}}^\ddagger = 13.8$  kcal/mol), though hydrogen evolution is limited by isomerization to the Ir dihydride.<sup>12</sup> If indeed a hydricity range for kinetically preferred CO<sub>2</sub>RR exists, this could become a powerful screening tool for both experiment and theory to predict selective CO<sub>2</sub>RR catalysts.

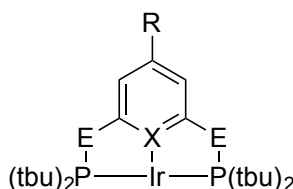


**Figure 4.1:** POCOP-Ir is substituted in the *para* position (R) with -NH<sub>2</sub>, -OH, -Me, -H, and -CF<sub>3</sub>, the arm groups (E) with -CH<sub>2</sub> and -O and the *ipso* position (X) with -C and -N to change the electronic structure of the catalyst.

In order to probe this possibility, the barriers for hydride transfer to CO<sub>2</sub> and protonation of the hydride in a series of modified tridentate pincer (*p*-R-C<sub>5</sub>XH<sub>3</sub>-2,6-[EP(*t*Bu)<sub>2</sub>]<sub>2</sub>) complexes have



been calculated. One strength of using pincers is that their highly modular nature enables them to be methodically altered. In particular, substitution in the *para* position on the phenyl ring can change the electronic structure in the metal center in an isolated manner without significantly changing the steric interactions at the reaction center.<sup>23</sup> Computational studies in both substituted pincers and other complexes have been previously used to investigate a variety of catalytic processes, including hydrogen evolution<sup>24</sup>, hydrogenation<sup>25</sup>, C-H activation<sup>26,27</sup>, and water-splitting<sup>28</sup>. Experimentally, substituted POCOP catalysts have been used to study silane dehydrocoupling<sup>29</sup> and dehydrogenation<sup>26</sup>. The substituted R-POCOP pincer can be seen in Figure 4.1. Various R groups (R = -NH<sub>2</sub>, -OH, -Me, -H, -CF<sub>3</sub>) were chosen to represent a range of Hammett constants ( $\sigma_p$  between -0.66 and 0.54)<sup>30</sup> to probe both electron donating and withdrawing effects. These complexes will be used in particular for the hydricity studies. Calculated hydricities of these compounds can be seen in Table 4.1, where they span the range 21.1 to 15.2 kcal/mol. In addition to kinetic effects, electronic effects on acetonitrile (MeCN) coordination and intermediate energies will be investigated.

For understanding general effects, pincer ligands can also be modified in the *ipso* position (X in Figure 4.1), substituting the phenyl ring for other aromatic (or non-aromatic<sup>31</sup>) rings, as well as the arms (E). Prior work has investigated the use of both (POCOP)Co<sup>12,32</sup> and for use in CO<sub>2</sub>RR, while experimental work has investigated (PONOP)Ir for use in C-H bond cleavage.<sup>33</sup> Here, we will investigate (PENEP)Co (E = CH<sub>2</sub>, O) catalysts, then compare to (PONOP)Ir.

While some of these systems have been made experimentally<sup>29,34,35</sup>, it is important to note that these pincers are primarily toy systems.

## Methods

All geometry optimizations, frequency and solvation calculations were carried out using the B3LYP functional<sup>36</sup> and with a 2- $\zeta$  basis set and the Los Alamos small core potential on iridium and 6-311G\*\* basis set on organics.<sup>37,38</sup> Single point electronic calculations were completed with the M06 functional.<sup>39</sup> The LACVP\*\*++ basis set was used in iridium with augmented *f*-functions and diffuse functions.<sup>40</sup> All organic atoms used the 6-311G\*\*++ basis set.<sup>41</sup> Solvation in water was modeled using the Poisson-Boltzmann polarizable continuum model using a dielectric constant of 80.37 and probe radius of 1.40 Å. In order to calculate the free energy of acetonitrile

in water, the 1 atm ideal gas free energy of MeCN was computed using appropriate statistical mechanical methods and empirical free energies of vaporization (2.45 kcal/mol<sup>42</sup>) was subtracted. Solvation of formate in water was taken from experiment.<sup>43</sup>

In the case of (PENEP)Co catalysts, B3LYP-D3, the dispersion corrected functional was used.<sup>44</sup> Solvation for these complexes in acetonitrile via the Poisson Boltzmann polarizable continuum model used a dielectric constant of 37.5 and a probe radius of 2.19 Å. The free energy of 1 M acetonitrile was computed using the appropriate statistical mechanics formulae, and the empirical free energies of vaporization (1.27 kcal/mol, derived from the vapor pressure<sup>42,45</sup>) was subtracted. The chemical potential of H<sup>+</sup>(1M) in MeCN was the ideal gas free energy ( $H-TS = 5/2 kT - (298K)(26.04 \text{ e.u.})^{46} = -6.3 \text{ kcal/mol}$ ) minus the free energy of hydration ( $\Delta G(1\text{atm} \rightarrow 1\text{M}) = 264.0 \text{ kcal/mol}^{47}$ ) plus the transfer free energy  $\Delta G(1\text{M, aq} \rightarrow 1\text{M, MeCN}) = 5.7 \text{ kcal/mol}^{48}$ ]. The formally “Co<sup>0</sup>” solvent complexes are best described as high spin, cationic Co<sup>I</sup> centers antiferromagnetically coupled to radical anionic pyridine ligands. The approximate projection scheme proposed by Yamaguchi<sup>49</sup> was applied (using the large basis, unsolvated wavefunctions) to correct electronic energies of the unrestricted doublets for spin-contamination from the higher-energy quartet state,  $S^2$  values of the broken-symmetry doublets ranged from 1.50 to 1.65, leading to corrections of up to 3.2 kcal/mol. Wavefunctions for Co<sup>II</sup> and Co<sup>I</sup> states did not suffer spin contamination.

Free energies were calculated by the following equation:

$$G = E_{M06} + G_{solv} + E_{ZPE} + H_{vib} + H_{TR} - T(S_{vib} + S_{elec} + S_{TR})$$

In this equation,  $E_{M06}$ ,  $G_{solv}$ , and  $E_{ZPE}$  are the single point electronic energy, free energy of solvation, and zero-point energy correction, respectively.  $H_{vib}$  and  $H_{TR}$  ( $^{12}/_2 k_B T$ ) are the vibrational and translational/rotational enthalpies respectively, while  $S_{vib}$ ,  $S_{elec}$ , and  $S_{TR}$  represent the vibrational, electronic, and translational/rotational entropies. Gas phase translational and rotational entropies were modified by corrections suggested by Wertz in order to be used in solvent.<sup>50</sup> Transition state calculations were validated by the presence of imaginary modes in analytical frequency calculations. All calculations were carried out in Jaguar.<sup>51</sup>

Hydricities were calculated using the free energy from the following equation:



where L is the modified pincer ligand. In order to calculate the free energy of the proton in solution for hydricity calculations, we are using the value established by Tissandier and coworkers.<sup>47</sup> In the previous chapter<sup>12</sup>, we have referenced hydricities to the  $\text{H}_2/\text{H}^+$  couple, but for the sake of comparison to experimental systems we are referencing hydricities to the free energy of the formation of hydrogen from a proton and a hydride (34.2 kcal/mol in water), in accordance with recommendations set forth by Connelly et al.<sup>13</sup> These are the same values used by Berben and coworkers.<sup>11</sup>

## Results and Discussion

### *Effect of Modification on Pathways and Hydricity*

Low energy pathways for the  $\text{CO}_2\text{RR}$  and protonation of the ground state (H-POCOP)Ir complex have been previously modeled<sup>12</sup> and will serve as the template for mechanistic steps in the modified complexes. Free energy surfaces for three representative compounds ( $\text{X} = \text{NH}_2$ , H, and  $\text{CF}_3$ ) can be seen in Figure 4.2, with all pincer complexes represented in Appendix B in the Supporting Information. The complexes whose pathways are shown in Figure 4.2 were chosen because they are the most electron donating/withdrawing groups according to Hammett constant. The pathway for  $\text{CO}_2\text{RR}$  is shown moving from **Mol 1** (in the center) to the right. MeCN first coordinates to form **Mol 1b**, after which the hydride can be abstracted in **TS 1**. The subsequent formate complex, bound through the hydride, is shown in **Mol 2**. In water, the formate ion can be solvated and thus dissociates to form **Mol 3**. Finally, a second MeCN molecule can coordinate to form the octahedral complex **Mol 4**, which can then undergo a two electron reduction and protonation to regenerate **Mol 1**.<sup>12</sup> In comparing the different ligands, one can see that the more electron donating pincer,  $\text{NH}_2$ -POCOP, disfavors acetonitrile coordination the most, while in the  $\text{CF}_3$ -POCOP pincer, coordination is favorable by 1.2 kcal/mol. This effect will be discussed *vide infra*. **TS 1** is also affected by the electronic effects in the pincer, with the most electron-withdrawing pincer providing the lowest overall barrier at 16.3 kcal/mol, though this is quite close to the barrier for the parent complex (16.9 kcal/mol). Electron donation into the pincer raises the barrier, though likely due to the increased energy required for coordinating MeCN.

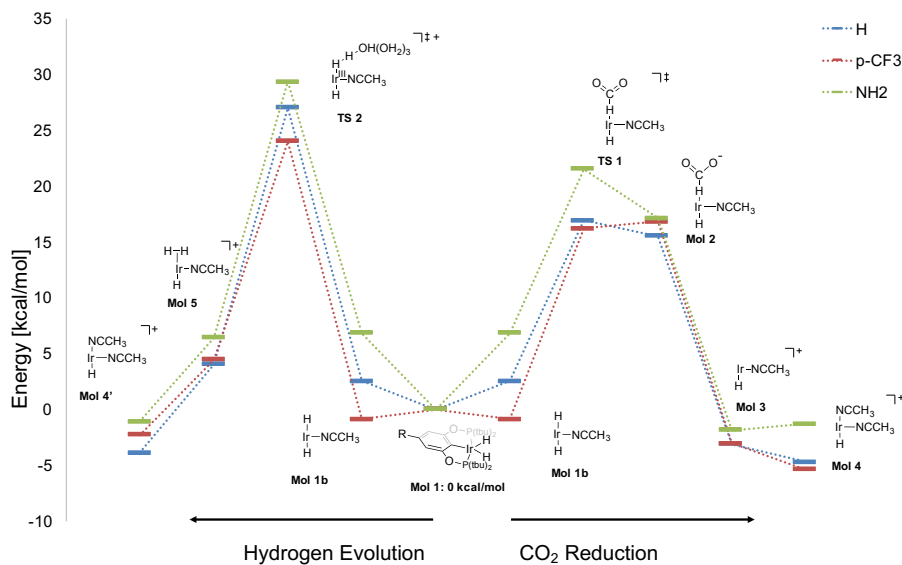


**Figure 4.2:** Pathways for CO<sub>2</sub> reduction and hydrogen adduct formation are shown for three representative pincer complexes (R-POCOP, X = NH<sub>2</sub>, H, CF<sub>3</sub>). Free energies in kcal/mol.

Intermediates along the pathway to protonation by water are also shown in Figure 4.2, moving from **Mol 1** in the center to the left. Again, the first step along this pathway is coordination by MeCN. This is followed by protonation by an external four-water cluster (use of which is previously justified<sup>12,52,53</sup> and is seen in Appendix A.3), represented by **TS 2**. This forms an H<sub>2</sub> adduct, seen in **Mol 5**, which can be released to form the bis-MeCN complex **Mol 4'**. Again, this complex can undergo a two electron reduction and protonation to regenerate **Mol 1**. The lowest barriers again belong to the CF<sub>3</sub>-POCOP analogue, at 22.0 kcal/mol. This is 7.3 kcal/mol lower than the NH<sub>2</sub>-POCOP analogue. The energy of the H<sub>2</sub> complex **Mol 5** is also affected by the *para* substituent group, with the energy of the electron donating pincer complexes having the highest energy. This again may be attributed to the coordination of MeCN in the axial position.

Both pathways are initiated by the coordination of MeCN in the equatorial position to form **Mol 1b**.<sup>12</sup> The free energy of the formation for all *para* substituted analogues of **Mol 1b** plotted versus Hammett constants ( $\sigma$ ) of the substituted functional group is shown in Figure 4.3. Linear correlation between the energy for coordinating MeCN in the equatorial position and the

Hammett constant of the *para* substituted group, shown in Figure 4.3a, implies a strong *trans* influence. The more electron-withdrawing complexes encourage the coordination of MeCN, even driving this energy below zero in the case of CF<sub>3</sub>-POCOP, by reducing competition for the orbital shared by the *ipso* carbon in the pincer and MeCN in the equatorial position. This in turn allows for easier donation by the lone pair of MeCN. This *trans* influence has been noted in other pincer complexes with *para* substitutions<sup>29</sup> and in iridium complexes with the same functional groups sans pincer directly *trans* to the equatorial position.<sup>26</sup> In their work with four and five coordinate complexes with monodentate ligands, Goldman and coworkers showed that little effect is seen unless ligands are directly *trans* to the substituted ligand.<sup>26</sup> However, as the pincer complexes are tridentate, the electronic effect of the *para* substitution may be more widely felt by all octahedral positions. This is significant because the relevant H<sup>-</sup> is in the *cis* position. This is evident in the HOMO diagrams of the CF<sub>3</sub>-POCOP and NH<sub>2</sub>-POCOP analogues of **Mol 1b**, wherein the  $\pi$ -system of the phenyl ring in the pincer mixes into a combination of the d<sub>xy</sub> orbital and s orbitals of the hydrides, as shown in Figure 4.3. The NH<sub>2</sub>-POCOP analogue shows greater extension into the  $\pi$ -system, even extending into the lone pair of the NH<sub>2</sub> group. The CF<sub>3</sub>-POCOP pincer shows greater localization onto the *para* carbon alone.

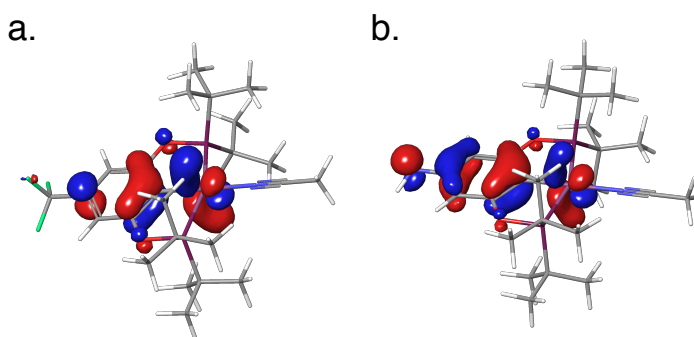


**Figure 4.3:** HOMO orbitals of a. CF<sub>3</sub>-POCOP and b. NH<sub>2</sub>-POCOP dihydride. Both analogues show mixing of the  $\pi$ -system of the phenyl ring with the d<sub>xy</sub> orbitals of the metal.

To separate the geometric effect from the electronic effect of coordinating MeCN, the single point, large basis electronic energy of **Mol 5'** (without the MeCN in the equatorial position, with H<sub>2</sub> *trans* to H<sup>-</sup>) was calculated. This was compared to the electronic energy of **Mol 5**. The results show little change in the energy (< 2 kcal/mol) of the electronic energy for the different substituent groups relative to the energy for coordination, implying that the geometric effect of

moving the H<sub>2</sub> and hydride *trans* to one another is minimal. Additionally, Figure 4.4 also shows the correlation between  $\sigma_m$  Hammett parameters and the free energy of **Mol 1b**. The use of  $\sigma_m$  should remove the effect of  $\pi$  delocalization and resonance and limit the effect to electronegativity effects only. A weaker correlation is seen here, implying that both resonance contributes more strongly and backbonding to the MeCN groups is at play. Backbonding refers to the donation from the d orbitals of the metal back into the p orbitals of the organic ligand, opposite the direction of *sigma* bonding. Backbonding was previously proposed as important in the coordination of acetonitrile<sup>6</sup> and this work supports that. The impact of these *para* substituted groups is important especially since MeCN coordination is a key step in CO<sub>2</sub>RR by (POCOP)Ir.<sup>12</sup>

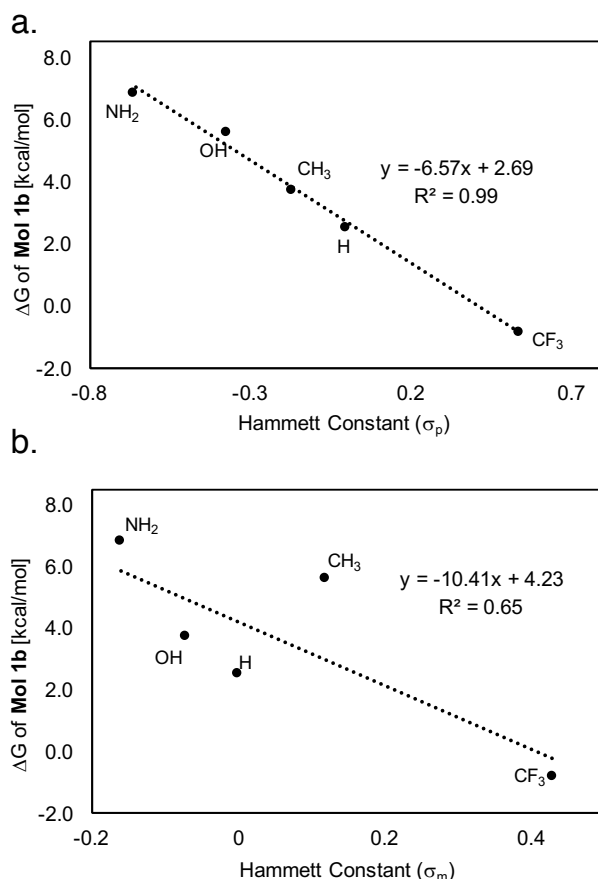


**Figure 4.4:** Free energy for coordination of acetonitrile versus para (a.) and meta (b.) Hammett constants show that more electron withdrawing group favor acetonitrile coordination.

The substitution of the *para* position in the pincer allows a range of hydricities to be achieved, as shown in Table 4.1. These hydricities allow us to span much of the range of hydricities proposed by Berben et al. that make up the “formate window”. One begins by plotting the Hammett constants versus calculated hydricities. This can be seen in Figure 4.5.

**Table 4.1:** Hammett constants and calculated hydricities

Functional Group	Hammett Constant ( $\sigma_p$ )	Hammett Constant ( $\sigma_m$ )	Calc'd Hydricity [kcal/mol]
NH <sub>2</sub>	-0.66	-0.16	17.4
OH	-0.37	0.12	17.3
CH <sub>3</sub>	-0.17	-0.07	15.1
H	0.00	0.00	18.6
CF <sub>3</sub>	0.54	0.43	21.0

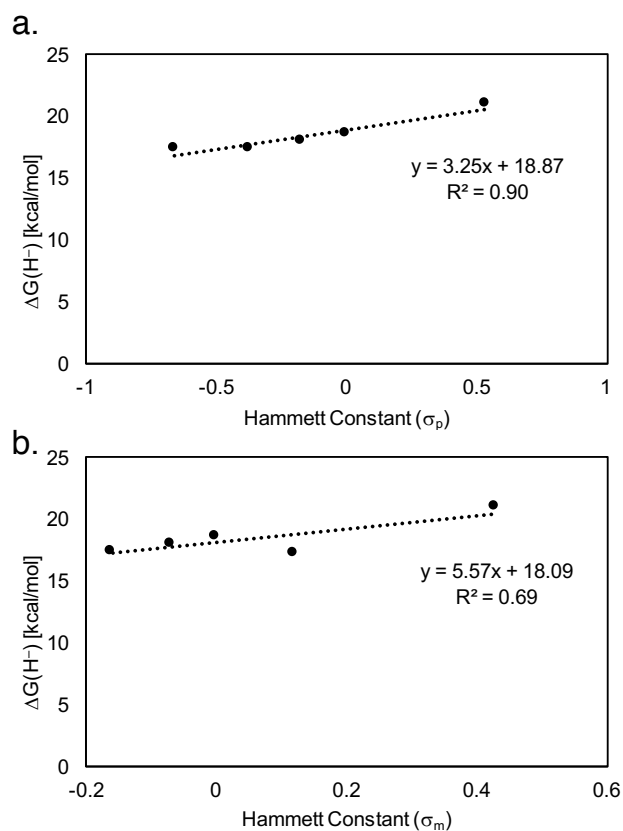


**Figure 4.5:** Calculated hydricity as a function of *para* and *meta* Hammett constants.

One can see good linear correlation between  $\sigma_p$  and hydricity, with the general trend that electron withdrawing groups lead to less hydridic compounds. Better correlation between  $\sigma_p$  and the calculated hydricities than between  $\sigma_m$  and hydricities imply that this is largely a resonance effect, which can be seen in the previously discussed Figure 4.4.

Hydricities can also be compared to the energies of **TS 1** and **TS 2**. This can be seen in Figure 4.6. It is important to note that all hydricities and barriers are calculated from **Mol 1b** for the sake of consistency. Again, calculated scatter is quite large, particularly in the case of **TS 2**, where no clear trend can be seen. This can be attributed to a number of sources, including the extra degrees of freedom involved in protonation from the water cluster. However, even in the relatively simpler reaction with CO<sub>2</sub> (**TS 1**), little correlation is seen.

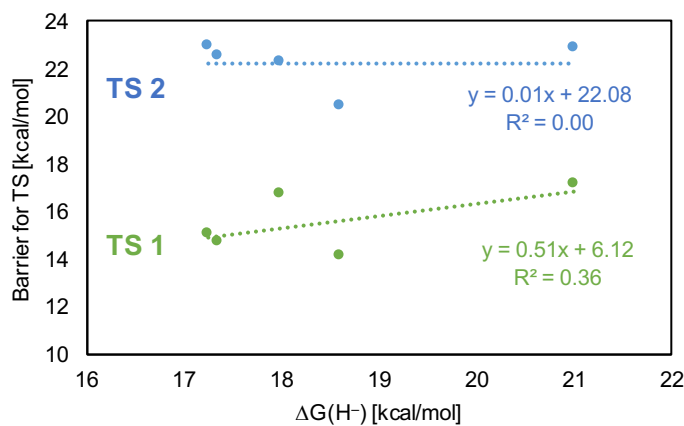


**Figure 4.6:** Transition states for hydride abstraction by CO<sub>2</sub> (**TS 1**, green) and protonation of hydride (**TS 2**, blue) as a function of hydricity.

While electron withdrawal aids in the initial coordination of MeCN, once MeCN is in the equatorial position, transition state barriers are decreased by electron donating groups. Additional electron density at the metal center may help to break the strong Ir-H bond. From **Mol 1b**, the formation of **Mol 4/4'** is also generally more exergonic for the electron donating groups. Just as solvation of formate by solvent can affect the hydricity,<sup>12</sup> the more exergonic formation of **Mol 4** also provides extra thermodynamic driving force to make electron donating group complexes more hydridic. Increasing hydricity (less thermodynamic driving force) corresponds with higher barriers overall, which would be expected from the Bell-Evans-Polanyi principle.<sup>54</sup> However, the fact that protonation, which should have a larger driving force, still has



higher barriers overall across the range of hydricities is puzzlingly not in accord with this principle. Despite modifications meant to make this catalyst more reactive to protons, we still see kinetically unfavorable protonation relative to CO<sub>2</sub> reduction and little indication that the trend is changing.

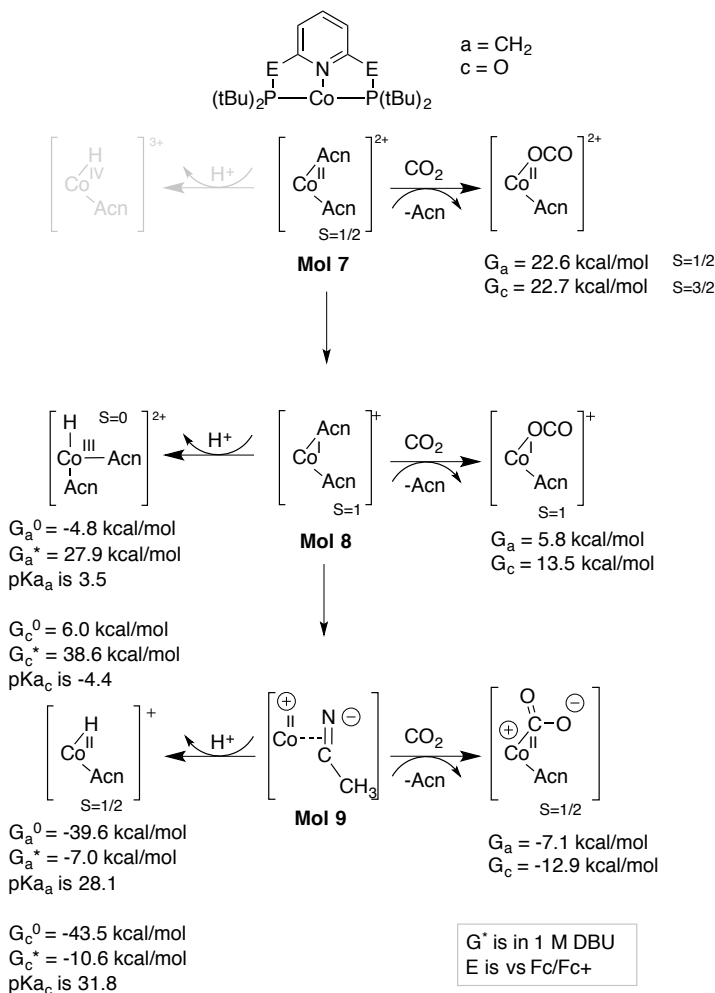
### Modification of the *ipso* position

#### *(PENEP)Co catalysts*

In work done in conjunction with David Shaffer (now of Brookhaven National Lab) and Prof. Jenny Yang of University of California, Irvine, (PENEP)Co (E = CH<sub>2</sub>, O) catalysts were investigated for their use in CO<sub>2</sub>RR (seen in Scheme 4.1).<sup>55</sup> Experimentally, no reaction with the Co<sup>I</sup> analogue of these catalysts were seen. However, upon a second reduction event, the (PCNCP)Co analogue did see reaction with CO<sub>2</sub>, forming what was spectroelectrochemically identified as a CO bond. This CO adduct of (PCNCP)Co was prepared independently as validation of the carbonyl adduct. Protons are necessary for these compounds to reduce CO<sub>2</sub> to CO and H<sub>2</sub>O, which again presents the possibility of competition with HER. Experimentally, the pK<sub>a</sub> of (PCNCP)Co was determined to be between 3 and 6 pK<sub>a</sub> units, but was difficult to pin down due to the complexes' instability. Therefore, computational methods were employed to gauge the relative intermediate energies involved with a CO<sub>2</sub> versus H<sup>+</sup> reduction pathway.

Free energies for the reaction of solvento complexes with CO<sub>2</sub> and protons can be seen in Scheme 4.1. For both PCNCP and PONOP ligands, the Co<sup>I</sup> and Co<sup>II</sup> complexes lowest in free energy contain two acetonitrile molecules. The second solvent molecule is weakly bound, by 2.2 kcal/mol relative to liquid MeCN for the PONOP (**Mol 8**) complex. Crystals of related (PNNNP)Co catalysts contain only one bound acetonitrile. The computed association energies are less than the accuracy of DFT free energies, but it is physically reasonable that the weakly bound solvent was liberated by the (drying procedure) used to isolate the crystals. It is thermodynamically unfavorable for the Co<sup>II</sup> complexes (**Mol 7a** and **Mol 7c**) to react with CO<sub>2</sub>, as in both ligands it is uphill by at least 20 kcal/mol to form the CO<sub>2</sub> complex. CO<sub>2</sub> forms a loosely bound complex at the equatorial position through the oxygen. In the PCNCP ligand, the Co-O bond length is calculated to be 2.10 Å and in PONOP the bond length is 2.12 Å.

It is also unfavorable for  $\text{Co}^{\text{I}}$  (**Mol 8a** and **Mol 8c**) to react with  $\text{CO}_2$ , and only weakly coordinated complexes form, similar to the  $\text{Co}^{\text{II}}$  case. Protonation of  $\text{Co}^{\text{I}}$  by HDBU (DBU = 1,8-diazabicyclo[5.4.0]undec-7-ene) is also highly endergonic. However, protonation to form  $[(\text{PCNCP})\text{Co}^{\text{III}}\text{H}(\text{NCCH}_3)_2]^{+2}$  from **Mol 8a** is accessible with strong acids, giving a calculated  $\text{pK}_a$  close to the value experimentally measured above. However, **Mol 8c** is calculated to be much less basic, and protonation is not accessible in  $\text{CH}_3\text{CN}$ .



**Scheme 4.1:** Calculated  $\text{pK}_a$  values and  $\text{CO}_2$  binding energies for the reduction of  $[(\text{PCNCP})\text{Co}]$  and  $[(\text{POCOP})\text{Co}]$ .

At more negative potentials, the  $\text{Co}^{\text{I}}$  cations can be further reduced, as is seen experimentally. While the calculated reduction potentials do not capture the exact values, they do capture the ligand trend. In both PCNCP and PONOP, two kinds of low-energy, formally  $\text{Co}^0$  structures

were identified (**Mol 9a** and **9c**). When zero, one or two acetonitrile molecules are coordinated to a neutral (PCNCP)Co moiety through nitrogen, the wavefunction consists of a triplet  $\text{Co}^{\text{I}}$  cation antiferromagnetically coupled to a radical anion ligand with spin distributed around the pyridine ring. The PCNCP ligands can thus become ‘redox active’,<sup>56,57</sup> but not under conditions for neutral-pH, low-overpotential  $\text{CO}_2$  reduction. A few kcal/mol lower in free energy, however, lie neutral (PCNCP)Co( $\eta^1$ -C MeCN) complexes incorporating a  $\pi$ -bound solvent molecule. The Mulliken population on bound MeCN ( $-0.75e^-$ ) and C-N and Co-C bond lengths (1.23Å and 1.95Å, respectively) suggest the description of  $\text{Co}^{\text{II}}$  metallacycle. That various isomers lie within 8 kcal/mol of one another underscores how the reduced metal can change coordination at the metal center.

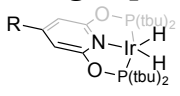
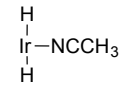
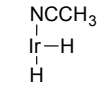
These neutral complexes can react with  $\text{CO}_2$ , as it is exergonic by 7.1 kcal/mol in PCNCP and 12.9 kcal/mol in PONOP to do so. This mirrors the experimental findings of this paper, which indicate that reactions with  $\text{CO}_2$  occur after the second reduction. With the extra electron density provided by the second reduction, the lone pair from Co is donated into the  $\pi^*$  orbital of the  $\text{CO}_2$ , bending the  $\text{CO}_2$  adduct. This is similar to the bonding which occurs with the bent MeCN adduct. The competing reaction with protons is also favorable. At pH = 24.3, reacting with protons is exergonic by 7.0 kcal/mol in PCNCP and 10.6 in PONOP.

#### (PONOP)Ir

While no reaction except at very negative potentials with (PONOP) $\text{Co}^{\text{I}}$  is seen, it may still be possible for reaction with (PONOP)Ir<sup>III</sup> dihydride. Previously, Brookhart and coworkers saw evidence of C-H bond cleavage in reactions with benzene.<sup>33</sup> Thus, the reaction of  $\text{CO}_2$  with (R-PONOP)Ir was investigated using the same mechanism as previously seen for (POCOP)Ir<sup>12</sup>, where X =  $\text{NH}_2$ ,  $\text{CH}_3$ , H, and  $\text{CF}_3$ . First, the coordination of MeCN to form **Mol 1b** was investigated, as shown in Table 4.2. While in POCOP the *trans* conformation was preferred<sup>12</sup>, this was not the case in all variations of the R-PONOP ligand. Instead, the *cis* conformation was preferred by as much as ~10 kcal/mol in the most electron-donating case of X =  $\text{NH}_2$  and ~8 kcal/mol in the most electron-withdrawing case of X =  $\text{CF}_3$ .  $\text{CO}_2\text{RR}$  was investigated from the *cis* conformation, but no stable formato complex could be found from either the axial or equatorial hydride, unlike in the POCOP analogues. When the hydricities of these complexes

are compared, it is easy to see why. The *cis* isomer has acetonitrile and pyridine groups *trans* to each hydride. Neither is as good a donor as the hydride or the phenyl ring<sup>26</sup> thus the characteristically strong iridium hydride bond cannot be broken. This is reflected in the hydricity, which is 8.6-13.4 kcal/mol too weak to donate to the CO<sub>2</sub>/HCOO<sup>-</sup> couple. These catalysts would not be effective in this manner for CO<sub>2</sub> reduction. It is important to note that another CO<sub>2</sub>RR pathway may exist, but that in the case of the dihydride in the presence of acetonitrile, coordination would likely result in the best case, a thermodynamic sink, and in the worst case, hydrogen evolution. In a computational study with a (PCNCP)Ir catalyst, hydrogenation was achievable in both in the case of a trihydride and in the case of a coordinating hydroxyl group in the equatorial position.<sup>58</sup> This further underlines the importance of a strong *trans* donor in weakening the iridium hydride, as the trihydride is necessary to ensure weakening of the Ir-H bond.

**Table 4.2:** Free energies for coordination of MeCN to (R-PONOP)Ir complexes.

 R group	$\Delta G_{\text{trans}}$ [kcal/mol]	$\Delta G_{\text{cis}}$ [kcal/mol]	Hydricity [kcal/mol]
			
NH <sub>2</sub>	7.2	-3.3	32.6
CH <sub>3</sub>	5.6	-1.3	32.6
H	5.0	-3.4	34.1
CF <sub>3</sub>	8.2	0.1	37.4

## Conclusions

In this study, we investigated the role of modifications on the pincer ligand, both for understanding the relationship between hydricity and kinetics, and general catalytic mechanisms, in (PEXEP)Ir and Co catalysts. Overall, the best candidates for low or accessible barriers involved those with more electron donation to the metal center, as this was important for weakening the Ir-H bond sufficiently for reaction. That being said, electron withdrawal was important in (R-POCOP)Ir catalysts as it allowed for coordination of MeCN. In the case of the dihydride, a strong *trans* influence on the relevant hydride is key in CO<sub>2</sub> reduction from Ir

catalysts, as it further weakens the Ir-H bond, allowing for hydride abstraction. In the case of PENEPC catalysts, neither metal centers are able to complete electrocatalytic CO<sub>2</sub>RR without going to very negative potentials, or forming a trihydride, further underlining the importance of electron donation and *trans* effect. Future work in this area involves expanding the data set investigating the relationship between hydricity and barrier height. I propose using several different *para* substituents, particularly in towards the direction of electron donating groups (BH<sub>2</sub>, NMe<sub>2</sub>). This will expand the range of hydricities achieved, hopefully moving out of the formate window. Additionally, simpler transition states such as the bridging water states in Chapter 2 may also remove some of the noise in the transition state data, giving a cleaner picture of the link between hydricity and barrier height.

## References

- (1) Gray, H. B. *Nat. Chem.* **2009**, *1*, 7-7.
- (2) Lewis, N. S.; Nocera, D. G. *Proc. Natl. Acad. Sci. USA* **2006**, *103*, 15729-15735.
- (3) Aresta, M. *Carbon Dioxide Reduction and Uses as a Chemical Feedstock*; Wiley-VCH: Weinheim, Germany, 2006.
- (4) Taheri, A.; Berben, L. A. *Chem. Comm.* **2016**, *52*, 1768-1777.
- (5) Wiedner, E. S.; Chambers, M. B.; Pitman, C. L.; Bullock, R. M.; Miller, A. J. M.; Appel, A. M. *Chem. Rev.* **2016**, *116*, 8655-8692.
- (6) Kang, P.; Chen, Z.; Brookhart, M.; Meyer, T. *Top. Catal.* **2014**, *58*, 30-45.
- (7) Kang, P.; Cheng, C.; Chen, Z.; Schauer, C. K.; Meyer, T. J.; Brookhart, M. J. *Am. Chem. Soc.* **2012**, *134*, 5500-5503.
- (8) Kang, P.; Meyer, T. J.; Brookhart, M. *Chem. Sci.* **2013**, *4*, 3497-3502.
- (9) Kang, P.; Zhang, S.; Meyer, T. J.; Brookhart, M. *Angew. Chem. Int. Ed.* **2014**, *126*, 8853-8857.
- (10) Taheri, A.; Thompson, E. J.; Fettingner, J. C.; Berben, L. A. *ACS Catal.* **2015**, *5*, 7140-7151.
- (11) Taheri, A.; Berben, L. A. *Inorg. Chem.* **2016**, *55*, 378-385.
- (12) Johnson, S. I.; Nielsen, R. J.; Goddard, W. A. *ACS Catal.* **2016**, 6362-6371.
- (13) Connelly, S. J.; Wiedner, E. S.; Appel, A. M. *Dalton Trans.* **2015**, *44*, 5933-5938.
- (14) Cheng, T.-Y.; Brunschwig, B. S.; Bullock, R. M. *J. Am. Chem. Soc.* **1998**, *120*, 13121-13137.
- (15) Jeletic, M. S.; Mock, M. T.; Appel, A. M.; Linehan, J. C. *J. Am. Chem. Soc.* **2013**, *135*, 11533-11536.
- (16) Berning, D. E.; Miedaner, A.; Curtis, C. J.; Noll, B. C.; Rakowski DuBois, M. C.; DuBois, D. L. *Organometallics* **2001**, *20*, 1832-1839.
- (17) Ciancanelli, R.; Noll, B. C.; DuBois, D. L.; DuBois, M. R. *J. Am. Chem. Soc.* **2002**, *124*, 2984-2992.
- (18) Price, A. J.; Ciancanelli, R.; Noll, B. C.; Curtis, C. J.; DuBois, D. L.; DuBois, M. R. *Organometallics* **2002**, *21*, 4833-4839.
- (19) Raebiger, J. W.; Miedaner, A.; Curtis, C. J.; Miller, S. M.; Anderson, O. P.; DuBois, D. L. *J. Am. Chem. Soc.* **2004**, *126*, 5502-5514.
- (20) Creutz, C.; Chou, M. H. *J. Am. Chem. Soc.* **2009**, *131*, 2794-2795.
- (21) Tsay, C.; Livesay, B. N.; Ruelas, S.; Yang, J. Y. *J. Am. Chem. Soc.* **2015**, *137*, 14114-14121.
- (22) Pitman, C. L.; Brereton, K. R.; Miller, A. J. M. *J. Am. Chem. Soc.* **2016**, *138*, 2252-2260.
- (23) Albrecht, M.; van Koten, G. *Angew. Chem. Int. Ed.* **2001**, *40*, 3750-3781.
- (24) Solis, B. H.; Hammes-Schiffer, S. *J. Am. Chem. Soc.* **2011**, *133*, 19036-19039.
- (25) Mondal, B.; Neese, F.; Ye, S. *Inorg. Chem.* **2016**, *55*, 5438-5444.
- (26) Wang, D. Y.; Choliy, Y.; Haibach, M. C.; Hartwig, J. F.; Krogh-Jespersen, K.; Goldman, A. S. *J. Am. Chem. Soc.* **2016**, *138*, 149-163.
- (27) Cheng, M.-J.; Bischof, S. M.; Nielsen, R. J.; Goddard Iii, W. A.; Gunnoe, T. B.; Periana, R. A. *Dalton T.* **2012**, *41*, 3758-3763.
- (28) Sandhya, K. S.; Remya, G. S.; Suresh, C. H. *Inorg. Chem.* **2015**, *54*, 11150-11156.
- (29) Mucha, N. T.; Waterman, R. *Organometallics* **2015**, *34*, 3865-3872.
- (30) Hansch, C.; Leo, A.; Taft, R. W. *Chem. Rev.* **1991**, *91*, 165-195.
- (31) Polukeev, A. V.; Marcos, R.; Ahlquist, M. S. G.; Wendt, O. F. *Organometallics* **2016**, *35*, 2600-2608.
- (32) Hebden, T. J.; St. John, A. J.; Gusev, D. G.; Kaminsky, W.; Goldberg, K. I.; Heinekey, D. M. *Angew. Chem. Int. Ed.* **2011**, *50*, 1873-1876.
- (33) Bernskoetter, W. H.; Hanson, S. K.; Buzak, S. K.; Davis, Z.; White, P. S.; Swartz, R.; Goldberg, K. I.; Brookhart, M. J. *Am. Chem. Soc.* **2009**, *131*, 8603-8613.
- (34) Göttker-Schnetmann, I.; Heinekey, D. M.; Brookhart, M. J. *Am. Chem. Soc.* **2006**, *128*, 17114-17119.
- (35) Shaffer, D. W.; Johnson, S. I.; Rheingold, A. L.; Ziller, J. W.; Goddard, W. A.; Nielsen, R. J.; Yang, J. Y. *Inorg. Chem.* **2014**, *53*, 13031-13041.
- (36) Lee, C. T.; Yang, W. T.; Parr, R. G. *Phys. Rev. B* **1988**, *37*, 785-789.
- (37) Francl, M. M.; Pietro, W. J.; Hehre, W. J.; Binkley, J. S.; Gordon, M. S.; Defrees, D. J.; Pople, J. A. *J. Chem. Phys.* **1982**, *77*, 3654-3665.
- (38) Hehre, W. J.; Ditchfie.R; Pople, J. A. *J. Chem. Phys.* **1972**, *56*, 2257-2261.
- (39) Zhao, Y.; Truhlar, D. G. *Theor. Chem. Acc.* **2008**, *120*, 215-241.
- (40) Martin, J. M. L.; Sundermann, A. *J. Chem. Phys.* **2001**, *114*, 3408-3420.
- (41) Clark, T.; Chandrasekhar, J.; Spitznagel, G. W.; Schleyer, P. V. J. *Comp. Chem.* **1983**, *4*, 294-301.
- (42) Putnam, W. E.; McEachern, D. M. J.; Kilpatrick, J. E. J. *Chem. Phys.* **1965**, *42*, 749-755.

- (43) Kelly, C. P.; Cramer, C. J.; Truhlar, D. G. *J. Phys. Chem. B* **2006**, *110*, 16066-16081.
- (44) Grimme, S.; Antony, J.; Ehrlich, S.; Krieg, H. *J. Chem. Phys.* **2010**, *132*, 154104.
- (45) Dojcansky, J.; Heinrich, J. *Chem. Zvesti* **1974**, *28*, 157-159.
- (46) Chase, M. W. J. *NIST-JANAF Thermochemical Tables, Fourth Edition*, 1998.
- (47) Tissandier, M. D.; Cowen, K. A.; Feng, W. Y.; Gundlach, E.; Cohen, M. H.; Earhart, A. D.; Coe, J. V.; Tuttle, T. R. *J. Phys. Chem. A* **1998**, *102*, 7787-7794.
- (48) Kelly, C. P.; Cramer, C. J.; Truhlar, D. G. *J. Phys. Chem. B* **2006**, *111*, 408-422.
- (49) Kitagawa, Y.; Saito, T.; Ito, M.; Shoji, M.; Koizumi, K.; Yamanaka, S.; Kawakami, T.; Okumura, M.; Yamaguchi, K. *Chem. Phys. Lett.* **2007**, *442*, 445-450.
- (50) Wertz, D. H. *J. Am. Chem. Soc.* **1980**, *102*, 5316-5322.
- (51) Bochevarov, A. D.; Harder, E.; Hughes, T. F.; Greenwood, J. R.; Braden, D. A.; Philipp, D. M.; Rinaldo, D.; Halls, M. D.; Zhang, J.; Friesner, R. A. *Int. J. Quantum Chem.* **2013**, *113*, 2110-2142.
- (52) Creutz, C.; Chou, M. H.; Hou, H.; Muckerman, J. T. *Inorg. Chem.* **2010**, *49*, 9809-9822.
- (53) Huang, Y.; Nielsen, R. J.; Goddard, W. A.; Soriaga, M. P. *J. Am. Chem. Soc.* **2015**, *137*, 6692-6698.
- (54) Evans, M. G.; Polanyi, M. *Trans. Faraday Soc.* **1936**, *32*, 1333-1360.
- (55) Henceforth, for the case where E = CH<sub>2</sub>, we will refer to the pincer as PCNCP, with the hydrogens omitted for simplicity.
- (56) Semproni, S. P.; Milsmann, C.; Chirik, P. J. *J. Am. Chem. Soc.* **2014**.
- (57) Khaskin, E.; Diskin-Posner, Y.; Weiner, L.; Leitun, G.; Milstein, D. *Chem. Commun.* **2013**, *49*, 2771-2773.
- (58) Osadchuk, I.; Tamm, T.; Ahlquist, M. S. G. *Organometallics* **2015**, *34*, 4932-4940.

## Chapter 5

## MECHANISMS FOR HYDROGEN EVOLUTION FOR CP\*RH(BPY)

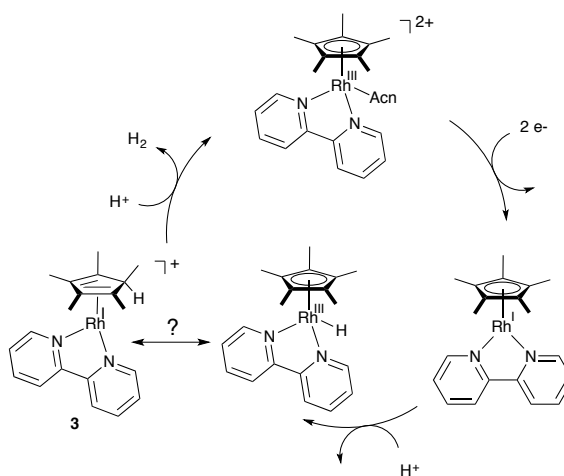
With contributions from James D. Blakemore, Luis Aguirre-Quintana, Sydney Corona, and William A. Goddard III

Some material adapted from:

L. Aguirre Quintana; **S.I. Johnson**; S.L. Corona; W. Villatoro; W.A. Goddard III; M. K. Takase; D. G. VanderVelde; J. R. Winkler; H. B. Gray; and J.D. Blakemore; Proton-Hydride Tautomerism in Hydrogen Evolution Catalysis. *Proceedings of the National Academy of Sciences* 2016, 113 (23), 6409-6414.

## Introduction

In the previous two chapters, solar fuels have presented themselves as a means for solar energy storage.<sup>1,2</sup> However, these chapters focused solely on CO<sub>2</sub> reduction, a scheme in which hydrogen production presents itself as a nuisance. However, in the case where hydrogen is selectively produced, it too is considered a viable solar fuel. In the ideal hydrogen evolution reaction (HER) based solar fuels scheme, a catalyst would use protons and electrons harvested from solar-powered water splitting and convert them to hydrogen.<sup>1,2</sup> This fuel-forming catalyst should be earth-abundant and have a high turnover frequency in order to provide low-cost energy storage. Nonetheless, the atomistic details of even the simplest fuel-forming reaction, combining two H<sup>+</sup> and two e<sup>-</sup> with the aid of a catalyst to form H<sub>2</sub>, are often poorly understood.



**Scheme 5.1:** Previous mechanisms for hydrogen evolution in this catalyst involved the generation of a Rh<sup>III</sup> hydride. Experimentally, protonation of the Cp\* is seen.



One example of a hydrogen evolution reaction (HER) catalyst is the Cp\*Rh(bpy) catalyst [Cp\* = pentamethylcyclopentadienyl, bpy = 2,2'-bipyridine]. This catalyst was originally synthesized by Maitlis et al.<sup>3</sup> and was used in a colloidal suspension by Graetzel et al. to evolve hydrogen.<sup>4</sup> The reduced form of the catalyst was recently isolated and crystallized by Blakemore and coworkers.<sup>5</sup> HER in Cp\*Rh(bpy) was previously thought to occur first by a two electron reduction to the Rh<sup>I</sup> catalyst, followed by protonation at the metal as shown in Scheme 5.1.<sup>4</sup> However, as shown by Aguirre-Quintana et al., upon protonation by a weak acid, triethylammonium (TEAH<sup>+</sup>), protonation of the Cp\* ring was observed, with all protonation occurring at the *endo* position (oriented towards the metal center).<sup>6</sup> The presence of the protonated ligand and its position is confirmed via NMR and X-Ray crystallography. With the weaker acid alone, the protonated complex does not produce H<sub>2</sub>. However, when the Cp\*H complex is in the presence of a stronger acid, protonated dimethylformamide (DMF), HER goes to completion, liberating H<sub>2</sub> with unity yield.<sup>6</sup> Evidence of protonated Cp\* ligands in transition metal complexes has been seen<sup>7-9</sup>; this is the first time hydrogen evolution had been seen from a complex of this type. It is also of note that the same intermediate is also seen in water.<sup>10</sup> Understanding the role of this complex is key to better understanding of HER, as several catalysts involving protonated ligands have been successful for HER.<sup>11-13</sup> One catalyst of note, a nickel metalloporphyrin system augmented with a pendant base, has been shown to have two pathways for HER, one operative with weak acids and another operative for the case of strong acids.<sup>11</sup> Neither pathway involves formation of a traditional metal hydride.

In this work we seek to answer how protonation occurs at the Cp\* ligand, as well as understand how hydrogen evolution occurs from the singly protonated compound. In this way, we can understand the true nature of Cp\*Rh(bpy) as an HER catalyst and potentially use these lessons to develop earth abundant analogues. It is important to study this specific catalyst because of the ubiquity of Cp\* as a ligand in organometallic catalysis. The results with this compound contradict the usual notion that Cp\* is an inert ancillary ligand. To the contrary, it now seems that Cp\*/Cp\*H may be a useful interconvertible motif that relies on close ligand-metal cooperation to drive successful catalysis. Towards this goal, density functional theory (DFT) will be used to locate intermediates and transition states along

pathways for evolving hydrogen. In particular, we will be seeking to understand if the protonated ligand is responsible for hydrogen evolution.

## Methods

All calculations were performed using density functional theory. Geometry, frequency, and solvation calculations were completed with the B3LYP functional<sup>14,15</sup> modified by a dispersion correction<sup>16</sup> with 6-31G\*\* basis set on organics.<sup>17,18</sup> Rh atoms were treated with the Los Alamos small core potential and 2- $\zeta$  basis set.<sup>19</sup> All single point energy calculations were completed with the M06 functional<sup>20</sup>, again modified with a dispersion correction.<sup>16</sup> The 6-311G\*\*++ basis was used for on organics. Rh was treated with the 3- $\zeta$  LACV3P\*\*++ basis set, augmented with f and diffuse functions.<sup>21,22</sup> Solvation in acetonitrile was applied using the Poisson Boltzmann polarizable continuum model with a dielectric constant and probe radius of 37.5 and 2.19 Å. To calculate the free energy of acetonitrile, the 1 atm ideal gas free energy was calculated and the empirical energy of vaporization, 1.27 kcal/mol was subtracted.<sup>23</sup> Free energies were computed in according to the following equation:

$$G = E_{M06} + G_{solv} + E_{ZPE} + H_{vib} + H_{TR} - T(S_{vib} + S_{elec})$$

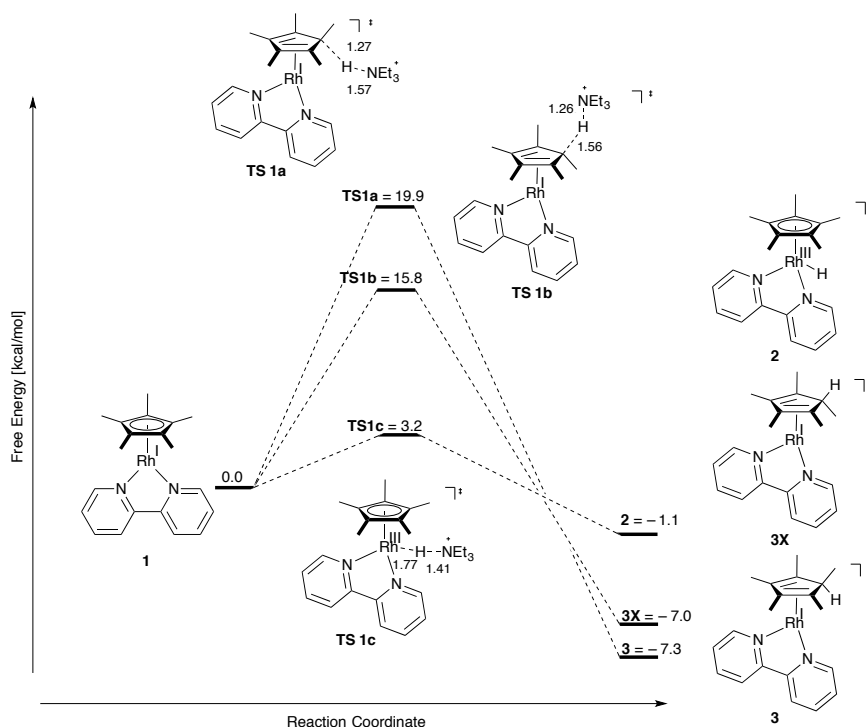
Where zero point energies, enthalpic, and entropic effects are provided by frequency calculations at room temperature. To validate calculations with the acids, the  $pK_a$  values of triethylammonium (TEAH<sup>+</sup>) and protonated dimethylformamide (HDMF) were calculated in acetonitrile and compared to experiment. For these calculations, the value of the proton in solution was calculated from its gas phase free energy ( $G_{H^+} = H - TS = 2.5k_b t - T \times 26.04 = -6.3$  kcal/mol) plus the empirical free energy of solvation in water at concentration of 1 M ( $\Delta G_{H^+,solv} = -265.9 + k_b t \ln(24.5)$ ), as found by Tissandier et al.<sup>24</sup> To account for solvation in acetonitrile, the free energy of intersolvent proton transfer of 14.1 kcal/mol was used in accordance with measurements by Roberts and coworkers.<sup>25,26</sup> This yields a value of -256.2 kcal/mol for the free energy of the proton solvated in acetonitrile. Using this value, the  $pK_a$  of triethylammonium and HDMF in acetonitrile was calculated as 18.5 and 4.0 respectively, which compares well to the experimentally measured value of 18.8 and 6.1. In calculations involving the Rh complexes, the explicit acid complexes themselves were used, rather than the energy of the free proton. All calculations were completed in Jaguar.<sup>27</sup>

## Results and Discussion

### Routes to First Protonation

First, we aim to show how protonation occurs at the Cp\* ring. Scheme 5.2 shows the various protonation routes that can be taken by this catalyst to form the protonated species. In this scheme, all free energies are referenced to **1**, the Rh<sup>I</sup> species with TEAH<sup>+</sup> as the acid.

Thermodynamically, three intermediate states are available. Complex **2** is downhill by 1.1 kcal/mol and features a traditional Rh<sup>III</sup> hydride, while complexes **3X** and **3** are the exo and endo Rh<sup>I</sup> with protonated ligand. These molecules are both exergonic to form in the presence of TEAH<sup>+</sup> by 7.0 and 7.3 kcal/mol, respectively. The geometry of complex **3** features visible ring slippage in the Cp\* moiety, forming an η<sup>4</sup> bound dienyl Cp\*H ligand. To form these protonated species, three separate routes are shown.



**Scheme 5.2:** Protonation at the metal center to form the traditional hydride is the most kinetically feasible pathway.

The first is through **TS 1a**, which features direct protonation of the carbon in Cp\* by TEAH<sup>+</sup> to form **3**. In this transition state, the aromaticity of the Cp\* ring is broken, allowing the methyl group to bend upwards and the carbon in the ring to accept a proton. The

distance between proton and the carbon on the ring in this transition state is 1.57 Å. At 19.9 kcal/mol, the barrier for this route indicates a kinetically slow reaction, which may be expected due to the similarities between this reaction and C-H activation. This also may be attributed to steric effects, as the TEAH<sup>+</sup> is quite bulky. Under this hypothesis, one may surmise that protonation from the top of the Cp\* ring may be more favourable. This transition state is demonstrated in **TS 1b**, where the TEAH<sup>+</sup> attacks from the top to form the slightly higher in energy *exo* analog, **3X**. This barrier is lower in energy, at a barrier of 15.8 kcal/mol but features a transition state with a slightly shorter H-C<sub>Cp\*</sub> distance of 1.56 Å. The reduced barrier and C-H distance support the fact that steric bulk in the acid plays a role in preventing direct protonation at the ring, but is not the only factor present. The final option is direct protonation of the metal, which is represented by **TS 1c**. At 3.0 kcal/mol, this transition state is the most accessible. At 1.41 Å, this transition state features the longest H-N distance, implying its late nature. This may be a product of sterics, as the TEAH<sup>+</sup> is unable to deeply penetrate the cavity left by the metal and the Cp\*.

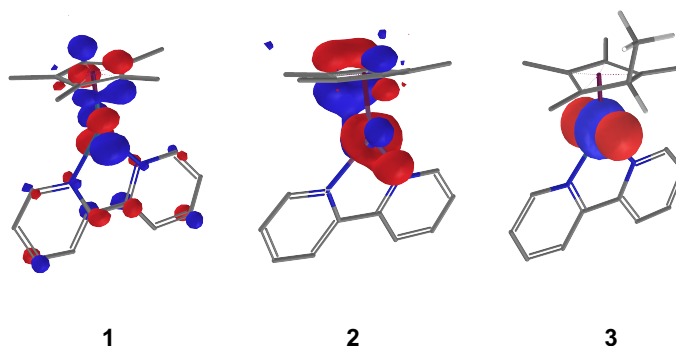
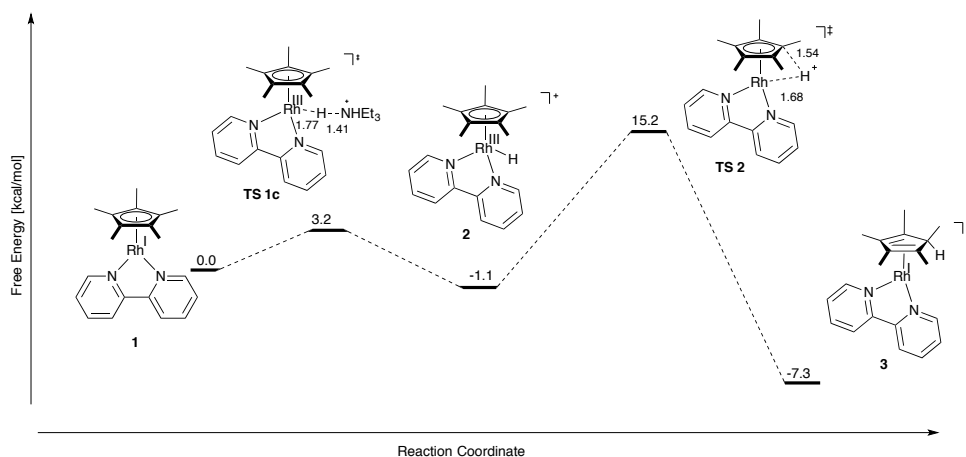


**Figure 5.1:** Frontier orbitals of complexes **1**, **2**, and **3**. While in the original complex the HOMO is delocalized, on **3** it is localized in a  $d_{z^2}$  orbital.

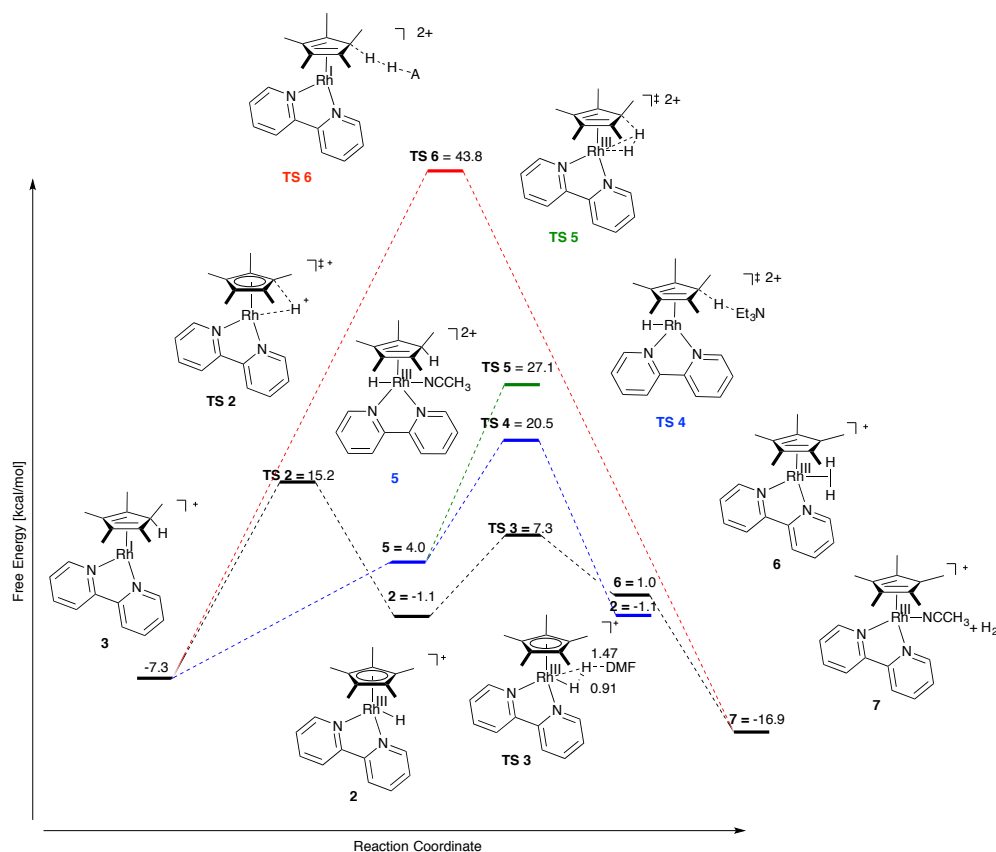
The frontier orbitals of the starting complex, as well as final two thermodynamic products are seen in Figure 5.1. The HOMO in **1** is largely delocalized over the  $p_z$  orbitals of the bipyridine, the  $d_{yz}$  orbital of the metal, and the  $p_z$  orbitals of the carbons in the Cp\* ring. Upon protonation at the metal center, the HOMO is made up of a molecular orbital consisting of the  $s$  orbital of the hydride, the  $d_{z^2}$  of Rh, and the  $\pi$  system of the Cp\*.

complex **3**, the HOMO is localized almost solely in the  $d_{z^2}$  orbital, implying that the Rh behaves formally as a  $Rh^I$  center.



**Scheme 5.3:** After formation of the hydride, the proton can bridge, forming the  $Rh^I$  complex with the protonated  $Cp^*$  ligand.

While metal protonation is the most kinetically feasible, it is still true that the thermodynamically preferred and experimentally observed complex is **3**. The product **2** features a long Rh-H bond of 1.56 Å, which implies that it is rather weak; however, it is a true hydride and is not bridging to the  $Cp^*$  (as evidenced by the distance:  $H-C_{Cp^*} = 2.72$  Å). Due to the weak Rh-H bond, a transition state between **2** and **3** may be feasible. This is shown in Scheme 5.3. From **2**, the proton is able to bridge to the  $Cp^*$  with a thermally accessible barrier of 15.2 kcal/mol. The reverse reaction from the protonated  $Cp^*$  complex to the  $Rh^{III}$  is 22.5 kcal/mol higher, which is likely insurmountable at room temperature. In the weak acid case, this is the product and no hydrogen is produced.



**Scheme 5.4:** Routes involving a second protonation by HDMF. Energies in kcal/mol and bond lengths in Ångstroms.

#### *Protonation from the Cp\*H complex*

In the presence of a stronger acid HDMF (protonated dimethylformamide,  $pK_a = 6.1$ ), hydrogen is evolved, both from the starting complex **1** and the resulting complex **3**. Various routes for this process is shown in Scheme 5.4. From the starting state **3**, several mechanisms for the formation of hydrogen can be seen. Direct acid attack at the protonated Cp\*H can be seen in **TS 6**, wherein Cp\*H acts as an organic hydride donor. As had been previously shown, the HOMO in **3** is largely localized on the Rh center as a formal Rh<sup>I</sup>. This means that the electron density to make the hydride must be passed through the  $\pi$  system of the Cp\* ring in order to form the hydride. The calculated barrier for this reaction is 43.8 kcal/mol, far too high for a room temperature H<sub>2</sub> evolution reaction. This high barrier is somewhat to be expected, as second order rate constants for hydride transfer from aryl rings

to carbocation hydride acceptors are often several orders of magnitude smaller than their transition metal hydride cousins.<sup>28-30</sup>

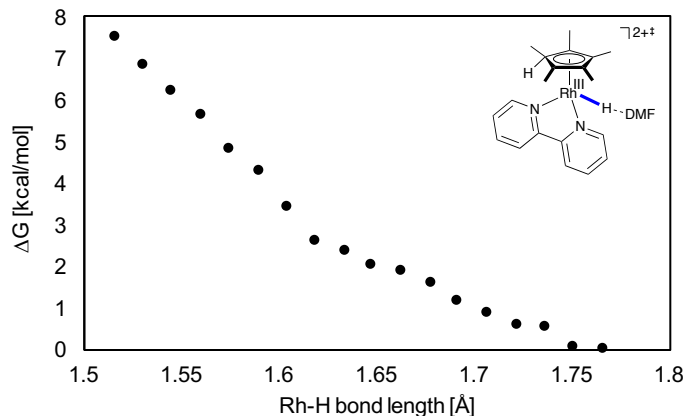


**Figure 5.2:** Relaxed coordinate scan moving the Rh-H distance 0.015 Å each step.

Alternatively, the protonated Cp\* complex **3** can undergo a barrierless second protonation, as shown in blue to form **5**. Complex **5** is the *trans* isomer of the doubly protonated complex and the lowest energy isomer of all possible combinations. It features a loosely coordinated acetonitrile opposite the hydride. The analogue sans acetonitrile is higher in energy by 8 kcal/mol. The *cis* isomers with and without acetonitrile are higher in energy by 3.3 and 15.1 kcal/mol, respectively. In order to establish the barrierless nature of the protonation to form **5**, a relaxed coordinate scan of the Rh-H bond distance from 1.766 to the resting distance of 1.516 Å with a step size of 0.015 Å was completed. The results of the scan can be seen in Figure 5.2, in which the energy is monotonically increasing with decreasing Rh-H distance. From **5**, the potential energy surface branches into two potential routes. The higher barrier route through **TS 5** involves a metathesis pathway, wherein the Cp\* ring rotates and the proton from the ring is passed back to the metal. The geometry of this transition state is unique, as the proton is not passed directly from overhead to the metal-bound proton, but rather from a slightly rotated position onto the Rh (dihedral angle  $\angle$  H-Rh-C-H of 45.0°). A representation of this geometry is shown in Figure 5.3a. In theory, this would go on to form **6**, the dihydrogen complex present as a short lived intermediate before the thermodynamically favored release of hydrogen, shown by **7**. However, at a barrier of 27.1 kcal/mol, this is also unfeasible at room temperature for hydrogen evolution.

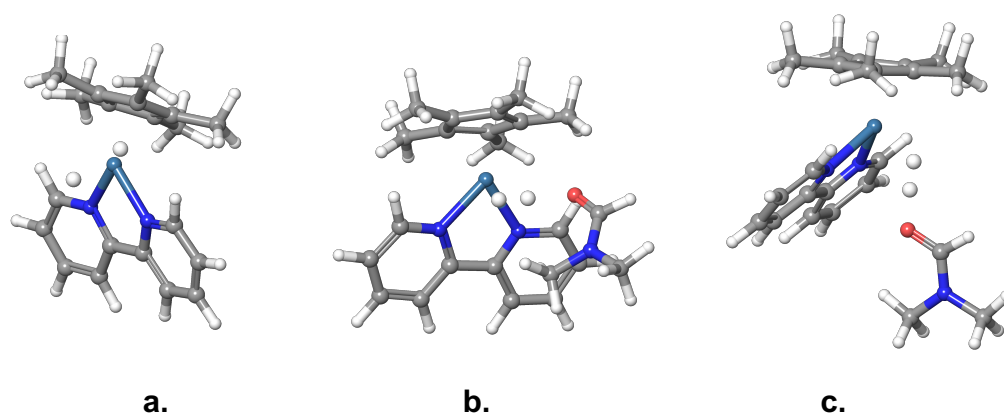


**Figure 5.3:** Relevant transition states, a. **TS 5**; b. **TS 3**; c. Attack on hydride from bottom.

It is important to note that in the experimental system, two equivalents of HDMF are added. The first equivalent protonates the TEA in solution, which completed the first protonation. The second equivalent is then thought to provide the second proton for the formation of  $H_2$ , supported by gas chromatography measurements.<sup>6</sup> Especially while the first equivalent of HDMF is being added, some TEA may be available in solution to abstract a proton. In some heterogeneous systems, protonation occurs at one location to stabilize the system for a second protonation, only to be abstracted later.<sup>31</sup> This is shown by the alternative transition state **TS 4**, wherein TEA abstracts a proton from the ring to form the singly protonated hydride **2**. The barrier for this is similarly high at 20.5 kcal/mol. The analogous transition state with DMF acting as base has a higher barrier of 24.5 kcal/mol, which is reasonable considering that TEA is more basic than DMF. These transition states rule out participation by the protonated  $Cp^*$ , leaving only those routes involving the traditional hydride and concerted routes and.

Two routes exist from the traditional hydride **2**. The first, **TS 3**, features a side-on attack from HDMF to form the dihydrogen adduct **6**. This barrier is quite feasible at 7.3 kcal/mol, which is only 8.4 kcal/mol uphill from **3**. The geometry of this complex can be seen in Figure 5.3b. In this transition state, the Rh-H length of 1.71 Å is lengthened from the previous Rh-H bond length of 1.56 Å, but is not as far as the dihydride adduct (**6**) Rh-H lengths of 1.93 Å. The H-H bond length in the transition state is 0.91 Å and relaxes to a bond length in **6** to 0.783 Å. This H-H bond length is indicative of a classical hydrogen



complex, rather than a bound  $H_2$ , or a dihydride.<sup>32</sup> This implies that in this transition state, we are moving from a hydride to a very loosely bound  $H_2$  adduct that may be short lived, if exists at all.

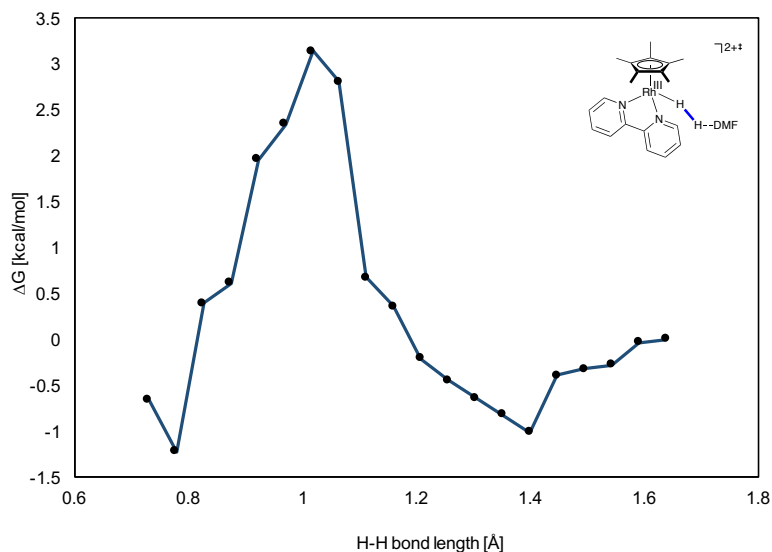


**Figure 5.4:** Potential energy surface along a decreasing H-H bond distance with acid attack from the bottom.

A second route found via a relaxed coordinate scan features attack from the bottom in the direction of the bipyridine ligand. The full free energy surface for this is shown in Figure 5.4. The coordinate scan began with a minimized Rh-H species **3** with HDMF nearby, which is taken as the reference state for this calculation. The H-H bond distance was then shortened by 0.048 Å and the new geometry was minimized at each step. The process repeated itself for H-H distances ranging from 1.638 to 0.538 Å, though only distances to 0.729 Å are included in this plot. Distances smaller than this showed a large increase in energy due to atomic repulsion. At each point, the full free energy including enthalpies and entropies is calculated. As the H-H interatomic distance is decreased, a shallow well centered around H-H = 1.399 Å develops, though the energy of this well (~1 kcal/mol) is smaller than the accepted error for DFT. This is followed by a barrier in the potential energy surface of 3.1 kcal/mol at an H-H distance of 1.016 Å. This is an earlier transition state than the side-on attack, as both the H-H and the protic H-O distance are much closer to the corresponding distances in the reactants. Similarly, the Rh hydride distance of 1.66 Å implies

the early nature of the transition state. A representation of the complex at the maximum along the potential energy surface is seen in Figure 5.3c. As the H-H distance continues to decrease, the barrier is overcome and a minimum of -1.2 kcal/mol is seen at an H-H distance of 0.777 Å. In this state, the Rh-H distances are 1.86 and 2.08 for the original hydride and proton respectively. This geometry could imply that **6** never truly forms in solution. However, it is of note that both low barrier hydride protonation routes involve participation of both the hydride and the metal, a scheme seen previously in biological<sup>33,34</sup>, heterogeneous<sup>31</sup>, and inorganic<sup>35,36</sup> systems. It is also important to note that both low barrier pathways occurring via the hydride lower in energy than protonation via the bridging pathway, **TS 2**. In the presence of strong acid, it is likely that the ring will not participate as fast kinetics will drive the system towards hydrogen evolution. While this suggests that **3** is off-path in the strong acid case, it is on path in the weak acid case. Previous work by Solis et al. has identified other HER catalysts where two separate cycles exist for differing acid strengths.<sup>11</sup> Both works imply that in kinetic studies, it is important to consider that multiple paths can exist that are accessible in differing conditions.

In isolation, formation of the hydride species **2** from **3** encounters a barrier of 22.5 kcal/mol, which is quite high. However, a concerted route by which the protons approach simultaneously is a possibility. As an isolated transition state, this proved quite difficult to locate. However, the same step approach used in Figures 5.2 and 5.3 was used here, except with two variables rather than one. The first variable was the Rh-H distance, where the proton in question is the one bound to Cp\*. This distance was increased in increments of 0.260 Å. The second variable was the distance between the proton on the Cp\* and the proton of the acid, which was decreased in increments of 0.250 Å. This resulted in 42 individual geometries and energies, which can be seen in the contour plot in Figure 5.5.

One can see several critical points, the geometries of which are included in the figure. Point A is a local minimum which represents the protonated Cp\* complex, **2**, with the acid nearby. Another critical point can be seen in B., where the proton has migrated to form a loosely bound hydride (Rh-H distance of 1.697 Å), with the acid oriented towards it. This state is interesting, as it shows a shallow minimum in preparation for protonation of the hydride. The final critical point, C, is the point post-protonation, where H<sub>2</sub> has been released and can

go into solution. One additional feature is the barrier in the top middle of the figure. This large barrier is one previously discussed, **TS 6**, where HER occurs directly from the **2**.

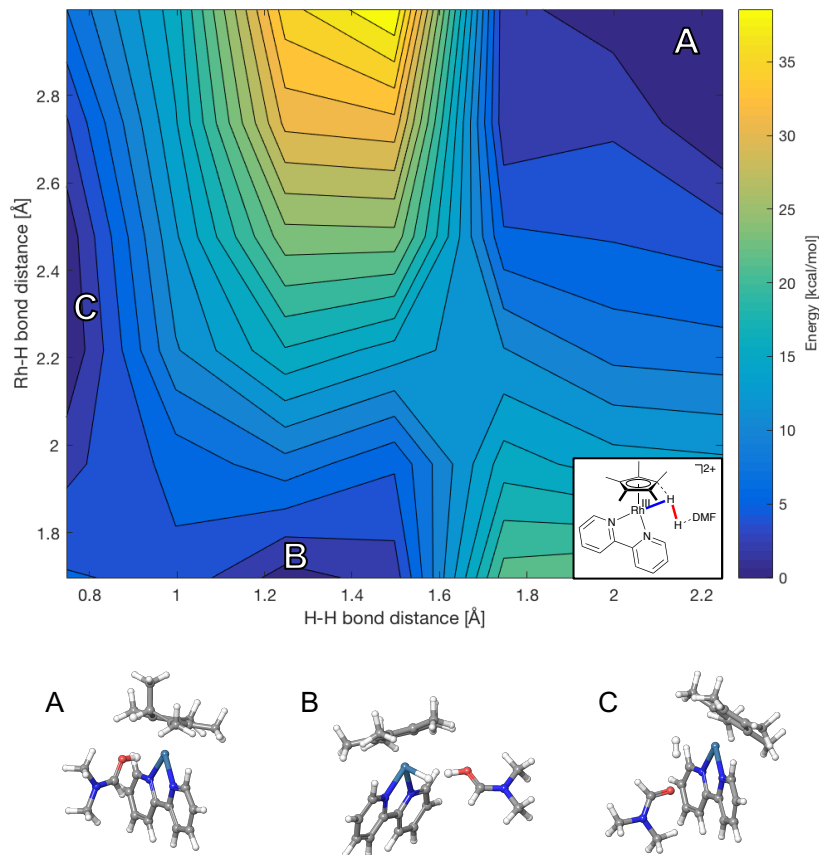


**Figure 5.5:** Varying the H-H distance and the Rh-H distances yields several critical points of interest, geometries of which can be seen in A., B., and C.

The path connecting A and B features a barrier around  $\sim 12$  kcal/mol, which is lower than the defined barrier in **TS 2** and is, more importantly, accessible at room temperature. The barrier is reduced by the simultaneous movement of the proton on Cp\* towards Rh and the two protons together. The figure suggests that the potential energy surface for this system is quite flat. The barrier region itself is quite broad, which indicates why a transition state was difficult to locate. A higher resolution search (which is in the works) will yield more information. However, this implies that from **2**, a concerted route towards B and then towards C, with the release of H<sub>2</sub>, is the only feasible path towards hydrogen production.

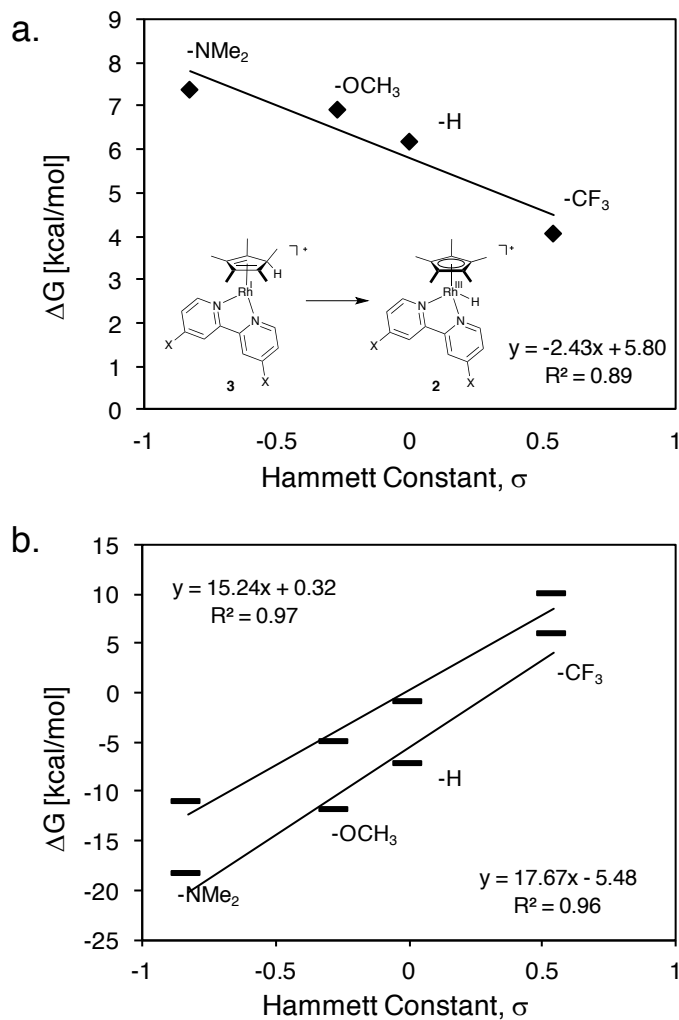
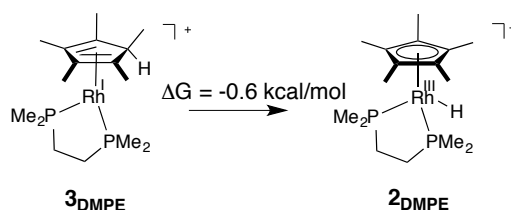


**Figure 5.6:** 5.6a.) Linear correlation between the Hammett constant of functional groups on bpy and energy difference between complexes 2 and 3 shows the effect of bpy on this complex. 5.6b.) As the functional groups become more electron withdrawing, the complex becomes harder to protonate.

In order to gauge substituent effects on the electronic structure of the  $\text{Cp}^*\text{Rh}(\text{bpy})$  complex, several functional groups were substituted in the *para* position of the bipyridine ligand. The computationally calculated difference between the protonated  $\text{Cp}^*$  ligand and the  $\text{Rh}^{\text{III}}$  hydride was plotted against the Hammett constant ( $\sigma_p$ ) of the functional groups in Figure 5.6a. Hammett constants ranging from -0.83 to 0.54 (electron donating to withdrawing) were used.<sup>37</sup> There is a linear relationship between  $\Delta G$  and  $\sigma_p$ , suggesting that within the bpy

family, variation of the electronic structure is quite small. Though not shown here, this is also corroborated by little change in the Mulliken populations of the nitrogen, rhodium, and relevant carbon atoms among different functional groups. One implication that can be gleaned from this is that in order to favor the formation of the hydride, **2**, a functional group with a Hammett constant of  $\sim 2.5$  would be needed, suggesting that only an incredibly electron donating group can achieve this within the bpy family. It would thus seem that the bpy backbone is very adept at absorbing the electronic effect of the functional group, making it an excellent candidate for surface attachment. One could surmise that a bpy-based rhodium catalyst bound to a surface would likely perform similarly to the homogeneous analog.



**Scheme 5.5:** The hydride is slightly favored in phosphine-based ligand sets.

Intuitively, one might expect the more electron donating ligands to have a smaller  $\Delta G$  between complexes **2** and **3**, as more electron density on the metal would favor the formation of the hydride. Nonetheless, this is not seen. Reasons for this can be seen in Figure 5.6b, in which the energy to protonate **2** and **3** from **1** are plotted against Hammett Constant. As the bpy ligand becomes more electron withdrawing, the overall metal complex becomes harder to protonate. This effect is felt more strongly at the metal center and the hydride becomes harder to form more rapidly with respect to electronic effects than the protonated Cp\*, as indicated by the differing slopes of the trend lines.

However, once one travels outside the bpy family, one sees a different story. Using 1,2-bis(dimethylphosphino)ethyl (dmpe) groups instead of bpy in a toy system, the  $\Delta G$  is shifted just slightly in favor of the Rh<sup>III</sup> hydride, as shown in Scheme 5.5. Previously a diphosphine Rh hydride had been seen with the loss of a Cp\*H complex upon exposure to H<sub>2</sub>.<sup>8</sup> Examination of the Mulliken populations shows significantly less positive character on the

rhodium atom, showing the electron-donating role of the phosphine groups. This implies that binding to the Cp\* is not a given, but rather a characteristic of the molecule as a whole. The bpy ligand depletes the Rh metal center of electron density, resulting in a weak metal hydride bond. This weak bond is so disfavored thermodynamically that it is exchanged for the stronger C-H bond at the cost of some aromaticity in the Cp\* ring.

## Conclusions

In this study, we have investigated the formation of the unique Cp\*H adduct in Cp\*Rh(bpy), showing that protonation by a weak acid first occurs at the metal and then the proton bridges to the Cp\* to form the *endo* protonated thermodynamic product. This complex is competent for hydrogen evolution upon exposure to HDMF and does so through a combined bridge/protonation pathway. Under exposure to a strong acid, the ring is never likely implicated. Modification of the bpy ligand shows that the thermodynamic product is always the protonated Cp\* ligand. However, this changes with the use of diphosphine ligands. This study and catalyst highlight the many accessible pathways to HER, which may be achieved by simply differing conditions in a single catalyst. In some respects, it serves as a cautionary tale for kinetic studies, as the “slower” path may not be the dominant one in typical catalysis.

## References

- (1) Gray, H. B. *Nat. Chem.* **2009**, *1*, 7-7.
- (2) Lewis, N. S.; Nocera, D. G. *Proc. Natl. Acad. Sci. USA* **2006**, *103*, 15729-15735.
- (3) Maitlis, P. M. *Acc. Chem. Res.* **1978**, *11*, 301-307.
- (4) Kölle, U.; Grützel, M. *Angew. Chem. Int. Ed.* **1987**, *26*, 567-570.
- (5) Blakemore, J. D.; Hernandez, E. S.; Sattler, W.; Hunter, B. M.; Henling, L. M.; Brunshwig, B. S.; Gray, H. B. *Polyhedron* **2014**, *84*, 14-18.
- (6) Quintana, L. M. A.; Johnson, S. I.; Corona, S. L.; Villatoro, W.; Goddard, W. A.; Takase, M. K.; VanderVelde, D. G.; Winkler, J. R.; Gray, H. B.; Blakemore, J. D. *Proc. Natl. Acad. Sci. USA* **2016**, *113*, 6409-6414.
- (7) Gusev, O. V.; Denisovich, L. I.; Peterleitner, M. G.; Rubezhov, A. Z.; Ustynyuk, N. A.; Maitlis, P. M. *J. Organomet. Chem.* **1993**, *452*, 219-222.
- (8) Jones, W. D.; Kuykendall, V. L.; Selmecky, A. D. *Organometallics* **1991**, *10*, 1577-1586.
- (9) Zamorano, A.; Rendón, N.; Valpuesta, J. E. V.; Álvarez, E.; Carmona, E. *Inorg. Chem.* **2015**, *54*, 6573-6581.
- (10) Pitman, C. L.; Finster, O. N. L.; Miller, A. J. M. *Chem. Comm.* **2016**, *52*, 9105-9108.
- (11) Solis, B. H.; Maher, A. G.; Dogutan, D. K.; Nocera, D. G.; Hammes-Schiffer, S. *Proc. Natl. Acad. Sci. USA* **2016**, *113*, 485-492.
- (12) Solis, B. H.; Maher, A. G.; Honda, T.; Powers, D. C.; Nocera, D. G.; Hammes-Schiffer, S. *ACS Catal.* **2014**, *4*, 4516-4526.
- (13) Lacy, D. C.; Roberts, G. M.; Peters, J. C. *J. Am. Chem. Soc.* **2015**, *137*, 4860-4864.
- (14) Becke, A. D. *J. Chem. Phys.* **1993**, *98*, 5648-5652.
- (15) Lee, C. T.; Yang, W. T.; Parr, R. G. *Phys. Rev. B* **1988**, *37*, 785-789.
- (16) Grimme, S.; Antony, J.; Ehrlich, S.; Krieg, H. *J. Chem. Phys.* **2010**, *132*, 154104.
- (17) Francl, M. M.; Pietro, W. J.; Hehre, W. J.; Binkley, J. S.; Gordon, M. S.; Defrees, D. J.; Pople, J. A. *J. Chem. Phys.* **1982**, *77*, 3654-3665.
- (18) Hehre, W. J.; Ditchfie.R; Pople, J. A. *J. Chem. Phys.* **1972**, *56*, 2257-2261.
- (19) Hay, P. J.; Wadt, W. R. *J. Chem. Phys.* **1985**, *82*, 299-310.
- (20) Zhao, Y.; Truhlar, D. G. *Theor. Chem. Acc.* **2008**, *120*, 215-241.
- (21) Krishnan, R.; Binkley, J. S.; Seeger, R.; Pople, J. A. *J. Chem. Phys.* **1980**, *72*, 650-654.
- (22) Clark, T.; Chandrasekhar, J.; Spitznagel, G. W.; Schleyer, P. V. *J. Comp. Chem.* **1983**, *4*, 294-301.
- (23) Bridgeman, O. C.; Aldrich, E.W., *J. Heat Transfer* **1964**, *86*, 279-286.
- (24) Tissandier, M. D.; Cowen, K. A.; Feng, W. Y.; Gundlach, E.; Cohen, M. H.; Earhart, A. D.; Coe, J. V.; Tuttle, T. R. *J. Phys. Chem. A* **1998**, *102*, 7787-7794.
- (25) Pegis, M. L.; Roberts, J. A. S.; Wasylenko, D. J.; Mader, E. A.; Appel, A. M.; Mayer, J. M. *Inorg. Chem.* **2015**, *54*, 11883-11888.
- (26) Roberts, J. A. S.; Bullock, R. M. *Inorg. Chem.* **2013**, *52*, 3823-3835.
- (27) Bochevarov, A. D.; Harder, E.; Hughes, T. F.; Greenwood, J. R.; Braden, D. A.; Philipp, D. M.; Rinaldo, D.; Halls, M. D.; Zhang, J.; Friesner, R. A. *Int. J. Quantum Chem.* **2013**, *113*, 2110-2142.
- (28) Horn, M.; Schappele, L. H.; Lang-Wittkowski, G.; Mayr, H.; Ofial, A. R. *Chem. Eur. J.* **2013**, *19*, 249-263.
- (29) Cheng, T.-Y.; Brunshwig, B. S.; Bullock, R. M. *J. Am. Chem. Soc.* **1998**, *120*, 13121-13137.
- (30) Mayr, H.; Lang, G.; Ofial, A. R. *J. Am. Chem. Soc.* **2002**, *124*, 4076-4083.
- (31) Huang, Y.; Nielsen, R. J.; Goddard, W. A.; Soriaga, M. P. *J. Am. Chem. Soc.* **2015**, *137*, 6692-6698.
- (32) Crabtree, R. H. *Chem. Rev.* **2016**, *116*, 8750-8769.
- (33) Eilers, G.; Schwartz, L.; Stein, M.; Zampella, G.; de Gioia, L.; Ott, S.; Lomoth, R. *Chem. Eur. J.* **2007**, *13*, 7075-7084.
- (34) Carroll, M. E.; Barton, B. E.; Rauchfuss, T. B.; Carroll, P. J. *J. Am. Chem. Soc.* **2012**, *134*, 18843-18852.
- (35) Besora, M.; Lledos, A.; Maseras, F. *Chem. Soc. Rev.* **2009**, *38*, 957-966.
- (36) O'Reilly, M. E.; Johnson, S. I.; Nielsen, R. J.; Goddard, W. A.; Gunnoe, T. B. *Organometallics* **2016**.
- (37) Hansch, C.; Leo, A.; Taft, R. W. *Chem. Rev.* **1991**, *91*, 165-195.

*Chapter 6*DESIGN OF ROBUST ATTACHMENT OF BIPYRIDINE LIGANDS TO SI  
FOR THE IMMOBILIZATION OF HOMOGENEOUS CATALYSTS.

With contributions from James D. Blakemore, Robert J. Nielsen, Bruce S. Brunshwig,  
Nathan S. Lewis, Petter Persson and William A. Goddard III

**Introduction**

In previous chapters, we have focused on homogeneous (or solution phase) catalysts for the production of chemical fuels.<sup>1,2</sup> In general, however, catalysts of interest can either be homogenous or heterogeneous (a different phase than the surroundings), each with their advantages. Heterogeneous systems<sup>3,4</sup> offer the advantage of simplified product separation; however single product selectivity can be difficult to achieve, but is key to the efficiency and productivity of fuel-forming devices. Homogenous electrocatalysts are well-known for their selectivity and rate and have been quite successful at selective production of solar fuels; however, product and catalyst separation can be difficult and expensive.<sup>5-8</sup> By immobilizing a homogeneous catalyst to the surface of an electrode, one can ideally combine the advantages of the two systems, while making homogeneous catalysts better for industrial use.<sup>9-13</sup>

Early work on surface immobilization of electrocatalysts often saw the catalysts polymerize on the surface.<sup>14,15</sup> Non-covalent attachment through  $\pi$ - $\pi$  stacking of a catalyst to an electrode has seen moderate success. Using a pyrene-appended (bpy)Re(CO)<sub>3</sub>(Cl) [bpy = 2,2'-bipyridiyl] catalyst on graphitic carbon electrodes, CO<sub>2</sub>RR to CO was achieved. TON of 58 was reached with no H<sub>2</sub> produced, implying success at achieving single product selectivity. However, over the course of several hours, loss of activity was seen due to detachment of the catalyst from the electrode.<sup>16</sup> Kang et al. saw success with their (POCOP)Ir catalyst, which was similarly pyrene-appended to a carbon nanotube gas diffusion electrode. They saw catalysis over 8 hours with a TON of over 54,000.<sup>17</sup> While covalent attachment of an electrocatalyst to an electrode seems like it should be more robust, there has been difficulty in creating a working system.<sup>18</sup> Some covalently-bound catalysts and complexes have displayed stability under reductive conditions, including Co porphyrine systems attached to conductive diamond,<sup>19</sup> vinyl ferrocene on the (111)



surface of Si<sup>20</sup>, Co terpyridine catalysts grafted onto glassy carbon surfaces,<sup>21</sup> and Rh catalysts incorporated into graphite surfaces.<sup>22</sup> In the Co-porphyrine system, a long sp<sup>3</sup> alkane group with a terminal azide was coupled with an alkyne in a Cu<sup>I</sup>-catalyzed click reaction (CuAAC) to covalently bind it to conductive diamond. The catalyst was stable for at least 1000 electrochemical cycles and showed a turnover frequency (TOF) of 0.8 s<sup>-1</sup> for reduction of CO<sub>2</sub> to CO<sup>19</sup>. In the vinyl ferrocene system, a chlorinated Si (111) surface reacted with vinyl-tagged ferrocene. The remaining surface sites were then terminated with methyl groups, using a methyl Grignard reagent. Stable electrochemical cycling was observed. However, it was unclear how the attachment reaction proceeded mechanistically. Despite analogous reactions suggesting that upon attachment, the chlorine would be bound to the linker, little Cl was detected by XPS. Additionally, no IR stretch from a C-C double bond is observed.<sup>23</sup>

Recent work by Lattimer et al. reported attachment of UV-induced attachment of vinyl-tagged bpy transition metal catalyst moiety. The bpy can then undergo cyclometallation to form (bpy)Rh(Cp\*)(Cl), (bpy)Ir(Cp\*)(Cl), and (bpy)Re(acac)<sub>2</sub> [Cp\* = pentamethylcyclopentadienyl, acac = acetylacetonate] surface immobilized catalysts. While experimental evidence showed attachment had been made, upon cyclic voltammetry measurements, the complexes decayed within ~3 electrochemical cycles.<sup>20</sup>

In this work, we study the vinyl bipyridine linker system computationally to elucidate the failure mechanism and provide potential solutions to increase the robustness of this system. This presents an interesting challenge, both due to the multiscale nature of the project and the ubiquity of bpy ligands in catalysis.<sup>24-27</sup> Previous computational work has investigated surface immobilized catalysis in photocatalytic systems<sup>28</sup>, as well as studying immobilized electrocatalysts on Au clusters for comparison to spectroscopy.<sup>29</sup>

## Methods

All geometry optimizations are completed with the B3LYP functional<sup>30,31</sup> with Los Alamos small core potential on transition metals.<sup>32</sup> Double  $\zeta$  basis sets were used on transition metals and 6-311G\*\* basis set were used on organic atoms.<sup>33,34</sup> Poisson Boltzmann polarizable continuum acetonitrile solvent was also used in geometry optimizations. In all spin density and orbital plots *iso* values of 0.005 were used. Silicon clusters were cut along the (111) plane initially using

Crystal<sup>35</sup>, then trimmed on the sides to minimize number of doubly H terminated sides. A similar method has been previously employed for oxide clusters.<sup>36,37</sup> The clusters were designed to be large enough to enable a full ring of Me-Si bonds around the primary bond, in order to minimize the bending of neighboring Me-Si units outward. This bending had been seen in smaller clusters and was shown to affect the electronic behavior of the clusters.<sup>38</sup> Energies for large clusters consist only of electronic and solvation components, due to their large size.

The mechanism for dissociation including transition state calculations was calculated on tristrimethylsilane molecules, as frequency calculations were computationally intractable on the large clusters. All tristrimethylsilane complexes are optimized as per the methods above, however full free energies were calculated involving single point electronic energies, entropies, and enthalpies, in accordance with previously used methods.<sup>39,40</sup> The calculation for single point energies is as follows:

$$G = E_{M06} + G_{solv} + E_{ZPE} + H_{vib} + H_{TR} - T(S_{vib} + S_{elec})$$

Zero point energies,  $E_{ZPE}$ , vibrational enthalpies,  $H_{vib}$ , and vibrational and electronic entropies,  $S_{vib}$  and  $S_{elec}$  respectively, were taken from frequency calculations. Translational and rotational enthalpies were calculated as  $^{12}/_2 k_B T$ . Single point electronic energies were calculated with M06 functional<sup>41</sup> and 6-311G\*\*++ basis set.<sup>42,43</sup> Transition states verified using frequency calculations and intrinsic reaction coordinate calculations. All calculations were completed in Jaguar.<sup>38</sup>

## Results and Discussion

### *Effect of Chlorination on the Linker*

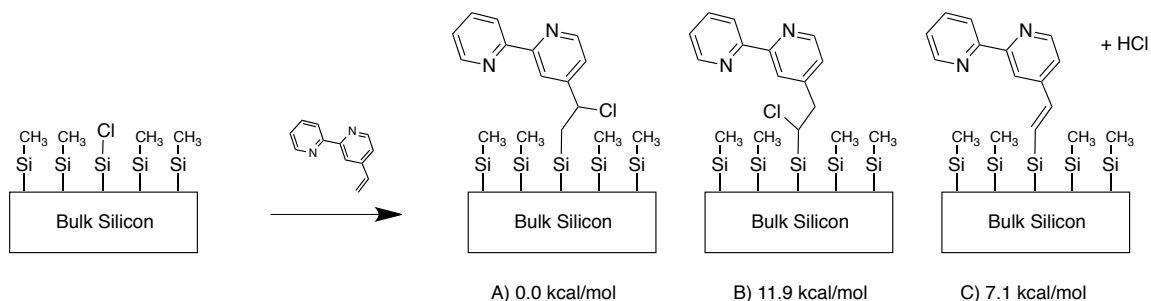


**Figure 6.1:** Relative energies (compared to A) of Cl binding motifs.

Previous experimental and computational work on the hydrogen terminated Si surface has proposed that photons excite electrons within the Si-H bond, breaking off a H radical and leaving a dangling Si radical.<sup>44</sup> This can then react with the vinyl-tagged molecules, which leaves a radical on the  $\beta$ -carbon of the vinyl linker. Recombination of the H and the vinyl radicals yield a linker in which the original H from the surface termination is located on the  $\beta$ -carbon of the linker.<sup>44,45</sup> In the Cl-terminated surface, the analogous attachment scheme would yield a Cl on the  $\beta$ -carbon of the linker. Thermodynamic support for this mechanism can be seen in a comparison of free energies of cluster complexes with chlorine in different positions on the linker, as seen in Figure 6.1. In **A**, the Cl group has gone to the  $\beta$ -carbon. This is the lowest energy conformation. The energy of **B**, which features Cl on the  $\alpha$ -carbon, is higher by 11.9 kcal/mol, largely due to unfavorable steric interaction with the neighboring methyl groups. This is further compared to the  $sp^2$  analog of the linker **C**, which loses HCl in the process of linking, and is similarly higher in energy by 7.1 kcal/mol. This does not feature the same steric repulsion as **A**.

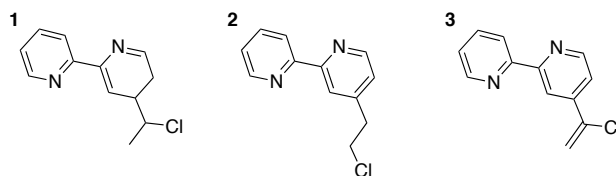


**Figure 6.2:** Molecular complexes with chlorinated linkers.

To further investigate the effect of chlorination on surface-bound complex, large basis set calculations were performed on the molecular bipyridine with Cl substituted throughout the linker, as shown in Figure 6.2. The molecular complexes were singly reduced as they would be on the surface under catalytic conditions. While reduced complexes **2** and **3** remained intact, reduced complex **1** decomposed into a chloride ion and a radical carbon linkage. The radical doublet was mostly centered on the  $\beta$ -carbon of the linker, as supported by atomic charges and spin populations, which are shown in Table 6.1. The spin density plot of the reduced complex is seen in Figure 6.3. It is of note that the spin density extends from one pyridine ring into the linker. The bpy ligand can be reversibly reduced in solution<sup>46</sup>, so it should be able to host an electron without participation of the linker. However, this does not occur for the ligand with the Cl on the  $\beta$  carbon atom, complex **1**, and the linker degrades upon reduction.

**Table 6.1:** Atomic charges and spin populations of the reduced bpy complex

Atom	Atomic Charges	Spin
Cl	-0.88933	0.02026
$\beta$ -carbon	-0.36476	0.69316
$\alpha$ -carbon	-0.10516	-0.05624

When the reduction process is repeated with the complex on a silicon cluster, the same decomposition occurs and the chlorine dissociates into solution. Examination of the spin density plot of the attached complex is similar to that of the molecular species, as shown in Figure 6.4.

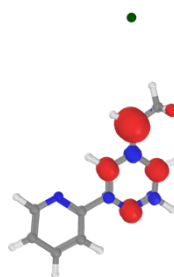


**Figure 6.3:** Spin density of the reduced chlorinated bpy complex. The chloride ion is released and settles at a distance 5.27 Å away from the  $\beta$ -carbon.

Together, the molecular and cluster calculations suggest the following decomposition pathway: during the attachment process, a chlorine radical formed by photoexcitation to break the Si-Cl bond recombines with a radical formed on the  $\beta$ -carbon to create a chlorinated linkage between the bpy complex and the Si surface (Figure 6.1, **A**). As this complex is reduced, the chlorine on the linker dissociates as a chloride ion, leaving a neutral doublet species on the  $\beta$ -carbon. This essentially reverses the attachment process, which allows the  $\nu$ -bpy ligand to dissociate from the surface.

To test this hypothesis, we used tris(trimethyl)silane complex as the analogue for the silicon surface. The proposed mechanism can be seen in Scheme 6.1. Hydrogen terminated silanes have been previously shown to undergo the same photoactivation processes leading to the formation of a silyl radical and reaction with alkenes<sup>47</sup>, so they are valuable analogues to our infinite process.

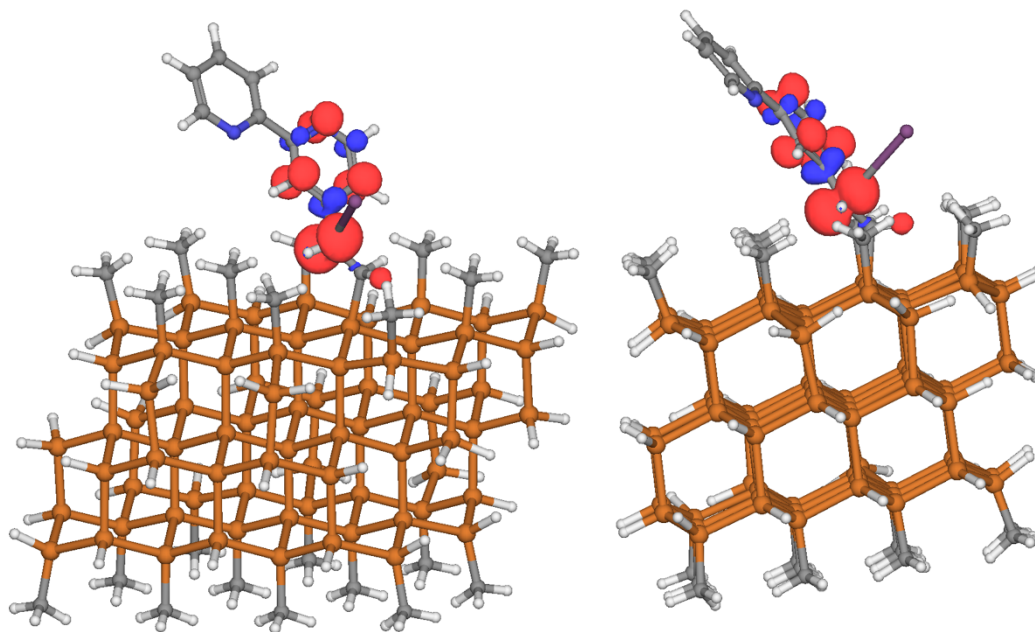
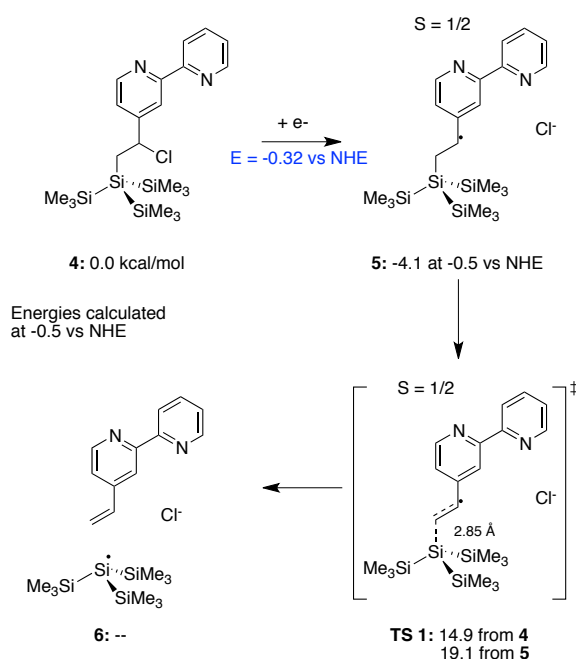


**Figure 6.4:** Spin density from two views on the reduced chlorinated complex **2** attached to a silicon cluster. The molecular and attached spin densities are quite similar to the molecular complex. The C-Cl distance is 3.62 Å, suggesting the chlorine has migrated from the linker.

The reduction of the chlorinated bpy system with loss of a chloride ion is calculated to occur at -0.32 V vs NHE, which can be verified experimentally. The overall barrier for the separation of the de-chlorinated bpy complex from the tris(trimethyl)silane is 14.9 kcal/mol, calculated with the free energy of an electron at -0.5 V vs NHE from the unreduced ground state, **4**. The barrier for dissociation from the immediately preceding step **5** is independent of the energy of the electron and the operating potential. This barrier is calculated to be 19.1 kcal/mol.



**Scheme 6.1:** The transition state for dissociation using a tristrimethylsilane toy system is shown in **TS 1**. While the overall barrier is dependent on the operating potential, the barrier energy from **5** is constant at 19.1 kcal/mol. This is accessible at room temperature. Additionally, the driving force for this complex gets stronger as more negative potentials are reached.

However, the overall barrier is dependent on the potential at which the reduction occurs. This dependence is shown in Figure 6.5. As the system is taken to more negative potentials, the loss of the bpy complex will occur even more quickly, such that once the system is at a potential of -1.1 V vs NHE, the barrier is nearly thermoneutral with the ground state. Additionally, bond strengths vary with the number of Si groups attached to the silane of interest<sup>48</sup>, so in the practically infinite Si crystal, this dissociation may occur even more rapidly than predicted by the molecular calculation. Effectively, the chlorine on the linker weakens the attachment to the surface.

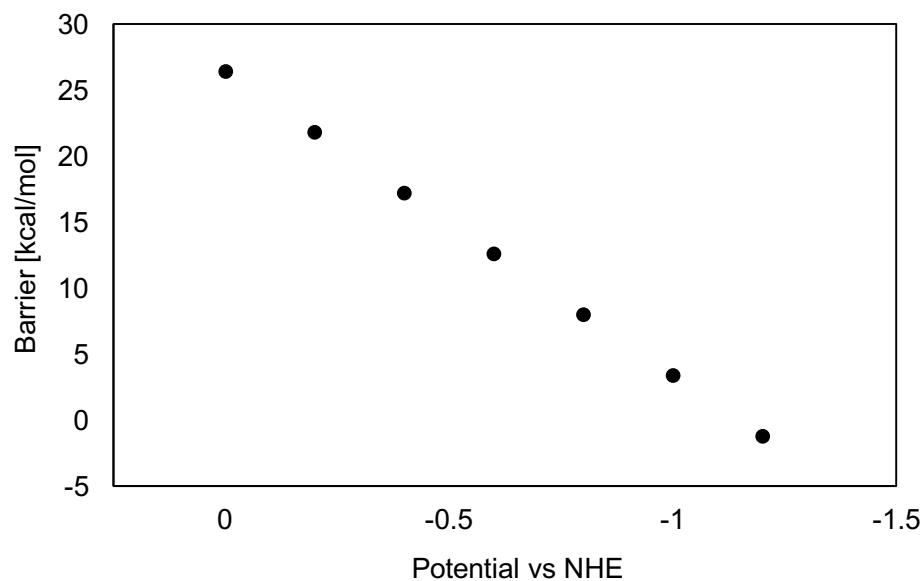


**Figure 6.5:** Overall dissociation barrier as a function of potential. As more negative potentials are reached, the dissociation becomes more kinetically favorable.

#### *Other bpy systems as replacements*

As analogous behavior can be seen between the molecular calculation and the cluster calculation, the molecular calculations can be used to screen complexes. One change that can be made is to use other halogens in the attachment process. Fluorine and bromine were attached to both the  $\alpha$ - and  $\beta$ -carbons of the linker and the molecular complex was reduced in solution, as shown in Figure 6.6, complexes **7** and **8**.

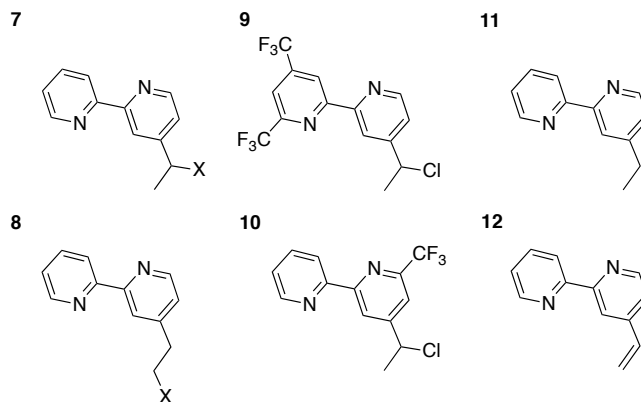


**Figure 6.6:** Molecular test analogues used to investigate ways to utilize bpy's non-innocent properties. In the halogenated species **7** and **8**, X = F, Br.

As bromine is typically classified as a better leaving group than chlorine, it is unsurprising that under reduction, the brominated ligand decayed in both positions. The fluorinated ligand, however, was stable under reduction in both positions, yielding an improvement upon the chlorinated ligand. Spin density plots for all modified complexes can be seen in Figure 6.7. The brominated case is quite similar to the chlorinated analogue, where the spin density extends into the linker. However, the fluorinated analogue shows much different behavior, with the bulk of the spin density isolated in the bpy, the expected non-innocent behavior. The fluorine does not appear to dissociate in the form of a fluoride ion.

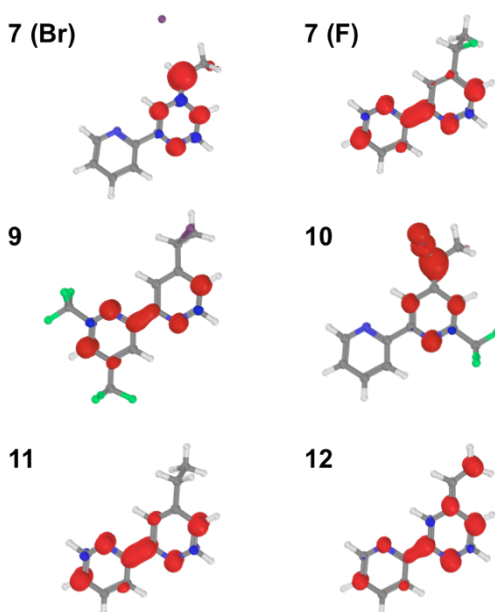


**Figure 6.7:** Spin density plots of the modified bpy ligands. In the fluorinated (**7F**), bis- $\text{CF}_3$  (**9**) and  $\text{sp}^3$ -hybridized linker (**11**) cases, electron density is isolated on the bpy, behavior expected for the non-innocent ligand

From this behavior, it can be predicted that the fluorinated complex would be stable on the surface and would not degrade. The geometry and spin density plot of this complex is seen in Figure 6.8. In the reduced molecular complex, the C-F bond in the linker is 1.42 Å, whereas in the bound complex, the C-F bond is 1.44 Å. This is slightly lengthened; however, it could be due to the smaller basis set by which the cluster-molecule complexes are calculated. Similar to the molecular complex, the spin density is largely isolated on the bpy ligand, with only a small amount on the fluorine. The spin density on the surface-attached fluorine is 0.00645, while the



molecular species has a spin density of 0.00036 on the fluorine. While there is a difference, this is still insignificant to the amount on the C and N atoms of the bipyridal group, which ranges from 0.15 to 0.25 on both the molecular and surface-attached complexes. The difference in fluorine spin densities on the fluorine may be attributed to the difference in basis set used. What is more significant is that there is very little spin density on the  $\beta$ -carbon of the linker (0.01504).

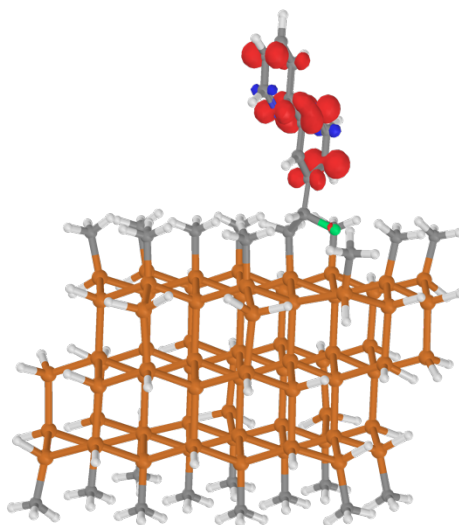


**Figure 6.8:** Spin density plot of the surface-attached fluorinated complex. Density is mostly confined to the bpy ligand.

It would appear that isolation of the added electron during reduction on the bpy ligand leaves the linker intact. Thus approaches to prevent the movement of electron density to the linker may be key to increasing the robustness of surface attached catalysts. One way of doing this is to add electron-withdrawing groups to the bpy to draw the electron off the linker. As hypothetical test cases, both 4'-(1-chloroethyl)-4,6-bis(trifluoromethyl)-2,2'-bipyridine (**9**) and 4-(1-chloroethyl)-6-(trifluoromethyl)-2,2'-bipyridine (**10**) were reduced and compared. Trifluoromethyl ( $\text{CF}_3$ ) groups are both strongly electron-withdrawing<sup>49</sup> and meta-directing, so they were strategically placed to maximize electron density on the bpy moiety. The spin density plots of **9** and **10** are shown in Figure 6.6. While **9** shows improvement upon the original complex **2**, there is some residual spin density on the  $\beta$ -carbon of the linker. The C-Cl bond in the reduced complex **9** is 1.89 Å, whereas the unreduced complex **2** has a C-Cl bond of 1.87 Å, which suggests that though there is some spin density on the linker, it does not significantly

encourage dissociation of the chloride ion. Using one  $\text{CF}_3$  group on the meta position to the vinyl linkage, as in complex **10**, does not appear to be an improvement upon the parent complex as the spin density again extends into the linker. The use of electron withdrawing groups on the bpy complex may prevent dissociation; however, their position is very important. To achieve this, asymmetric synthesis is necessary. Additionally, these groups may affect catalysis.

A potentially more successful approach would be to eliminate ionic groups on the linkers altogether, either through a  $\text{sp}^2$  or  $\text{sp}^3$  hybridized linker. These complexes, **11** and **12** respectively, and their spin densities can be seen in Figure 6.6. While both complexes do not degrade, it is important to note that the conjugation between the bpy and the vinyl linkage is quite clear, as spin density is delocalized over the entire complex. In the  $\text{sp}^3$  ethyl linkage, the electron is fully confined to the bpy complex and none remains on the linker. Berry's work with Co porphyrin catalysts utilized a long (greater than 9  $\text{CH}_2$  units), largely  $\text{sp}^3$  hybridized linkage that showed great stability.<sup>19</sup> However, the linker is long enough that the catalyst could potentially fold over towards the surface, allowing for diffusional electron transport. Berry et al. reports that there was a change in the cyclic voltammogram of the system that showed settling after the first 300 cycles, suggesting that an ideal conformation may be found after some cycling.<sup>19</sup> Electron hopping or tunneling through the linker would be unlikely with such a long linker. A short  $\text{sp}^3$  hybridized linker would be ideal.

An acetylide  $\text{sp}$  hybridized linker was also explored, based on recent studies involving ethynyl and propynyl functionalization of  $\text{Si}^{50}$  and the modification of the Si band structure with fluorinated phenyl groups bound to the surface with these groups.<sup>51</sup> In the past,  $\text{sp}$  hybridized groups have been used in dye-sensitized solar cells (DSSCs) in rigid rod constructions to make linkers that would not bend<sup>52,53</sup>, and have been used in conjunction with bipyridine groups.<sup>54</sup> In order to investigate the possibility of using these groups as linkers, 4-ethynyl-2,2'-bipyridine moieties were reduced both molecularly and on the cluster, as is seen in Figure 6.9.

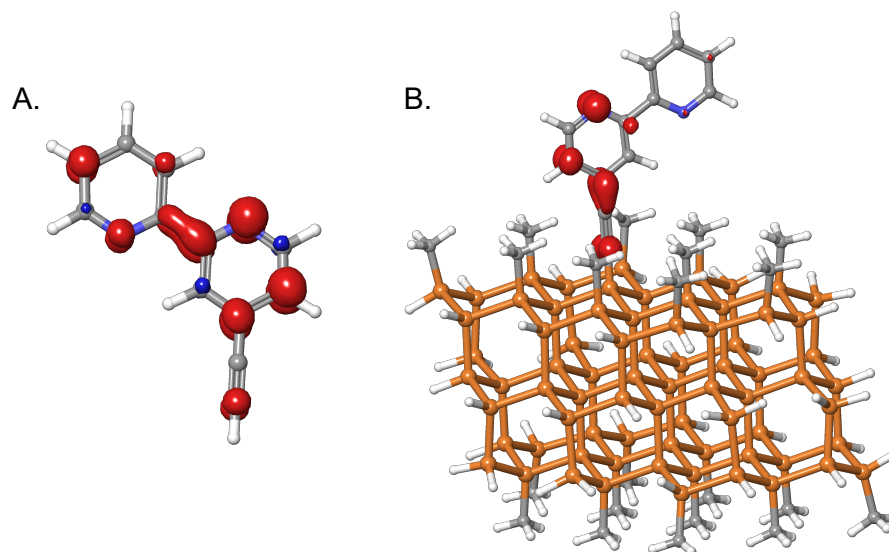


**Figure 6.9:** Spin density on reduced 4-ethynyl-2,2'-bipyridine A) in molecular form and B) on the cluster surface.

In Figure 6.9A, the spin density plot shows some spin density on the  $\alpha$ -carbon, though none on the  $\beta$ -carbon. Once bound to the cluster (Figure 6.9B), we see that some electron density extends onto the  $\beta$ -carbon, but most of it is in the first pyridine ring and on the  $\alpha$ -carbon, a departure from what has been previously seen. This is corroborated by the change in bond length upon reduction. In **2** bound to the cluster (see Figure 6.4), the C-C bond length in the linker changes from 1.54 Å to 1.48 Å, shortening due to the loss of the Cl. In contrast, in the  $sp$  hybridized system, the linker actually extends slightly, from 1.23 Å to 1.24 Å, much less change, however, than the chlorinated system. The triple bond here in this case may be helpful. By hosting some electron density, it may not be as stable as a fully  $sp^3$ -hybridized case, but it appears to be more robust than the chlorinated linkers.

The rate of electron transfer through such a linker is critical. Using DSSCs as an analogue, Li et al. calculated that fully  $sp^3$  hybridized linkers slowed electron injection from a dye into a  $TiO_2$  cluster by a factor of  $\sim 7$  relative to alkene linkers.<sup>55</sup> These times for electron injection are in the tens of femtoseconds range. However, even in seemingly fast or selective catalysts, the turnover frequencies are usually in  $0.1\text{-}10\text{ s}^{-1}$ .<sup>5,16,56</sup> Often the rate-limiting step is not one that is electrochemical, but rather binding of the substrate, protonation, or hydride transfer. This means

that even with the slowed rate of electron transfer, the linker will not likely be the limit for the catalyst and all strategies should be pursued.

### **Conclusion**

In this chapter, we have identified the thermodynamically preferred surface attachment structure in the attachment of vinyl bpy to a partially chlorinated Si(111) surface. This involves chlorination on the  $\beta$ -carbon of the linker, which inevitably leads to the electrochemical decomposition seen experimentally. In order to achieve this level of understanding, calculations were performed on Si clusters, as well as trimethyltrissilyl silane molecules. Future work involves expanding this analysis to periodic systems, though this is often difficult due to limitations in unit cell size and solvation. Several alternative systems for linking have been proposed, including replacing chlorine with fluorine, and using  $sp^3$  and  $sp$  hybridized linkers. These options provide a blueprint for experimentally creating more robust surface attachments for electrochemical catalysts on Si.

## References

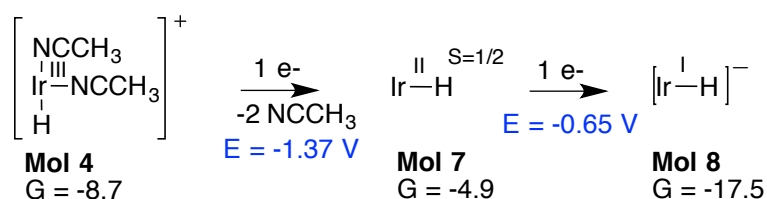
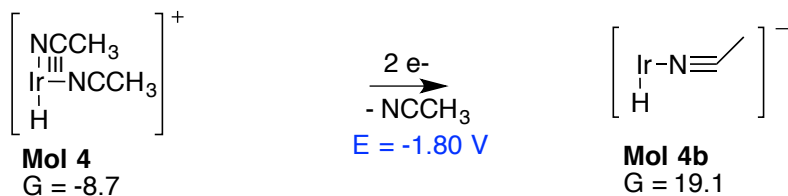
- (1) Lewis, N. S.; Nocera, D. G. *Proc. Natl. Acad. Sci. USA* **2006**, *103*, 15729-15735.
- (2) Olah, G. A. *Angew. Chem. Int. Ed.* **2013**, *52*, 104-107.
- (3) Li, C. W.; Kanan, M. W. *J. Am. Chem. Soc.* **2012**, *134*, 7231-7234.
- (4) Kuhl, K. P.; Cave, E. R.; Abram, D. N.; Jaramillo, T. F. *Energy Environ. Sci.* **2012**, *5*, 7050-7059.
- (5) Kang, P.; Cheng, C.; Chen, Z.; Schauer, C. K.; Meyer, T. J.; Brookhart, M. J. *Am. Chem. Soc.* **2012**, *134*, 5500-5503.
- (6) Benson, E. E.; Kubiak, C. P.; Sathrum, A. J.; Smieja, J. M. *Chem. Soc. Rev.* **2009**, *38*, 89-99.
- (7) Costentin, C.; Robert, M.; Saveant, J.-M. *Chem. Soc. Rev.* **2013**, *42*, 2423-2436.
- (8) Jessop, P. G.; Joó, F.; Tai, C.-C. *Coord. Chem. Rev.* **2004**, *248*, 2425-2442.
- (9) Abruña, H. D. *Coord. Chem. Rev.* **1988**, *86*, 135-189.
- (10) Murray, R. W. *Acc. Chem. Rev.* **1980**, *13*, 135-141.
- (11) McCreery, R. L. *Chem. Rev.* **2008**, *108*, 2646-2687.
- (12) Wrighton, M. S. *Science* **1986**, *231*, 32-37.
- (13) Inglis, J. L.; MacLean, B. J.; Pryce, M. T.; Vos, J. G. *Coord. Chem. Rev.* **2012**, *256*, 2571-2600.
- (14) Chardon-Noblat, S.; Deronzier, A.; Ziessel, R.; Zsoldos, D. *J. Electroanal. Chem.* **1998**, *444*, 253-260.
- (15) Bolinger, C. M.; Story, N.; Sullivan, B. P.; Meyer, T. J. *Inorg. Chem.* **1988**, *27*, 4582-4587.
- (16) Blakemore, J. D.; Gupta, A.; Warren, J. J.; Brunschwig, B. S.; Gray, H. B. *J. Am. Chem. Soc.* **2013**, *135*, 18288-18291.
- (17) Kang, P.; Zhang, S.; Meyer, T. J.; Brookhart, M. *Angew. Chem.* **2014**, *126*, 8853-8857.
- (18) Sun, C.; Gobetto, R.; Nervi, C. *New J. Chem.* **2016**, *40*, 5656-5661.
- (19) Yao, S. A.; Ruther, R. E.; Zhang, L.; Franking, R. A.; Hamers, R. J.; Berry, J. F. *J. Am. Chem. Soc.* **2012**, *134*, 15632-15635.
- (20) Lattimer, J. R. C.; Blakemore, J. D.; Sattler, W.; Gul, S.; Chatterjee, R.; Yachandra, V. K.; Yano, J.; Brunschwig, B. S.; Lewis, N. S.; Gray, H. B. *J. Chem. Soc., Dalton Trans.* **2014**.
- (21) Elgrishi, N.; Griveau, S.; Chambers, M. B.; Bedioui, F.; Fontecave, M. *Chem. Comm.* **2015**, *51*, 2995-2998.
- (22) Oh, S.; Gallagher, J. R.; Miller, J. T.; Surendranath, Y. *J. Am. Chem. Soc.* **2016**, *138*, 1820-1823.
- (23) Lattimer, J. R. C.; Brunschwig, B. S.; Lewis, N. S.; Gray, H. B. *J. Phys. Chem. C* **2013**, *117*, 27012-27022.
- (24) Quintana, L. M. A.; Johnson, S. I.; Corona, S. L.; Villatoro, W.; Goddard, W. A.; Takase, M. K.; VanderVelde, D. G.; Winkler, J. R.; Gray, H. B.; Blakemore, J. D. *Proc. Natl. Acad. Sci. USA* **2016**, *113*, 6409-6414.
- (25) Bolinger, C. M.; Story, N.; Sullivan, B. P.; Meyer, T. J. *Inorg. Chem.* **1988**, *27*, 4582-4587.
- (26) Brennaman, M. K.; Dillon, R. J.; Alibabaei, L.; Gish, M. K.; Dares, C. J.; Ashford, D. L.; House, R. L.; Meyer, G. J.; Papanikolas, J. M.; Meyer, T. J. *J. Am. Chem. Soc.* **2016**, *138*, 13085-13102.
- (27) Blakemore, J. D.; Schley, N. D.; Balcells, D.; Hull, J. F.; Olack, G. W.; Incarvito, C. D.; Eisenstein, O.; Brudvig, G. W.; Crabtree, R. H. *J. Am. Chem. Soc.* **2010**, *132*, 16017-16029.
- (28) Durrell, A. C.; Li, G.; Koepf, M.; Young, K. J.; Negre, C. F. A.; Allen, L. J.; McNamara, W. R.; Song, H.-e.; Batista, V. S.; Crabtree, R. H.; Brudvig, G. W. *J. Catal.* **2014**, *310*, 37-44.
- (29) Clark, M. L.; Rudshteyn, B.; Ge, A.; Chabolla, S. A.; Machan, C. W.; Psciuk, B. T.; Song, J.; Canzi, G.; Lian, T.; Batista, V. S.; Kubiak, C. P. *J. Phys. Chem. C.* **2016**.
- (30) Becke, A. D. *J. Chem. Phys.* **1993**, *98*, 5648-5652.
- (31) Lee, C. T.; Yang, W. T.; Parr, R. G. *Phys. Rev. B* **1988**, *37*, 785-789.
- (32) Hay, P. J.; Wadt, W. R. *J. Chem. Phys.* **1985**, *82*, 299-310.
- (33) Francl, M. M.; Pietro, W. J.; Hehre, W. J.; Binkley, J. S.; Gordon, M. S.; Defrees, D. J.; Pople, J. A. *J. Chem. Phys.* **1982**, *77*, 3654-3665.
- (34) Hehre, W. J.; Ditchfie.R; Pople, J. A. *J. Chem. Phys.* **1972**, *56*, 2257-2261.
- (35) Dovesi, R. O., R.; Civalleri, B.; Roetti, C.; Saunders, V. R.; Zicovich-Wilson, C. M. *Z. Kristallogr.* **2005**, *220*, 571-573.
- (36) Galynska, M.; Persson, P. In *Advances in Quantum Chemistry*; Sabin, J. R., Ed. 2014; Vol. 69, p 303-332.
- (37) Galynska, M.; Persson, P. *Int. J. Quantum Chem.* **2013**, *113*, 2611-2620.
- (38) Bochevarov, A. D.; Harder, E.; Hughes, T. F.; Greenwood, J. R.; Braden, D. A.; Philipp, D. M.; Rinaldo, D.; Halls, M. D.; Zhang, J.; Friesner, R. A. *Int. J. Quantum Chem.* **2013**, *113*, 2110-2142.
- (39) Johnson, S. I.; Nielsen, R. J.; Goddard, W. A. *ACS Catal.* **2016**, 6362-6371.

- (40) Zhou, M.; Johnson, S. I.; Gao, Y.; Emge, T. J.; Nielsen, R. J.; Goddard, W. A.; Goldman, A. S. *Organometallics* **2015**, *34*, 2879-2888.
- (41) Zhao, Y.; Truhlar, D. G. *Theor. Chem. Acc.* **2008**, *120*, 215-241.
- (42) Krishnan, R.; Binkley, J. S.; Seeger, R.; Pople, J. A. *J. Chem. Phys.* **1980**, *72*, 650-654.
- (43) Clark, T.; Chandrasekhar, J.; Spitznagel, G. W.; Schleyer, P. V. J. *Comp. Chem.* **1983**, *4*, 294-301.
- (44) Cicero, R. L.; Linford, M. R.; Chidsey, C. E. D. *Langmuir* **2000**, *16*, 5688-5695.
- (45) Buriak, J. M. *Chem. Mater.* **2014**, *26*, 763-772.
- (46) Saji, T.; Aoyagui, S. *J. Electroanal. Chem. Interfacial Electrochem.* **1975**, *58*, 401-410.
- (47) Chatgililoglu, C. *Chem. Rev.* **1995**, *95*, 1229-1251.
- (48) Wu, Y.-D.; Wong, C.-L. *J. Org. Chem.* **1995**, *60*, 821-828.
- (49) Hansch, C.; Leo, A.; Taft, R. W. *Chem. Rev.* **1991**, *91*, 165-195.
- (50) Plymale, N. T.; Kim, Y.-G.; Soriaga, M. P.; Brunschwig, B. S.; Lewis, N. S. *J. Phys. Chem. C* **2015**, *119*, 19847-19862.
- (51) Plymale, N. T.; Ramachandran, A. A.; Lim, A.; Brunschwig, B. S.; Lewis, N. S. *J. Phys. Chem. C* **2016**, *120*, 14157-14169.
- (52) Chitre, K.; Batarseh, A.; Kopecky, A.; Fan, H.; Tang, H.; Lalancette, R.; Bartynski, R. A.; Galoppini, E. *J. Phys. Chem. B* **2015**, *119*, 7522-7530.
- (53) Galoppini, E. *Coord. Chem. Rev.* **2004**, *248*, 1283-1297.
- (54) Wang, D.; Mendelsohn, R.; Galoppini, E.; Hoertz, P. G.; Carlisle, R. A.; Meyer, G. J. *J. Phys. Chem. B* **2004**, *108*, 16642-16653.
- (55) Li, J.; Wang, H.; Persson, P.; Thoss, M. *J. Chem. Phys.* **2012**, *137*.
- (56) Cosnier, S.; Deronzier, A.; Vlachopoulos, N. *J. Chem. Soc., Chem. Commun.* **1989**, 1259-1261.

## Appendix A

APPENDIX A: SUPPLEMENTARY CALCULATIONS SUPPORTING CO<sub>2</sub> REDUCTION**Appendix A.1: Calculation of the doubly reduced acetonitrile complex**

In work by Cao et al., (Cao, L.; Sun, C.; Sun, N.; Meng, L.; Chen, D. *Dalton Trans.* **2013**, 42, 5755.) a doubly reduced cationic solvento complex was calculated, as shown below. However, the geometry showed a bent acetonitrile, suggesting that the acetonitrile had been reduced, not the metal center. When this complex is recalculated with our methods, we see a reduction potential of -1.8 vs SHE, which is too negative for the experimentally observed reduction potential.

**Currently Proposed Reduction****Previously Proposed Reduction**

**Scheme A.1:** Free energies calculated in acetonitrile at -1.2V vs SHE. Reduction with loss of solvent is preferred to a two-electron reduction of the solvento complex, as previously proposed,<sup>1</sup> which leads to a reduced acetonitrile adduct. Energies in kcal/mol.

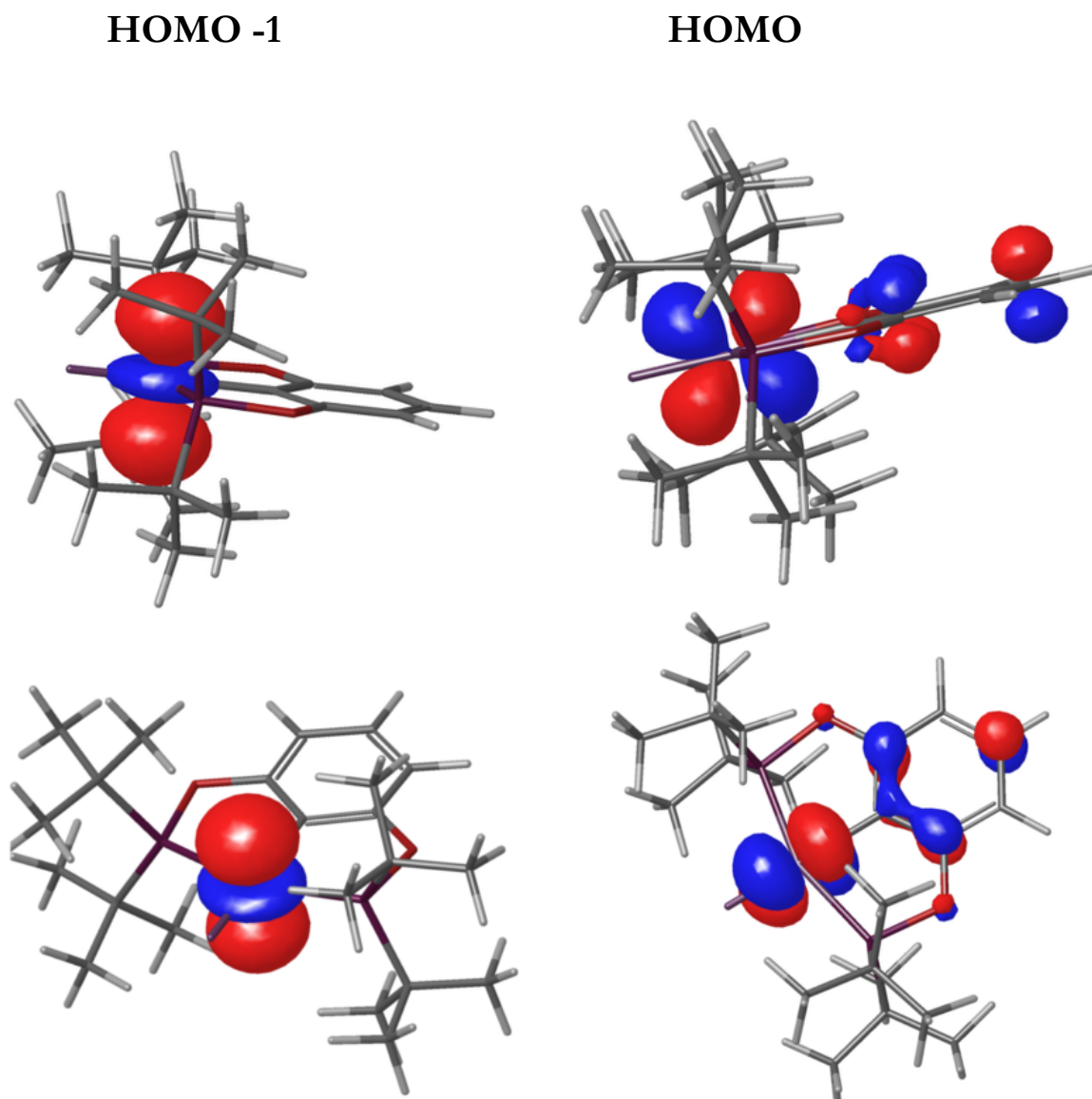


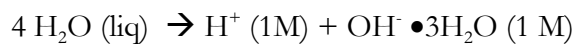
Figure S1: HOMO of Ir<sup>I</sup> complex

The HOMO -1 and HOMO of POCOP-Ir<sup>I</sup> hydride anion (**Mol 8**) is shown. The high electron density in axial positions explains why oxygen cannot coordinate simultaneously in a transition state analogous to **TS 2**.



### Appendix A.3: Justification for Calculations with Water Clusters

The calculated free energy and pKa for the auto-dissociation of water is used to justify our use of an explicit four-water cluster (plus continuum solvation) in transition state calculations. A neutral  $4\text{H}_2\text{O}$  and anionic  $\text{OH}^- \bullet 3\text{H}_2\text{O}$  cluster were used.



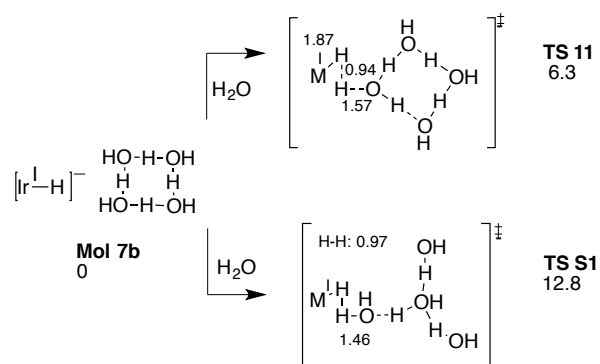
$$\Delta G_{\text{calc}} = 20.2 \text{ kcal/mol}$$

$$\Delta G_{\text{exp}} = 19.05 \text{ kcal/mol}$$



is the free energy of reaction with CO<sub>2</sub> to form formate, involving a change in overall charge. These can be seen in Scheme 2b. The difference in free energies of these reactions does not exceed 0.5 kcal/mol, which is well within the error of DFT. Thus, we feel comfortable in using the simplified ligand scaffold.

## Appendix A.5



**Scheme A.5:** Free energies for protonation via the Y-shaped cluster

Protonation via the Y-shaped cluster used previously for protonation has a higher barrier than the square shaped cluster, showing that water orientation is significant.

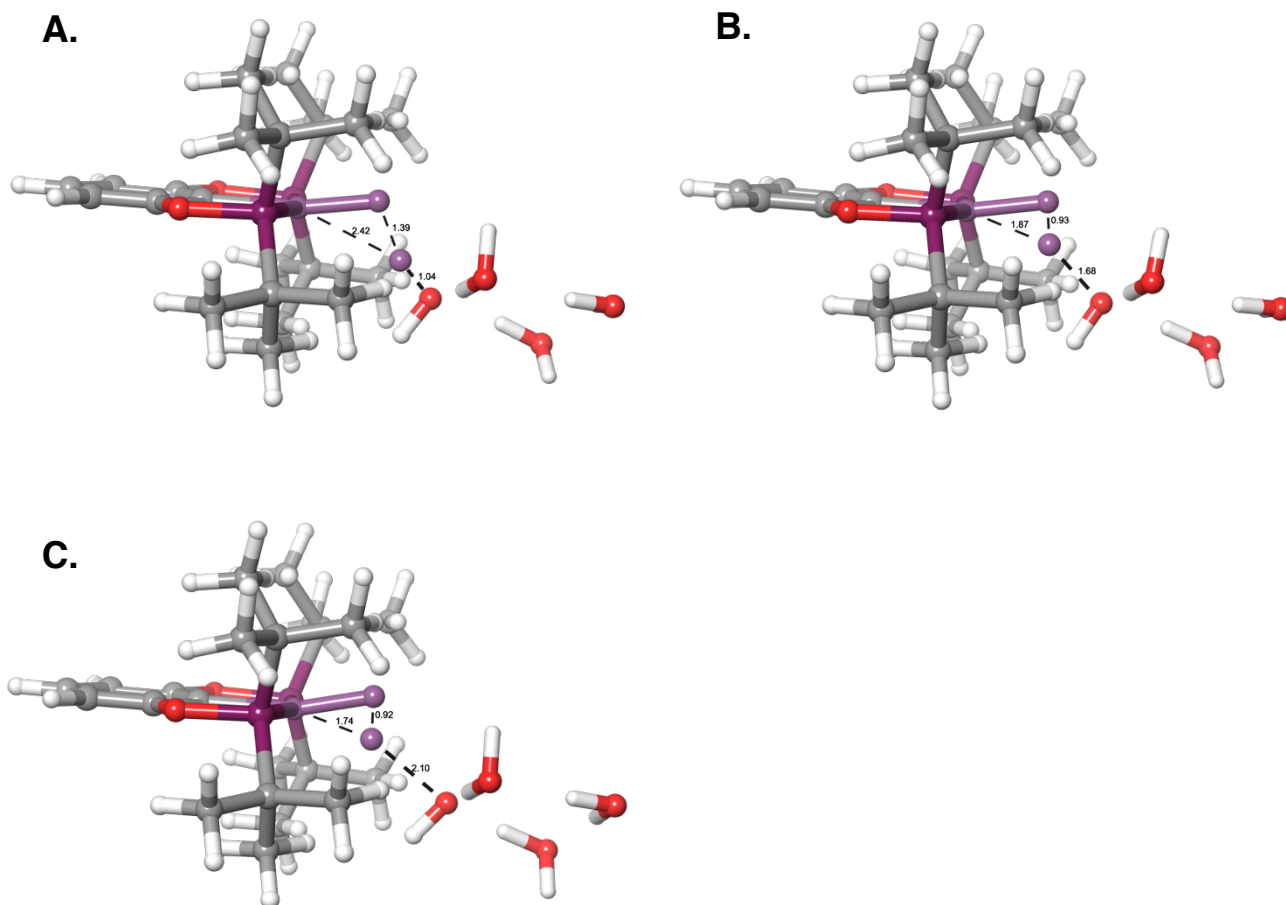


**Figure A.6:** Figures of points along the intrinsic reaction coordinate calculation. A. Point on the reverse path; B. The transition state; C. Point on the forward path. All bond lengths in Angstroms. For reference, the spectator Ir-H bond length is 1.70 Å.

## Appendix A.7

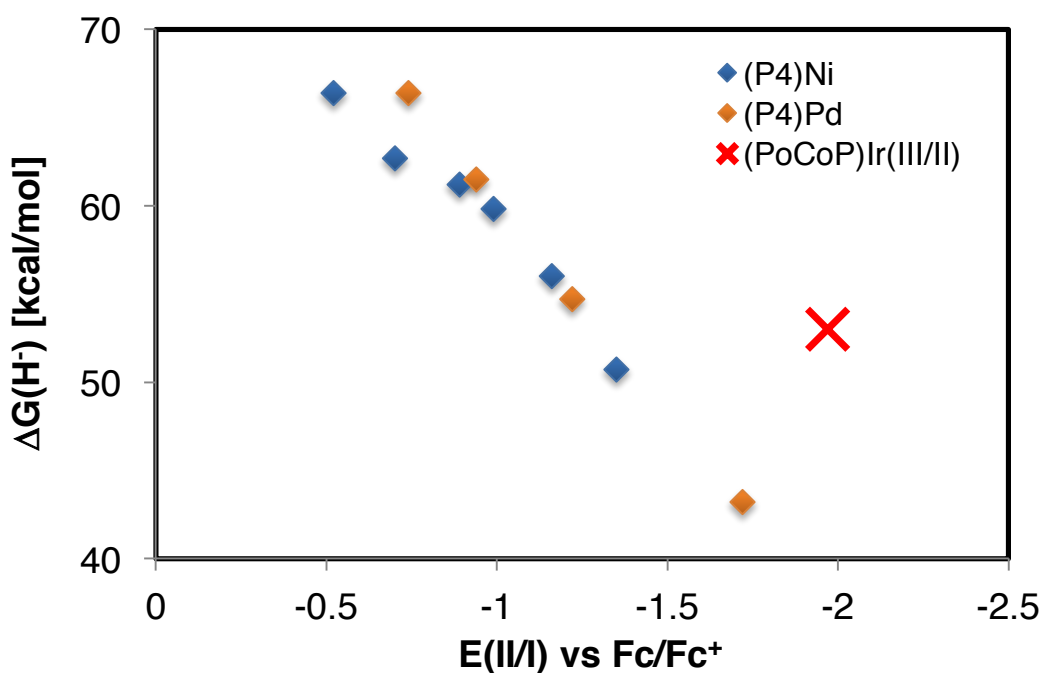


Figure A.7: Hydricities of (POCOP) Ir compared to other hydridic compounds

In Figure S3, the first reduction potential vs ferrocene of several  $\text{P}_4 \text{Ni}^2$  and  $\text{Pd}^3$  compounds are plotted against their measured hydricities in acetonitrile, denoted by the blue and yellow diamonds. Dubois and coworkers noted that the first half-wave one electron reduction potential correlated linearly with the resulting measured hydricity. The point marked by the red “X” is that calculated for  $(\text{POCOP})\text{Ir}(\text{H})_2(\text{NCCH}_3)$  for the (III/II) couple vs ferrocene. The value for this does not lie on the line established by the Pd and Ni compounds, which means that while the Ir complex has a calculated hydricity near some of the more reactive Pd and Ni compounds, more energy is required to gain the same return in hydricity. This indicates an interesting relationship between hydricity and structure.

## References

1. Cao, L.; Sun, C.; Sun, N.; Meng, L.; Chen, D. *Dalton Trans.* **2013**, *42*, 5755.
2. Berning, D. E.; Miedaner, A.; Curtis, C. J.; Noll, B. C.; Rakowski DuBois, M. C.; DuBois, D. L., Free-Energy Relationships between the Proton and Hydride Donor

Abilities of [HNi(diphosphine)<sub>2</sub>]<sup>+</sup> Complexes and the Half-Wave Potentials of Their Conjugate Bases. *Organometallics* **2001**, *20* (9), 1832-1839.

3. Raebiger, J. W.; Miedaner, A.; Curtis, C. J.; Miller, S. M.; Anderson, O. P.; DuBois, D. L., Using Ligand Bite Angles To Control the Hydricity of Palladium Diphosphine Complexes. *J. Am. Chem. Soc.* **2004**, *126* (17), 5502-5514.

## Appendix B

APPENDIX B: FULL RESULTS ON MODIFICATION OF POCOP  
PINCERS

## Appendix B.1: Results of simulations involving substitutions of (R-POCOP)Ir

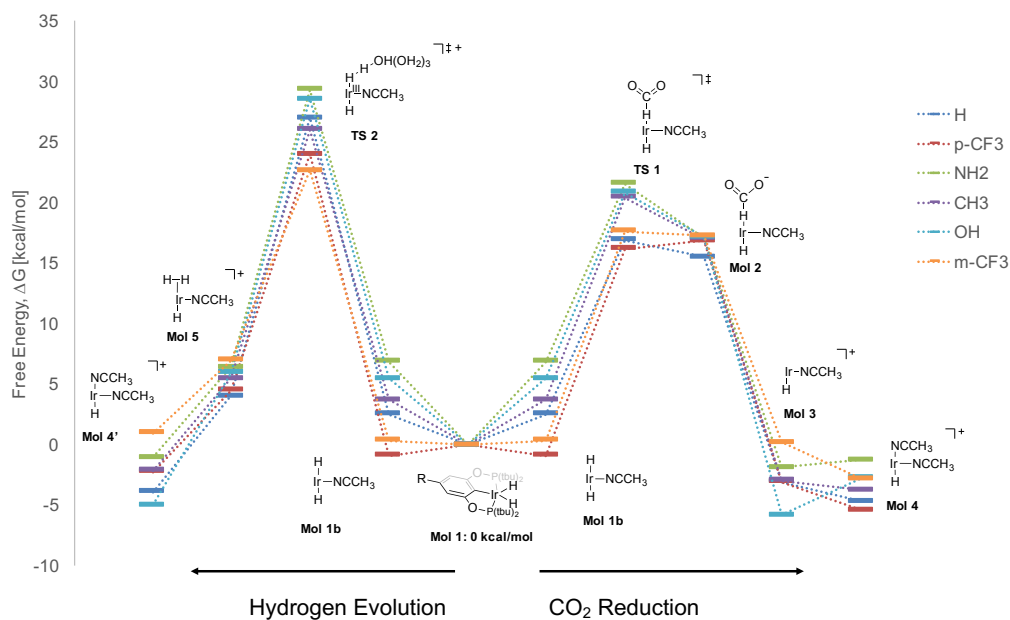


**Figure B.1:** Full results of modifications of the *para* position of pincers. Trends here largely scale with electron withdrawing ability of the catalysts. Numerical results can be seen in the table below.

**Table B.1:** All free energies ( $\Delta G$ ) of para substitutions on barriers and kinetics of CO<sub>2</sub>RR and HER

Energies in kcal/mol		Functional group (R)					
		H	<i>p</i> -CF <sub>3</sub>	NH <sub>2</sub>	CH <sub>3</sub>	OH	<i>m</i> -CF <sub>3</sub>
Intermediate Name	Mol 4'	-3.9	-4.6	-0.5	-3.0	-2.0	-2.0
	Mol 9	4.0	4.5	6.4	5.5	5.9	7.0
	TS 2	27.0	24.0	29.3	26.0	28.5	22.6
	Mol 1b	2.5	-0.9	6.8	3.7	5.5	0.4
	Mol 1	0.0	0.0	0.0	0.0	0.0	0.0
	Mol 1b	2.5	-0.9	6.8	3.7	5.5	0.4
	TS 1	16.9	16.2	21.5	20.4	20.8	17.6
	Mol 2	15.5	16.8	17.1	17.0	17.1	17.2
	Mol 3	-3.1	-3.1	-1.9	-3.0	-5.8	0.2
	Mol 4	-4.7	-5.4	-1.3	-3.8	-2.8	-2.8



*Appendix C*

## APPENDIX C: MOLECULAR COORDINATES

The molecular coordinates for many of the complexes found in this thesis can be found online as supplementary material. These coordinates are in .xyz format and are titled in the coordinates as they are in the figures of this document. They can be viewed using several free programs available online including Mercury ([www.ccdc.cam.ac.uk/mercury](http://www.ccdc.cam.ac.uk/mercury)) and MacmolPLT ([brettbode.github.io/wxmacmolplt](https://brettbode.github.io/wxmacmolplt)).

